Small-signal stability analysis of voltage source converter based high-voltage

Grdenić, Goran

University of Zagreb
FACULTY OF ELECTRICAL ENGINEERING AND COMPUTING

Goran Grdenić

SMALL-SIGNAL STABILITY ANALYSIS OF VOLTAGE SOURCE CONVERTER BASED HIGH-VOLTAGE DIRECT-CURRENT SYSTEMS

DOCTORAL THESIS

Zagreb, 2019

University of Zagreb
FACULTY OF ELECTRICAL ENGINEERING AND COMPUTING

Goran Grdenić

SMALL-SIGNAL STABILITY ANALYSIS OF VOLTAGE SOURCE CONVERTER BASED HIGH-VOLTAGE DIRECT-CURRENT SYSTEMS

DOCTORAL THESIS

Supervisor: Professor Marko Delimar, PhD

Zagreb, 2019

Sveučilište u Zagrebu
FAKULTET ELEKTROTEHNIKE I RAČUNARSTVA

GORAN GRDENIĆ

ANALIZA STABILNOSTI SLABOGA SIGNALA VISOKONAPONSKIH ISTOSMJERNIH SUSTAVA S PRETVARAČIMA S NAPONSKIM ULAZOM

DOKTORSKI RAD

Mentor: prof. dr. sc. Marko Delimar

Zagreb, 2019.

Doctoral thesis is created at the University of Zagreb Faculty of Electrical Engineering and Computing, Department of Energy and Power Systems

Supervisor: Professor Marko Delimar, PhD

Doctoral thesis has: 137 pages

Doctoral thesis No.:_____

About the supervisor

Marko Delimar was born in Zagreb in 1974. He received B.Sc., M.Sc. and Ph.D. degrees in electrical engineering from the University of Zagreb, Faculty of Electrical Engineering and Computing (FER), Zagreb, Croatia, in 1996, 2001 and 2005, respectively. He received a “Diploma Study in Management” (International postgraduate study in business management) degree from FER in 1997.

From 1997 he is working at the Department of Energy and Power Systems at FER, currently as a full professor. From 2013 to 2017 he was a member of the Steering Committee of the Smartgrids ETP (European Technology platform for the Electricity Networks of the Future). From 2014 to 2018 he served as Vice Dean for Education at FER. From 2015 he serves as Chairman of the Council and Head of the University of Zagreb dislocated university undergraduate Study of Energy Efficiency and Renewable Energy Sources in Šibenik. He is a member of the National Development Strategy 2030 Thematic Working Group on Energy and Sustainable Environment. He participated in nine national (Croatia Science Foundation, Ministry of Science and Education) and three international (FP7, bilateral) research projects. He published over 80 scientific articles in journals and conference proceedings.

Prof. Delimar is a member of IEEE, HRO Cigré and MIPRO. He is a member of steering, program, scientific and/or organizing committees of several prominent international conferences and symposia and a specialist editor for power and energy in an international journal. The Society of University Teachers, Scholars and Other Scientists – Zagreb awarded him the Young Scientist's Annual Award in 1998. He received silver medal “Josip Lončar” from FER for an outstanding Ph.D. thesis in 2006. The IEEE Regional Activities Board awarded him the annual Achievement Award in 2006. The IEEE Croatia Section awarded him the Distinguished Service Award in 2007. The IEEE Member and Geographic Activities Board awarded him the 2009 Innovation Award for the creation of the IEEEXtreme Programming Contest. In 2011 and 2012 he served as the Director of IEEE Region 8 (Europe, Africa and the Middle East); in 2013 and 2014 as IEEE Secretary; and from 2011 to 2014 as a member of the IEEE Board of Directors. Currently he is serving as a member of the Board of Directors of the IEEE Foundation and as Chair of IEEE European Public Policy Committee.

O mentoru

Marko Delimar rođen je u Zagrebu 1974. godine. Diplomirao je, magistrirao i doktorirao u polju elektrotehnike na Sveučilištu u Zagrebu Fakultetu elektrotehnike i računarstva (FER), 1996., 2001. odnosno 2005. godine. Međunarodni poslijediplomski studij poslovnog upravljanja „Diploma Study in Management“ završio je 1997. godine.

Od 1997. godine zaposlen je na Zavodu za visoki napon i energetiku FER-a, trenutačno kao redoviti profesor. Od 2013. godine do 2017. bio je član Koordinacijskog odbora Smartgrids ETP, odnosno Europske tehnološke platforme za napredne elektroenergetske mreže (European Technology Platform for the Electricity Networks of the Future). Od 2014. do 2018. godine bio je prodekan za nastavu FER-a. Od 2015. godine predsjednik je Vijeća i voditelj studija dislociranog sveučilišnog preddiplomskog Studija energetske učinkovitosti i obnovljivih izvora u Šibeniku Sveučilišta u Zagrebu. Trenutačno je član Tematske radne skupine za energiju i održivi okoliš za izradu Nacionalne razvojne strategije do 2030. godine. Sudjelovao je na devet nacionalnih (HRZZ, MZO) i tri međunarodna (FP7, bilateralni) znanstvena projekta. Objavio je više od 80 radova u časopisima i zbornicima radova konferencija.

Prof. Delimar aktivan je član IEEE, HRO Cigré i udruge MIPRO. Član je upravljačkih, programskih i/ili znanstvenih te organizacijskih odbora više uglednih međunarodnih skupova i konferencija, te urednik za područje elektroenergetike u međunarodnom časopisu. Društvo sveučilišnih nastavnika i drugih znanstvenika u Zagrebu dodijelilo mu je 1998. godine godišnju Nagradu Društva mladim znanstvenicima. Godine 2006. primio je srebrnu plaketu „Josip Lončar“ FER-a za posebno istaknutu doktorsku disertaciju. IEEE Regional Activities Board dodijelio mi je godišnju nagradu za postignuća u vođenju i organizaciji studentskih aktivnosti (Achievement Award) 2006. godine. Hrvatska Sekcija IEEE dodijelila mu je 2007. godine Nagradu za izuzetan doprinos Sekciji. IEEE Member and Geographic Activities Board dodijelio mu je 2009. godine godišnju nagradu za inovaciju (Innovation Award) za pokretanje međunarodnog natjecanja IEEEXtreme. U IEEE je 2011. i 2012. godine bio na dužnosti Direktora Regije 8 (Europa, Afrika i Bliski istok), 2013. i 2014. na dužnosti glavnog tajnika organizacije (IEEE Secretary), a od 2011. do 2014. godine bio je i član IEEE Upravnog odbora (IEEE Board of Directors). Trenutačno je direktor (član Upravnog odbora) IEEE Fondacije i predsjednik IEEE Odbora za javne politike u Europi.

Acknowledgement

First of all, I would like to thank my supervisor, professor Marko Delimar for the continuous mentorship during my PhD study, for providing me with the opportunity to be a teaching and research assistant at the Department of energy and power systems, for introducing me with an interesting topic of HVDC transmission, and for introducing me with the professors at the KU Leuven.

Many thanks to professor Jef Beerten for the warm hospitality at the KU Leuven and Energyville, for the selfless knowledge sharing, and the detailed review and useful advice on the thesis.

Finally, I would like to thank my family for all the support during these years in pursuing a PhD degree and sports results at the same time.

Summary

The main initiators of the higher employment of the voltage source converter based (VSC) high-voltage direct-current transmission (HVDC) are the connection of offshore wind power plants and the increasing necessity for flexibility and controllability in AC power grids. Transistor-based VSC technology has also facilitated the simpler implementation of truly meshed multi-terminal direct-current (MTDC) grids. Consequently, in AC grids, more converters are being located mutually in electrical proximity, forming multi-infeed HVDC (MI-HVDC) systems. Small-signal stability analysis (SSSA) is one of the most important methods for studying the inherent characteristics of dynamic systems and is a valuable tool of their design. This analysis is employed in the thesis to investigate the influence of different control and structural parameters in the aforementioned systems.

In VSC-based HVDC grids, the properties of grid interaction eigenvalues with respect to the operating point and grid structure are assessed. The obtained findings have helped in the selection of a voltage controlling converter with the highest stability margin of the dominant interaction mode and for the derivation of a method to tune the coefficients for voltage droop control. In VSC-based multi-infeed systems, different voltage and reactive power regulation methods are evaluated and compared. The impact of the short-circuit ratio (SCR) at the converter's connection point, active power flow and AC line length between converters are observed. Finally, the boundary selection, between dynamically and statically modeled parts in the AC grid hybrid model, is assessed to determine the most relevant converter and AC grid parameters. The study, including the comparison procedure based on SSSA, shows the importance of the speed of the phase-locked loop, the SCR at connection point and the length of adjacent AC lines.

Key words: high-voltage direct-current transmission, voltage source converters, multi-infeed HVDC systems, small-signal stability analysis

Analiza stabilnosti slaboga signala visokonaponskih istosmjernih sustava s pretvaračima s naponskim ulazom

Izumi višefaznoga indukcijskog motora te energetskoga transformatora krajem 19. stoljeća osigurali su prevlast izmjenične struje u elektroenergetskim sustavima. Međutim, prednosti prijenosa električne energije istosmjernom strujom nisu zaboravljene. Razvoj energetskih pretvarača u 20. stoljeću nastojao je nadograditi i ojačati postojeće izmjenične elektroenergetske sustave. Rezultati tehno-ekonomske usporedbe visokonaponskog istosmjernog i izmjeničnog prijenosa električne energije pokazuju kako istosmjerni nadzemni vodovi postaju opravdano rješenje za duljine vodova između 400 i 600 km, dok su kod kabelskih vodova te udaljenosti manje od 50 km. Naime, dugački nadzemni izmjenični vodovi zahtijevaju kompenzaciju jalove snage, te je stabilnost prijenosa ograničena duljinom voda. Veliki kapacitet kabelskih izmjeničnih vodova uzrokuje velike jalove struje, a kompenzacija jalove snage znatno je složenija u slučaju podmorskih kabela.

Dvije su osnovne vrste energetskih pretvarača danas u upotrebi u prijenosu električne energije istosmjernom strujom pri visokom naponu: mrežom komutirani (mrežno vođeni) pretvarači temeljeni na tiristorskoj tehnologiji, te pretvarači s naponskim ulazom (autonomni pretvarači) temeljeni na tranzistorskoj tehnologiji. Mrežom komutirani pretvarači u upotrebi su nekoliko desetljeća te se danas prije svega koriste za prijenos velikih količina električne energije na velike udaljenosti (u geografski velikim zemljama), te za povezivanje asinkronih izmjeničnih sustava. Razvoj visokonaponskih pretvarača temeljenih na tranzistorskoj tehnologiji krajem 20. stoljeća unaprijedio je mogućnosti istosmjernog prijenosa. Naime, tranzistorska tehnologija omogućila je neovisnu regulaciju djelatne i jalove snage, povezivanje sa slabim i pasivnim izmjeničnim sustavima, te je smanjila proizvodnju harmonika, a time i potreban prostor radi smanjene potrebe za filterima. Zbog navedenih prednosti, pretvarači s naponskim ulazom pogodni su za povezivanje udaljenih vjetroelektrana na moru te povećanje upravljivosti u izmjeničnim mrežama. Međutim, nabrojane prednosti dolaze s višom cijenom pretvarača i većim gubicima izmjenično-istosmjerne pretvorbe.

Ubrzani razvoj pretvarača s naponskim ulazom doveo je do pojave više različitih topologija u relativno kratkom vremenu. U radu su opisane, te se koriste dvorazinska i modularna višerazinska

topologija pretvarača u polumosnom spoju. Glavne prednosti modularnih višerazinskih pretvarača su manji gubici pretvorbe i smanjena proizvodnja harmonika. Međutim, broj potrebnih elektroničkih ventila dvostruko je veći.

Pretvarači s naponskim ulazom omogućili su implementaciju visokonaponskih istosmjernih mreža električne energije budući da se suprotan tok snage postiže promjenom smjera struje, a ne promjenom polariteta napona kao što je to slučaj kod mrežom komutiranih pretvarača. Visokonaponske istosmjerne mreže i razni aspekti njihova pogona, upravljanja i zaštite privukli su snažan interes istraživača širom svijeta. U izmjeničnoj mreži, sve više pretvarača nalazi se u električnoj blizini (eng. multi-infeed systems), te mnogi aspekti takvih sustava također nisu dovoljno istraženi.

Visokonaponski istosmjerni sustavi dinamički su sustavi sa složenim sustavom upravljanja i značajno manjim vremenskim konstantama u usporedbi s izmjeničnim elektroenergetskim sustavima. Stabilnost takvih sustava stoga je osobito važno pitanje koje zahtijeva posebnu pažnju. Stabilnost dinamičkih sustava općenito možemo podijeliti na stabilnost slaboga signala (ili stabilnost pri malim poremećajima) te na prijelaznu stabilnost (ili stabilnost pri velikim poremećajima). Ovaj rad posvećen je istraživanju značajki stabilnosti slaboga signala visokonaponskih istosmjernih mreža te sustava pretvarača u međusobnoj električnoj blizini u izmjeničnim mrežama.

Dinamički sustav je stabilan pri slabome signalu ili lokalno stabilan oko ravnotežne točke ukoliko ostaje u malom prostoru oko ravnotežne točke uslijed malog poremećaja. Poremećaj se smatra malim ukoliko linearizirane jednadžbe sustava precizno opisuju njegovu dinamiku. Linearizacija jednadžbi sustava omogućuje primjenu moćnih alata razvijenih u teoriji upravljanja za procjenu stabilnosti sustava. Analiza stabilnosti slaboga signala stoga je jedna od najvažnijih metoda za istraživanje inherentnih karakteristika dinamičkih sustava, te se vrlo često koristi u njihovom dizajnu. Ova analiza također se vrlo često koristi i u izmjeničnim elektroenergetskim sustavima gdje je povezana s utvrđivanjem oscilacija niskih frekvencija između sinkronih generatora. Za procjenu stabilnosti slaboga signala u ovome radu koriste se svojstvene vrijednosti koje se računaju pomoću matrice stanja dinamičkog sustava. Preduvjet za primjenu analize stabilnosti slaboga signala je dinamički model sustava u prostoru stanja, tj. opisan sustavom diferencijalnih jednadžbi prvoga reda.

U disertaciji se pobliže istražuju sljedeće teme: (i) interakcijske svojstvene vrijednosti ili modovi u visokonaponskim istosmjernim mrežama električne energije; (ii) različite metode upravljanja naponom i jalovom snagom u sustavu dva pretvarača u međusobnoj električnoj blizini u izmjeničnoj mreži; (iii) utjecaj različitih parametara pretvarača i izmjenične mreže na odabir granice između statičkog i dinamičkog modela izmjenične mreže s pretvaračima s naponskim ulazom.

Prvo poglavlje disertacije donosi pregled podloge i motivaciju za navedeno istraživanje, predstavljeni su ciljevi i doprinosi, te struktura samoga rada. Drugo i treće poglavlje uvodna su poglavlja nužna za sveobuhvatno razumijevanje provedenoga istraživanja. U drugome poglavlju sistematično je opisana tehnologija visokonaponskog istosmjernog prijenosa električne energije, počevši od pojedinačnih elektroničkih ventila preko topologija do pretvaračkih stanica. Okarakterizirani su prednosti i nedostaci mrežom komutiranih i pretvarača s naponskim ulazom, te su istaknuta najnovija tehnološka dostignuća kao i značajni projekti visokonaponskog istosmjernog prijenosa električne energije u svijetu. U trećemu poglavlju predstavljen je metodološki okvir koji se koristi u istraživanju. Prvo je opisan glavni analitički alat koji se koristi u cijeloj disertaciji – analiza stabilnosti slaboga signala temeljena na svojstvenim vrijednostima. Zatim su sistematično izvedeni modeli dvorazinske i modularne višerazinske topologije pretvarača u prostoru stanja. Naposljetku su predstavljene i opisane glavne metode regulacije napona u istosmjernim mrežama.

Četvrto poglavlje počinje istraživanjem interakcijskih svojstvenih vrijednosti ili modova u visokonaponskim istosmjernim mrežama električne energije. Slično kao i u izmjeničnim mrežama, svojstvene vrijednosti možemo podijeliti na lokalne i interakcijske. Interkacijske svojstvene vrijednosti su svojstvene vrijednosti u kojima sudjeluju (participiraju) varijable stanja više različitih podsustava. Nadalje, dominantna svojstvena vrijednost je svojstvena vrijednost najbliža ishodištu koordinatnog sustava i ima najveći utjecaj na odziv sustava. Interakcijske svojstvene vrijednosti proučavane su u radijalnoj visokonaponskoj istosmjernoj mreži s tri pretvarača u kojoj samo jedan pretvarač sudjeluju u regulaciji napona mreže, dok ostali pretvarači reguliraju (radnu) snagu (eng. voltage margin control). Cilj istraživanja bio je utvrditi ponašanje interakcijskih svojstvenih vrijednosti s obzirom na radnu točku i strukturu mreže, budući da ovakvo istraživanje nije sustavno provedeno prije u literaturi. Pokazuje se kako dominantna svojstvena vrijednost postaje stabilnija povećanjem radne snage pretvarača zaduženog za regulaciju napona u mreži te

sa simetričnim opterećenjem pretvarača u mreži. Suprotno, dominantna svojstvena vrijednost postaje manje stabilna povećanjem električne udaljenosti između pretvarača te povećanjem napona u istosmjernoj mreži. Dakle, stabilnost dominantne svojstvene vrijednosti, a time i cijeloga sustava, postaje ugrožena u slučaju malog toka snage, a osobito u mrežama s relativno dugačkim kabelskim vodovima.

Na temelju provedenih analiza, u nastavku četvrtoga poglavlja, razrađena je strategija za odabir pretvarača za regulaciju napona u mreži s ciljem postizanja što veće stabilnosti dominantne interakcijske svojstvene vrijednosti. Pokazano je kako struja pretvarača u kombinaciji s njegovom snagom preciznije određuje stabilnost dominantnog interakcijskog moda. Dobiveni principi potvrđeni su za dvije klase topologija istosmjernih mreža: za mreže u radijalnoj konfiguraciji s proizvoljnim brojem pretvaračkih stanica te za mreže u trokut spoju. Naposljetku, strategija za odabir pretvarača za regulaciju napona generalizirana je s obzirom na distribuirano upravljanje naponom pomoću proporcionalnih regulatora (eng. voltage droop control), te je kao rezultat dobivena metoda za podešavanje koeficijenata proporcionalnih regulatora. Ukoliko je redoslijed koeficijenata proporcionalnih regulatora jednak redoslijedu stabilnosti dominantnog interakcijskog moda (u slučaju kada je samo jedan pretvarač zadužen za regulaciju napona), tada je stabilnost dominantnog interakcijskog moda u mreži s distribuiranim upravljanjem naponom najveća.

Evaluacija različitih vanjskih upravljačkih krugova za regulaciju napona i jalove snage s aspekta stabilnosti slaboga signala provedena je u petome poglavlju na generičkom modelu više pretvaračkih stanica u međusobnoj električnoj blizini u izmjeničnoj mreži. Ovakvi sustavi opsežno su istraživani u slučaju mrežom komutiranih pretvarača, dok su istraživanja s pretvaračima s naponskim ulazom značajno manje zastupljena u literaturi. Proučavani sustav sastoji se od dva modularna višerazinska pretvarača međusobno povezana izmjeničnim vodom i prema vanjskoj mreži koja je modelirana Theveninovim ekvivalentom. Sljedeće metode za regulaciju napona i jalove snage su analizirane: (i) upravljanje konstantnom jalovom snagom, (ii) upravljanje konstantnim izmjeničnim naponom, (iii) kombinirano upravljanje jalovom snagom i izmjeničnim naponom pomoću proporcionalnog regulatora, (iv) upravljanje naponom udaljene sabirnice u izmjeničnoj mreži. Vrsta upravljanja koja je implementirana u pretvaraču s nižom snagom kratkog spoja u točki veze s izmjeničnom mrežom (dalje od vanjske mreže) ima veći utjecaj na odziv sustava u usporedbi s vrstom upravljanja koje je implementirano u pretvaraču s višom snagom

kratkog spoja (bliže vanjskoj mreži). Pokazano je i obrazloženo kako upravljanje konstantnim izmjeničnim naponom u pretvaraču koji se nalazi dalje od vanjske mreže dodatno narušava stabilnost najmanje stabilne svojstvene vrijednosti u usporedbi s upravljanjem konstantnom jalovom snagom u istome pretvaraču. U kombiniranom upravljanju jalovom snagom i izmjeničnim naponom, više vrijednosti koeficijenata proporcionalnih regulatora moguće su u slučaju kada je ova vrsta upravljanja implementirana u pretvaraču s višom snagom kratkog spoja u točki veze s izmjeničnom mrežom. Kod upravljanja naponom udaljene sabirnice, lokacija, odnosno udaljenost sabirnice od pretvarača, nema značajan utjecaj na stabilnost slaboga signala u proučavanome sustavu.

Istraživanje sustava dvije pretvaračke stanice u međusobnoj električnoj blizini u izmjeničnoj mreži dodatno je prošireno analizom sudjelovanja pojedinih podsustava u promatranim svojstvenim vrijednostima te sagledavanjem utjecaja duljine i radne snage na izmjeničnome vodu. Povećanje duljine izmjeničnoga voda općenito ima negativan utjecaj na stabilnost sustava, dok smanjivanje toka radne snage na vodu nema jednoznačan utjecaj na njegovu stabilnost. Analiza sudjelovanja pojedinih podsustava otkriva kako nizak tok radne snage i povećanje duljine izmjeničnoga voda općenito ima pozitivan razdvajajući efekt na upravljanje radnom snagom i ukupnom kapacitivnom energijom pojedinih pretvarača. Naposljetku, pokazano je kako statički model izmjeničnog voda precjenjuje stabilnost sustava čime je naglašena važnost odgovarajućeg modeliranja izmjeničnog voda u frekvencijskoj domeni.

Sve veća primjena uređaja energetske elektronike u modernim elektroenergetskim sustavima povećava raspon frekvencija mogućih dinamičkih međudjelovanja između sinkronih generatora, izmjeničnih vodova i uređaja energetske elektronike. U tom smislu, mijenja se tradicionalni pogled na stabilnost slaboga signala u izmjeničnim mrežama. Statičkim modelom izmjenične mreže nije moguće identificirati fenomene prvi višim frekvencijama, stoga su potrebni dinamički modeli prijenosnoga sustava. S druge pak strane, dinamičko modeliranje cijele izmjenične mreže može dovesti do velikih modela u prostoru stanja iz kojih postaje teško računati svojstvene vrijednosti. Kao rješenje problema, u literaturi su predloženi hibridni modeli u kojima je izmjenična mreža u blizini uređaja energetske elektronike modelirana dinamički, a ostatak mreže statički. Međutim, istraživanje granice između statičkog i dinamičkog modela izmjenične mreže s aspekta stabilnosti slaboga signala zasada nije sustavno istraživano u literaturi. U šestome

poglavlju ovoga rada, stoga je predložena procedura za usporedbu različitih modela izmjenične mreže utemeljena na analizi svojstvenih vrijednosti kako bi se utvrdili parametri pretvarača i izmjenične mreže s najvećim utjecajem na odabir granice između statičkog i dinamičkog modela izmjenične mreže. Predložena procedura primijenjena je na primjeru IEEE 39 mreže s jednom te s dvije pretvaračke stanice.

Na temelju provedenih istraživanja utvrđeno je kako snaga kratkog spoja u točki veze pretvarača s izmjeničnom mrežom ima značajan utjecaj na točnost statičkog modela izmjenične mreže s jednom pretvaračkom stanicom. Nadalje, među proučavanim parametrima pretvarača (brzina fazno spregnute petlje, brzina upravljanja radnom snagom, količina radne snage, vrsta upravljanja jalovom snagom), brzina fazno spregnute petlje ima najveći utjecaj na točnost statičkog i hibridnih modela izmjenične mreže. Stoga u slučaju brzog upravljanja fazno spregnute petlje i/ili male snage kratkog spoja u točki veze pretvarača s izmjeničnom mrežom, veći dio izmjenične mreže u okolici pretvarača mora biti modeliran dinamički. Naposljetku, istraživan je utjecaj duljina izmjeničnih vodova u blizini pretvaračkih stanica. Sakupljeni podaci potvrđuju kako se u slučaju dinamičkog modeliranja dugačkih vodova u okolici pretvaračkih stanica postiže značajno povećanje točnosti hibridnih modela izmjenične mreže. Ovo je osobito naglašeno kod brzog upravljanja fazno spregnute petlje.

Znanstveni doprinos ove doktorske disertacije može se sažeto predstaviti sa sljedećim:

- određivanje značajki interakcijskih svojstvenih vrijednosti visokonaponske istosmjerne mreže s obzirom na radnu točku i strukturu mreže,
- metoda za podešavanje koeficijenata proporcionalnih regulatora za distribuirano upravljanje naponom visokonaponske istosmjerne mreže,
- vrednovanje različitih metoda regulacije napona i jalove snage u izmjeničnoj mreži s više pretvaračkih stanica, te
- utvrđivanje parametara pretvarača i izmjenične mreže relevantnih za odabir granice između statičkog i dinamičkog modela izmjenične mreže s pretvaračima s naponskim ulazom.

Ključne riječi: visokonaponski istosmjerni prijenos električne energije, pretvarači s naponskim ulazom, sustav pretvarača u međusobnoj električnoj blizini u izmjeničnoj mreži, analiza stabilnosti slaboga signala

Contents

1. INTRODUCTION

1.1. Background and motivation

The invention of the polyphase induction machine by Nikola Tesla and the power transformer by Lucien Gaulard and John Dixon Gibbs at the end of the 19th century marked the termination of the so-called war of currents. These inventions enabled the dominance of alternating current in electric power transmission. However, the advantages of DC transmission have never been forgotten. The goal of subsequent developments in DC technology has not been to substitute the AC technology but to upgrade and reinforce existing AC transmission systems.

A techno-economic comparison [1, 2] indicates that high-voltage direct-current (HVDC) transmission typically becomes competitive for distances around 400–600 km for overhead lines and already at 30–50 km for cable connections. Investments in DC terminals are much higher compared to those in AC terminals. However, this high initial cost is offset by lower DC line costs per km compared with AC line costs. Long AC lines require reactive power compensation, and AC cables experience high charging currents. HVDC transmission does not experience any stability limits related to transmission distance or active power amount. Moreover, DC transmission lines have a smaller right-of-way, do not emit a varying electromagnetic field, have smaller active power losses (no skin or proximity effects), do not contribute to the fault current, and have increased controllability. Besides the high terminal costs, disadvantages of the HVDC transmission are, depending on the technology employed, production of harmonics and reactive power compensation.

HVDC technology with line-commutated converters based on thyristors (LCC HVDC) has been used for decades for long-distance bulk power transmission and asynchronous connections. A long-distance bulk power transmission is employed primarily in geographically large countries, such as China, India, and Brazil while power and voltage ratings reach as high as 8 GW and ±800 kV [3, 4]. Asynchronous connections are applied for connecting asynchronous AC grids or AC grids with different frequencies. Examples can be found in the United States, Japan, India, and others [3, 4]. If such connections have very short DC lines (or do not have them at all) they are called back-to-back connections. In addition, HVDC lines are also often a preferred solution in

situations where it is difficult to obtain permits for overhead line construction since they have a smaller right-of-way and have the possibility to use long underground/undersea cables.

Only relatively recently—with the advancement of voltage source converters (VSCs) based on transistors at the end of the 20th century—has HVDC transmission unfolded new possibilities. The main advantages of VSCs are the possibilities: (i) to independently control active and reactive power, contrary to LCCs which always consume reactive power; (ii) to connect to weak or even passive AC grids; and (iii) to offer black-start capability whereas LCCs require a strong AC grid necessary for commutation. Moreover, VSCs produce fewer harmonics and consequently occupy less space since filter requirements are significantly reduced. Because of this, VSC technology is suitable for the connection of remote offshore wind power plants. Additionally, VSCs can offer further controllability and flexibility to the AC grid, which becomes especially beneficial with larger renewable energy sources penetration and in today's market-oriented power systems. Advantages of VSCs come at higher converter costs and increased switching losses. On the contrary, LCCs still have significantly higher power ratings and slightly smaller losses. Hence, they remain the preferred technology for long distance bulk power transmission.

Another advantage of VSCs is related to the implementation of multi-terminal direct-current (MTDC) grids, in which three or more converters are interconnected on the DC side. Power reversal with LCCs can only be achieved by changing the voltage polarity, so in multi-terminal configuration, complex mechanical switchgear is required. Conversely, with VSCs, power reversal is achieved by changing the current direction, so the implementation of MTDC grids is much easier. Currently, there are two operational VSC HVDC grids in the world, both in China [5, 6], and a third is being built there too [7]. In Europe, the most promising region for the implementation of a DC grid is the North Sea [8, 9] for several reasons: vast wind power reserves, proximity to three asynchronous AC grids and offshore loads (oil and gas platforms). Plans for HVDC grids also exist in other parts of the world, such as the United States [10, 11].

The accelerated development of VSCs has led to the invention of several different configurations in a relatively short period of time, namely two-level, three-level and modular multilevel converters (MMCs). The main advantages of MMCs in comparison to two- and three-level topology are lower losses and lower harmonics production. However, this comes at a cost of double (or four times) the number of semiconductor switches. MMCs are considered a preferred

topology for high-voltage applications while two-level converters remain suitable for low-voltage applications.

Fig. 1.1 illustrates the layout of HVDC transmission systems. The main obstacle for a wide implementation of MTDC grids is the further development and commercialization of high-power DC breakers. However, DC grids and all aspects of their operation, control, and protection have attracted a high interest in the research community worldwide. Since more HVDC schemes are being employed, either as point-to-point lines or MTDC grids, converters are being built in each other's mutual electrical proximity in AC systems. These configurations are called multi-infeed HVDC (MI-HVDC) and many aspects of their interaction have remained insufficiently explored in the case of VSCs.

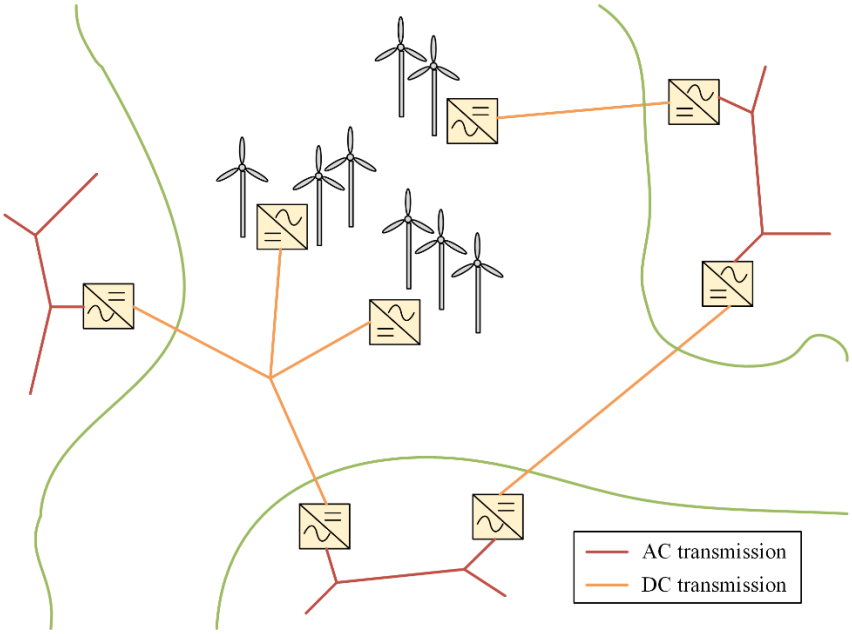

Figure 1.1: Layout of VSC-based HVDC transmission systems

HVDC transmission systems are dynamic systems characterized by complex control and much faster dynamics compared with AC transmission. Hence, stability questions are of great concern and require thorough assessment. System stability is generally classified into small-signal and transient stability. The focus of the research in this thesis is small-signal stability analysis (SSSA).

A dynamic system is said to be stable in small signals or locally stable around an equilibrium point if it remains within a small region surrounding the equilibrium point when it is

subjected to a small disturbance [12]. A disturbance is considered small enough if the equations describing the system can be linearized and still accurately capture the system's dynamics. A linearization of the system equations enables the application of powerful techniques developed in control theory for evaluating stability. SSSA is therefore one of the most important methods for studying the inherent characteristics of dynamic systems and is often used as a tool for system design. It is widely used in AC power systems, where it is typically used to assess low-frequency rotor angle oscillations. In this work, eigenvalue-based SSSA is the main analytical tool used to assess the stability properties of VSC-based HVDC grids and MI-HVDC systems.

1.2. Objectives and contribution of the thesis

The first subject matter of the conducted research is related to the small-signal stability of VSC-based HVDC grid with voltage margin control. More precisely, it is associated with the stability properties of interaction modes—modes in which state variables from more than one subsystem participate (converters in this case). The goal is to determine the behavior of interaction modes with respect to the operating point and structure of an HVDC grid since this type of analysis has not been carried out thoroughly in literature so far. More specifically, the considered parameters are the transmitted power in the grid, the selection of a voltage controlling converter, the power of a voltage controlling converter, the power of other converters, the reference voltage, the length of cables, and the grid topology. Based on the determined properties, the intention is (i) to propose a method for the grid voltage control with the largest stability margin of the dominant interaction mode and (ii) to generalize the method with respect to the grid structure and the voltage droop control in which several converters participate in the HVDC grid voltage regulation.

The second research subject is associated with the influence of different voltage and reactive power regulation methods on the small-signal stability of the VSC-based MI-HVDC systems. For VSC technology, several aspects of MI-HVDC system operation are less well understood compared to LCC HVDC systems. The objective here is to evaluate the small-signal stability properties of the following control methods: constant reactive power control, constant AC voltage control, AC voltage droop control, and remote bus voltage control. The assessment will be expanded by the subsystem participation analysis of selected system modes and the investigation of the influence of (i) the short-circuit ratio (SCR) at converter's point of common coupling (PCC), (ii) the AC line length, and (iii) the power flow between converters.

The final topic of the conducted research is the importance of appropriate AC line modeling in an AC grid with VSC HVDC infeeds. A hybrid network model was proposed in [13], in which the AC grid is modeled dynamically in the vicinity of a dynamic device (FACTS, HVDC) and the rest of the grid statically or in a steady state. However, the extent of the AC grid that needs to be modeled dynamically has not been investigated so far. Therefore, the thesis aims to determine the converter and AC grid parameters relevant to the boundary selection between the dynamically and statically modeled parts of an AC grid. This is carried out using a comparison procedure based on SSSA and for a single and double VSC HVDC infeed in a relatively larger AC grid.

The scientific contribution of this thesis can be summarized as follows:

1. Assessment of properties of HVDC grid interaction eigenvalues with respect to the operating point and grid structure;
2. Method for tuning coefficients of voltage droop control in HVDC grids;
3. Evaluation of different voltage and reactive power regulation methods in multi-infeed HVDC systems;
4. Determination of converter and grid parameters relevant to the boundary selection between a dynamic and a static AC grid model with voltage source converters.

1.3. Thesis outline

The thesis is organized in the following way. Chapters 2 and 3 are introductory chapters necessary for a comprehensive understanding of the conducted research. Chapter 2 systematically presents HVDC technology starting from power electronic switches to topologies and converter stations for the two types of converter technologies employed nowadays in HVDC transmission: LCCs and VSCs. Chapter 3 provides a methodological and modeling framework used in the research. First, an eigenvalue-based small-signal analysis, the main analytical tool used throughout the thesis, is described. Afterward, the state-space models of two-level and MMCs are systematically derived, and finally, the DC grid voltage control methods are presented and described.

The main contributions of the thesis are presented in Chapters 4 to 6, which present modified versions of published or submitted papers. Chapter 4 investigates the influence of the operating point and the grid structure on the stability of interaction modes in an HVDC grid. Based

on the conducted analyses, the method for tuning coefficients in the voltage droop control of an HVDC grid is proposed. The evaluation of different voltage and reactive power control methods in MI-HVDC is presented in Chapter 5. In Chapter 6, the comparison procedure of different AC grid models based on small-signal analysis is introduced to determine the most relevant converter and grid parameters in the boundary selection between a dynamic and a static AC grid model including VSCs. Finally, the main conclusions and the proposal for future work are summarized in Chapter 7.

2. POWER ELECTRONICS IN HIGH-VOLTAGE DIRECT-CURRENT TRANSMISSION

Parts of this chapter have been presented and published in: G. Grdenić and M. Delimar "Energetska elektronika u visokonaponskom istosmjernom prijenosu električne energije," in 14th HRO CIGRÉ Session, Šibenik, 2019. [14]

Although AC transmission is predominantly used in electrical power systems, DC transmission is still utilized in several different applications. These are typically the interconnection of asynchronous grids, long-distance cable connections, and bulk power transmission using overhead lines. The main drivers for an increased use of HVDC in developed countries are renewable energy integration (especially offshore wind power plants), the liberalization of electricity markets and difficulties in obtaining construction permits for new overhead lines. In large countries with high growth in energy demand (China, India, Brazil), HVDC is increasingly being used for long-distance electricity transmission from production to load centers.

The first commercial HVDC line was built in 1954 connecting the island of Gotland to mainland Sweden [15]. It was based on mercury-arc valves. However, because of the inherent drawbacks of mercury-arc technology and the development of solid-state converters, this type of HVDC line is not used anymore. Nowadays, there are two types of power electronic converters in the application in HVDC transmission:

- Line-commutated converters (LCCs) based on half-controlled semiconductor switches (thyristors)
- Self-commutated converters (SCCs), or forced-commutated converters, based on fully controlled semiconductor switches (transistors)

Considering the direct source they are using, converters can have a current or a voltage source. SCCs can have a direct current or a voltage source, while LCCs can only have a current source. However, in HVDC applications, LCCs are usually referred to as current source converters (CSCs) and SCCs are referred to as VSCs. The structure, topology, and operation of these converters are described in the following sections.

2.1. Line-commutated converters (current source converters)

LCCs have been used in HVDC application for several decades. The first commercial link with thyristors entered into operation in 1972 in Canada [3, 16] until mercury-arc valves had been used. High-voltage lines with LCCs are also called classical or conventional HVDC.

2.1.1. Thyristor technology

Thyristors are electronic valves with a turn-on but no turn-off capability. Although the term *thyristor* is used for the whole family of electronic valves (silicon-controlled rectifiers/SCRs, gate turn-off thyristors/GTOs, triac, MOS-controlled thyristors/MCTs, etc.), it is most often used as a synonym for a silicon-controlled rectifier. Because of their great power, robustness, and high efficiency, thyristors are still massively used in industrial applications. The voltage and current magnitudes of an electronic switch reaches values of 8.5 kV and 4.5 kA, respectively [17].

As seen in Fig. 2.1, a thyristor has four semiconductor layers and three terminals: anode, cathode, and gate. Operation of a thyristor is similar to that of a diode. However, the onset of conduction can be delayed by a control circuit. The current-voltage characteristic of a thyristor is shown in Fig. 2.2. When the thyristor voltage (the voltage between the anode and the cathode) is negative, a thyristor is reverse-blocked and cannot move to the conduction state. The value of the voltage must not exceed a certain threshold to avoid breakdown of the device. If the voltage between the anode and the cathode is positive, a thyristor is in the forward-blocking state. To get to the conduction state, the most common method is to bring a relatively weak and short current impulse to the gate terminal. Like the reverse-blocking voltage, the forward-blocking voltage must not exceed the value of the breakdown voltage. As mentioned earlier, the transition from the conduction to the blocking state cannot be influenced but depends on the external circuit to which a thyristor is connected. A thyristor moves from the conduction state to the blocking state when the anode current crosses zero.

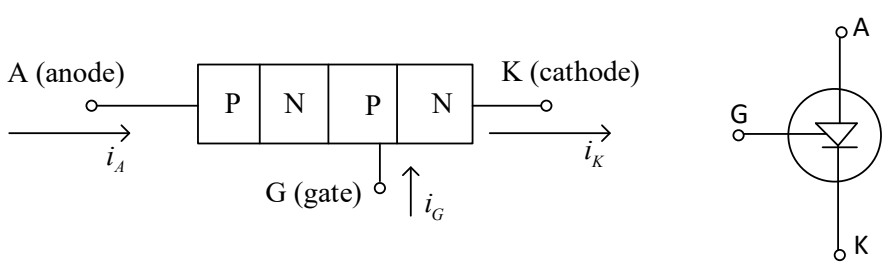

Figure 2.1: Thyristor structure and symbol

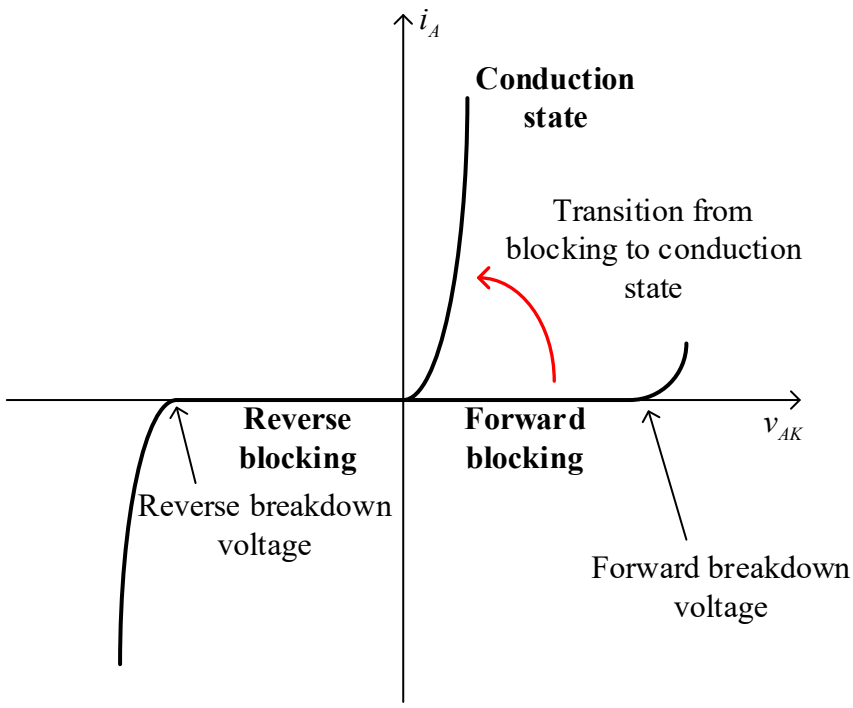

Figure 2.2: Simplified current-voltage characteristic of a thyristor

2.1.2. Topologies of line-commutated converters

To synthesize the DC current from the three-phase alternating current using thyristors, valves are connected in the six-pulse or Graetz bridge. A topology of the three-phase thyristor converter is shown in Fig. 2.3.

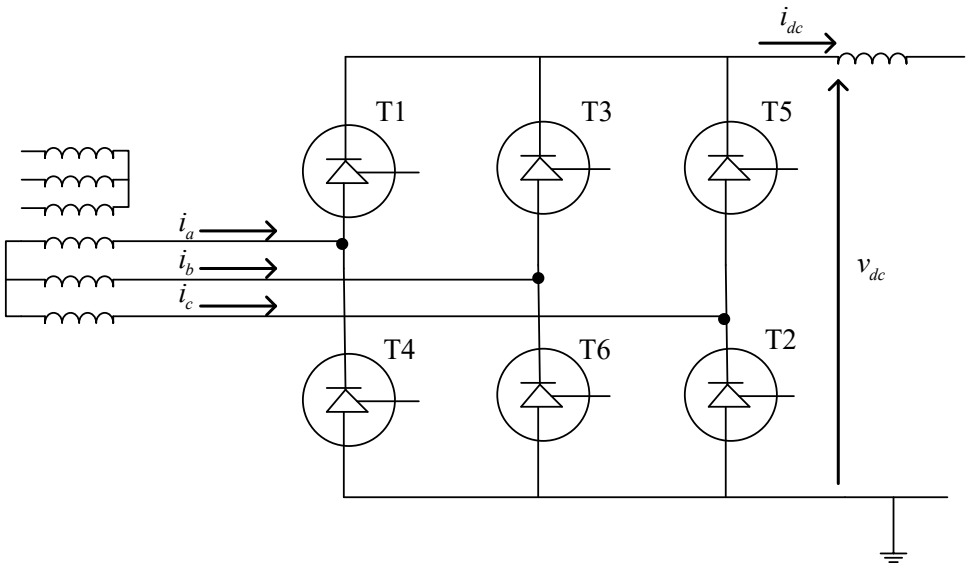

Figure 2.3: Thyristor-based six-pulse converter

In the scope of this work, only the situation with a firing angle equal to zero and no commutation overlap is considered in detail. Thyristors in this case eventually behave as diodes, that is, they start conducting when voltage between the anode and the cathode is positive. At each moment, exactly two thyristors conduct current since the commutation overlap is neglected. Fig. 2.4 illustrates a symmetrical and balanced three-phase system used to synthesize DC voltage. Since one period of the AC signal corresponds to six pulses of the DC voltage, this topology is named a six-pulse converter. At the beginning of a period, thyristors T6 and T1 conduct; at one-sixth of the period, T6 switches off and T2 starts conducting, and so on. Table 1 shows the order of thyristors conducting the current during an AC period. The average value of direct voltage can be calculated by averaging the surface below the $v_{dc,o}$ curve:

$$v_{dc,o} = \frac{3\sqrt{2}}{\pi} V_{LL} , \tag{2.1}$$

where V_{PLL} is the effective value of line-to-line AC voltage.

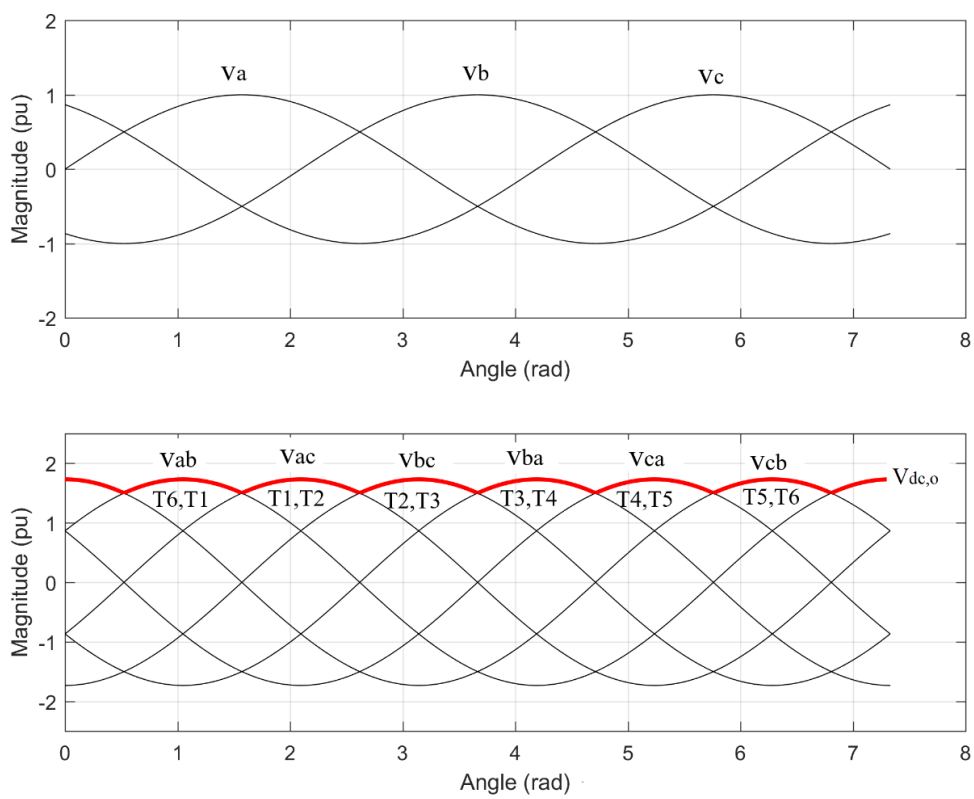

Figure 2.4: Three-phase AC voltage and DC voltage obtained with a thyristor-based six-pulse converter

Table 2.1: Sequence of thyristor conduction in one period of an AC signal

Time	Thyristors
0—1/6 T	T1, T2
1/6 T—2/6 T	T2, T3
2/6 T—3/6 T	T3, T4
3/6 T—4/6 T	T4, T5
4/6 T—5/6 T	T5, T6
5/6 T—6/6 T	T6, T1

On the DC side, harmonics of order 6n appear, and on the AC side of order 6n±1, as explained in [12]. To reduce the production of harmonics, instead of a six-pulse configuration, a 12-pulse configuration, shown in Fig. 2.5, is employed. It consists of two six-pulse bridges connected in series. By using this configuration, harmonics of order 5, 7, 17, 19, . . . are canceled out, so harmonics of order 12n±1 appear on the AC side, and harmonics of order 12n appear on the DC side. This is accomplished by connecting one Graetz bridge via a transformer with a wye (Y) connection, and the other via a transformer with a delta (Δ) connection. This way, the AC voltage is shifted by 30°. More details on this can be found in [12, 17].

The possibility of changing the thyristor firing angle enables control of the DC voltage and consequently the active power flow. The resulting voltage in the firing-angle control is equal to

$$v_{dc} = \frac{3\sqrt{2}}{\pi} V_{LL} \cdot \cos\alpha = v_{dc,o} \cdot \cos\alpha \,. \tag{2.2}$$

The value of the firing angle is in the range of 0° to 180° (with the commutation overlap neglected), so it is possible to produce negative voltages on the DC side for firing-angle values higher than 90° when the converter operates as an inverter. In this case, the current still flows in the same direction, but since the voltage on the DC side is negative, the power is also negative, that is, it flows in the opposite direction.

At the end of this section, it needs to be emphasized that to obtain a high-voltage level, each electronic valve in Figs. 2.3 and 2.5 actually consists of several hundred individual thyristors connected in series for HVDC applications. At the same time, it is necessary to ensure equal loading of all individual switches, as well as the simultaneity of their switching. Parallel connection, employed to achieve necessary current ratings, is usually not required because of the sufficient current ratings of individual thyristors.

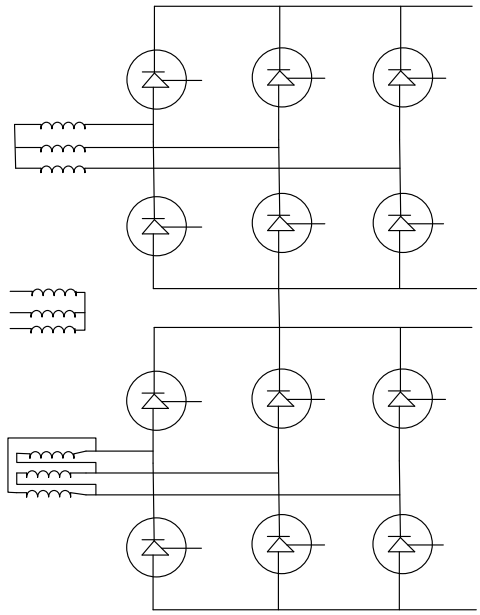

Figure 2.5: Thyristor-based 12-pulse converter

2.1.3. HVDC line with line-commutated converters

An LCC HVDC line, apart from converters, consists of several other components: power transformers, circuit breakers (CBs), smoothing reactors, AC and DC filters, reactive power compensation, earthing, and return path. All these elements, as well as the control circuit, are shown in Fig. 2.6.

Theoretically, power transformers are not necessary but are almost always used, as they enable DC voltage regulation independently from the state in the AC grid (regulating transformers). They also facilitate the application of a 12-pulse configuration and contribute to reduction of short-circuit currents. Since the currents passing through transformers contain a significant amount of harmonics, they have a more robust construction in comparison to standard grid transformers to prevent excessive heating.

When thyristor-based converters are used, reactive power compensation needs to be secured. Namely, the firing-angle control causes lagging of the current. Reactive power compensation accounts for around 60% of converter nominal power [17]. Capacitor banks are the most common and the most economical solution if there are no nearby generators to provide necessary reactive power. Because of the significant amount of produced harmonics, filters are placed on the AC and to a much smaller extent on the DC side. An additional reactor is placed on the DC side to smoothen the DC current. The converter control system is capable of resolving

transient faults, but mechanical CBs are necessary for isolating permanent disturbances. The return connection is most often in the form of a simple metal conductor because grid codes in most countries prohibit the return current flow through ground or sea. Besides the monopolar configuration shown in Fig. 2.6, there are also bipolar and homopolar DC line configurations.

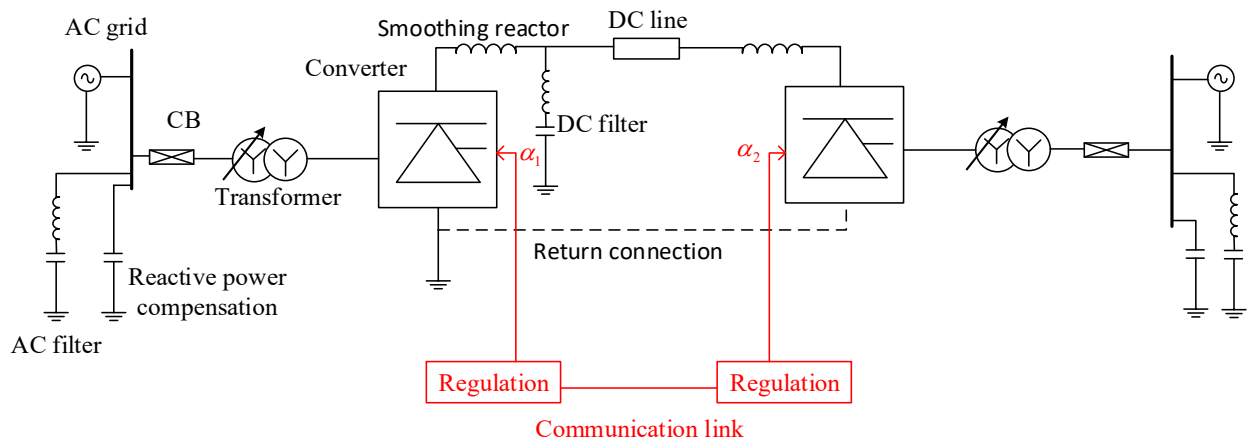

Figure 2.6: Monopolar configuration of an LCC HVDC line

Firing-angle control (in Fig. 2.6. in red) enables regulation of DC line voltage while additional voltage regulation is provided by regulating transformers. Control of LCC HVDC lines requires a direct communication link between the rectifier and the inverter.

Disadvantages of the LCC HVDC technology are the following:

- need for reactive power compensation
- production of a significant amount of harmonics
- susceptibility to commutation failures
- operation is possible only in relatively strong AC networks
- complicated implementation of DC grids because a bidirectional power flow is only possible by changing voltage polarity (since a thyristor can conduct current only in one direction)
- necessary communication link between terminals although an HVDC line can operate in the event of a loss of a communication link

Attempts to further develop power converters are being carried out to overcome these drawbacks. However, LCCs retain some important benefits: high power, low price, and small conversion losses

(<1%) [17]. Currently, there are more than 150 LCC-based HVDC links [3, 4, 18, 19], and because of the mentioned advantages and long operation experience, they are still being constructed. Two 8 GW ±800kV lines are in operation in China [4], and the largest LCC HVDC link is being built there as well. It should be capable of transmitting 12 GW of electricity at ±1100 kV voltage level from the Xinjiang region in the Northwest to the Anhui province in Eastern China [20].

2.2. Voltage source converters (self-commutated converters)

The first transmission line with a VSC was built in 1999 connecting the Swedish island of Gotland with the mainland [3, 21]. Application of new transistor technology has overcome some important drawbacks of LCCs:

- possibility to connect to weak AC grids
- reactive power regulation
- lower harmonics production and hence a smaller size of converter stations
- bidirectional power flow is enabled by changing current direction (it is not necessary to change voltage polarity; hence, the use of conventional cross-linked polyethylene cables/XLPE is enabled)
- reduced communication requirements between converter stations

More than 30 VSC HVDC lines have been built by 2019, and a dozen more are being constructed [3, 18, 22].

2.2.1. Transistor technology

VSCs (or SCCs) contain valves made of one of the following two groups of electronic devices [17]:

- insulated gate bipolar transistors (IGBTs),
- integrated gate commutated-thyristors (IGCTs).

These two groups of electronic valves are available at similar voltage levels but represent considerably different technologies. On the one hand, IGBTs are voltage-controlled devices with high switching speeds and simple control requirements. On the other hand, IGCTs have lower conduction losses at the expense of a large and complicated gate drive for equal power. Since IGCTs are more difficult to connect in series and have lower switching speeds, HVDC lines that

have been built use IGBT technology. Therefore, this type of valve is described more closely in the remainder of this section.

IGBTs adopted the advantages of metal-oxide-silicon field-effect transistors (MOSFETs), bipolar junction transistors (BJTs), and GTOs [23]. Similar to the MOSFETs, IGBTs have a high-impedance gate terminal, so a low amount of energy is needed for switching the device on and off. Like BJTs, they have a small on-state voltage in a conduction state, and like GTOs, they can be designed to block negative voltages. IGBTs with voltage ratings up to 6.5 kV are available [17], and for high-voltage applications, similar to thyristors, several hundred valves need to be connected in series. Different from thyristors, to achieve the necessary current rating, several IGBTs need to be connected in parallel (the typical current rating is around 1.2–1.5 kA [17]). A transistor symbol is depicted in Fig. 2.7a, with terminal names: collector, emitter, and gate.

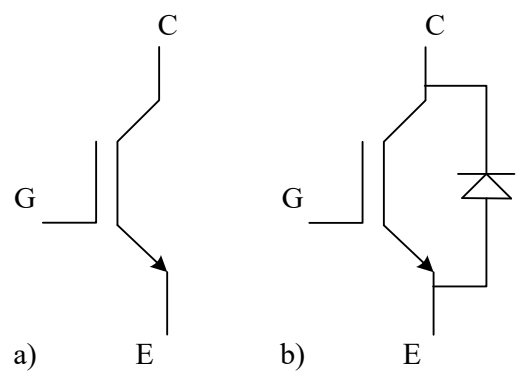

Figure 2.7: a) IGBT symbol; b) IGBT with antiparallel diode

Fig. 2.8 shows the current-voltage characteristic of an IGBT. When the voltage between the collector and the emitter (v_{CE}) is positive, and a gate is short-circuited with the emitter, an IGBT is forward-blocked. To switch the valve from the blocking to the conduction state, it is necessary to bring the gate terminal voltage (v_{GE}) to a sufficient level. When the voltage between the collector and the emitter is negative, the device is in reverse-blocked state. However, reverse blocking is not necessary for typical high-voltage configurations since an antiparallel diode is added to the transistor (symbol in Fig. 2.7b). Antiparallel diodes enable current flow in the opposite direction and protect transistors from reverse overvoltage. These diodes differ from standard rectifier diodes since they must have a fast turn-off behavior to comply with the converter's high operating frequency. The characteristic itself consists of a family of curves that correspond to

different voltage levels at the gate terminal. The collector current is shown in relation to the voltage between the collector and the emitter while the voltage of the gate terminal is constant. In high-voltage applications, an IGBT is always operated in the saturated region of the curve.

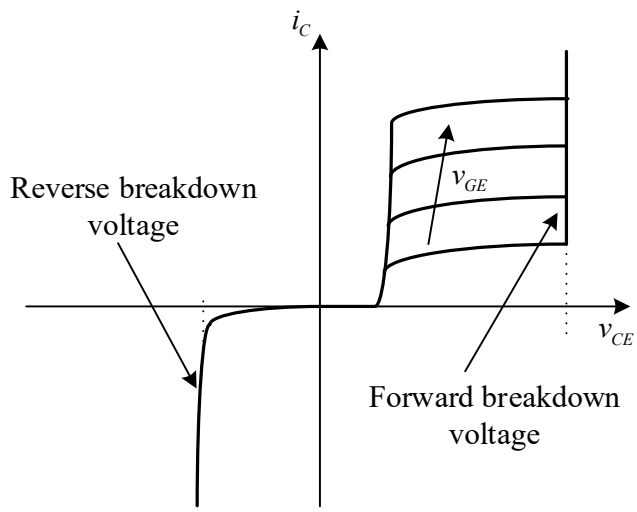

Figure 2.8: IGBT current-voltage characteristic

2.2.2. Topologies of voltage source converters

Several different VSC topologies have been developed. The first commercially available topology was the ABB's two-level configuration ("HVDC Light") depicted in Fig. 2.9. As mentioned above, each valve consists of a sequence of switches connected in series and in parallel.

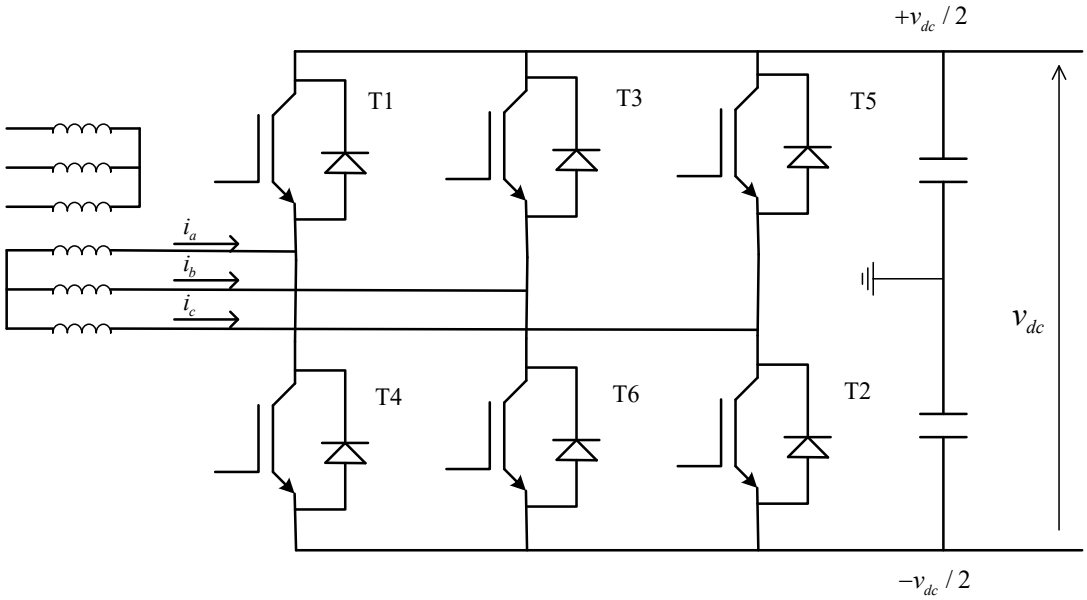

Figure 2.9: Two-level topology of VSC

To produce a sinusoidal signal of fundamental frequency, pulse width modulation (PWM) is used. The AC output voltage is connected to the positive or the negative DC voltage. By varying pulse lengths, a high-frequency voltage signal is synthesized containing the voltage signal of the fundamental frequency, designated with the red color in Fig. 2.10. Although IGBT transistors have relatively low conduction losses, switching frequency up to 2 kHz [1] causes considerable losses: the first generation of two-level VSCs have losses of around 3% [24, 25]. By using new modulation techniques to eliminate higher harmonics such as optimal PWM (OPWM), losses have been reduced to 1.4% [24, 25] of converter nominal power. This is still considerably higher in comparison to LCCs. A large voltage difference at each switching instant also causes large voltage stress (high dv/dt) with this topology, so the high insulation requirements are needed.

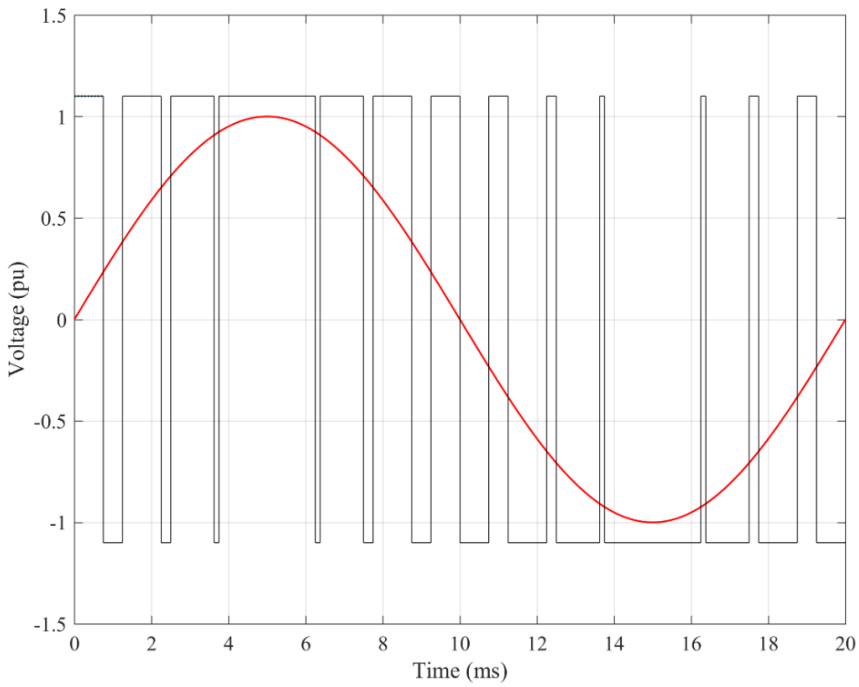

Figure 2.10: Switching pattern of a two-level topology

The primary goal of the further development of different topologies has been to decrease the switching losses. Two types of a three-level topology of VSCs had been developed: neutral point clamped (NPC) and flying capacitor (FC) topology. One converter branch of these two topologies are shown in Figs. 2.11 and 2.12. An NPC topology has two diodes inserted in each converter branch which enable the connection of the output voltage to the third voltage level without increasing the number of electronic switches. A FC topology has an additional capacitor

in each converter branch that also enables the formation of the third voltage level. The switching pattern of a three-level topology is depicted in Fig. 2.13. The application of the third voltage level decreases the voltage stress, and with the smaller voltage step, the switching frequency is also decreased. Consequently, losses have been reduced to 1.8% [24, 25]. However, for this type of converter, it is difficult to comply with grid codes, which require converters to stay in operation during faults in the AC grid to provide reactive power support. This is especially emphasized during asymmetrical short-circuits, so the further development of these topologies has been abandoned. Nevertheless, three-level converters are the preferred topology for medium-voltage applications [26].

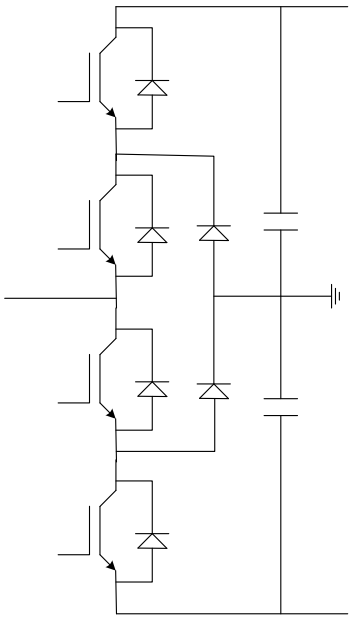

Figure 2.11: Three-level topology with neutral point clamped

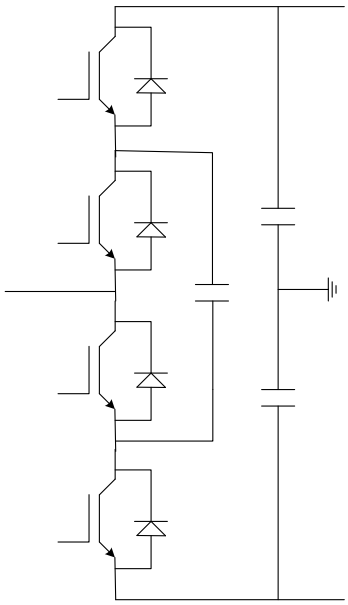

Figure 2.12: Three-level topology with flying capacitor

The latest topology development is represented by MMCs whose modular structure is illustrated in Fig. 2.14. All major manufacturers of power equipment have developed their own type of this converter topology: “HVDC PLUS” (Siemens), “HVDC Light Gen. 4” and “HVDC Light Gen. 5” (ABB), and “HVDC MaxSine” (General Electric/Alstom Grid). Currently, all transmission lines built with this technology use the half-bridge submodules. For the half-bridge configuration, each submodule consists of two switches and a capacitor (Fig. 2.15). Different from the previous topologies, a converter does not have a common large capacitance on the DC side, but the necessary capacitance is distributed among the submodules. If switches S1 and S2 in Fig. 2.15 are considered, the following combinations are possible:

- If S1 is switched on and S2 switched off, a submodule is inserted in a circuit, and the corresponding capacitance contributes to the overall converter voltage.
- If S1 is switched off and S2 switched on, a submodule is bypassed, that is, a submodule does not contribute to the overall converter voltage.
- If S1 and S2 are switched off, a submodule is blocked.

The desired AC voltage is synthesized by varying the number of inserted submodules in the upper and the lower converter arms. The obtained voltage signal no longer has large steps so a lower switching frequency is possible as can be noticed in the switching pattern of the MMC topology with six submodules per arm shown in Fig. 2.17. Switching frequency is around 150 Hz, resulting in significantly lower losses of around 1% [1]. With a large number of submodules, a converter can synthesize the desired signal of the fundamental frequency more precisely. This way, the production of harmonics and the need for filters on the AC side is reduced drastically. All the described advantages come at the expense of twice the number of electronic valves. In addition, the stated drawbacks of IGCT devices are much less significant when employed in MMCs; therefore, the dominant position of IGBTs in MMCs has been questioned [26].

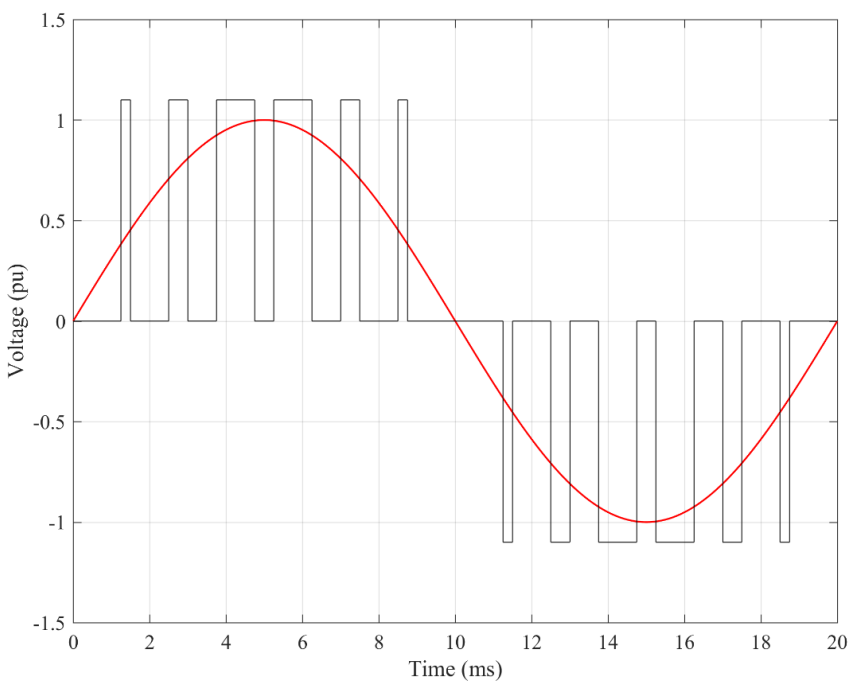

Figure 2.13: Switching pattern of a three-level topology

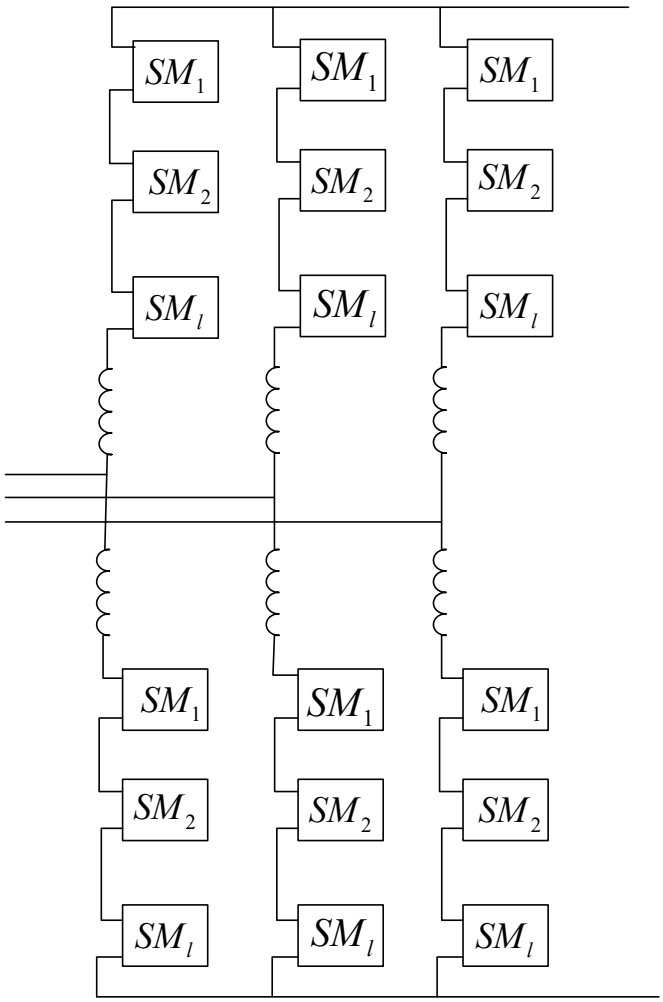

Figure 2.14: MMC topology

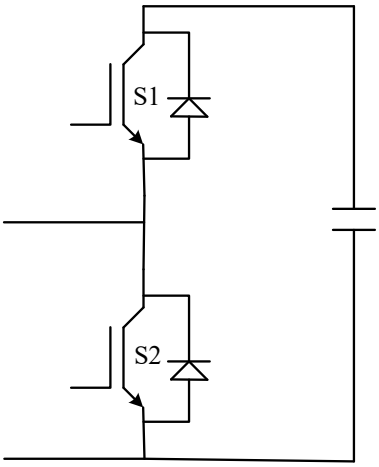

Figure 2.15: Half-bridge submodule

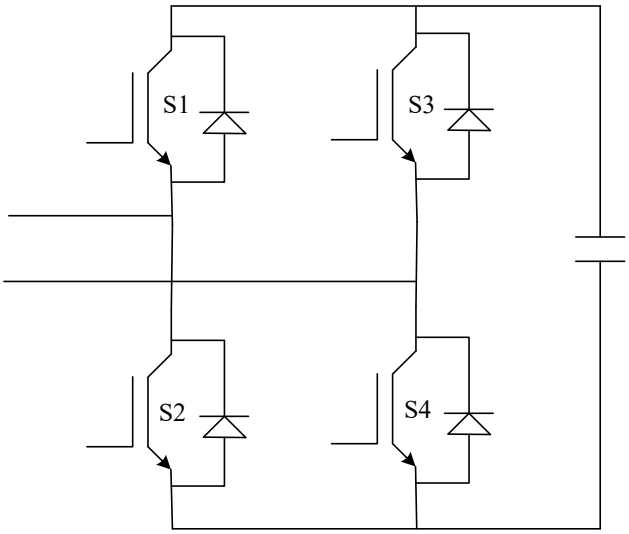

Figure 2.16: Full-bridge submodule

One of the disadvantages of VSC technology in comparison to the LCC is the inability to limit DC fault currents. During the DC fault, antiparallel diodes conduct the fault current, so a VSC behaves like an uncontrolled diode bridge, and the tripping of AC breakers is necessary. Interruption of DC currents is more difficult than that of AC currents since there is no passing of the current through zero and because of much shorter time constants. Several prototypes of DC breakers have been developed so far [17, 26]. For the above reasons, VSC HVDC projects with overhead lines are rare.

However, an MMC with full-bridge submodules, containing four switches and a capacitor (Fig. 2.16), has the ability to block fault currents on the DC side. This comes at the expense of four times the number of switches in comparison to two-level topology. Currently, the first HVDC line with full-bridge submodules is being built in Germany [27, 28]. To reduce the number of necessary electronic switches, researchers have developed schemes containing a combination of two-level topology with a certain number of full-bridge submodules [26, 29]. The development of new topologies continues with the aim to overcome the drawbacks of existing ones.

2.2.3. HVDC line with voltage source converters

A VSC HVDC line, besides converters, include other components as shown in Fig. 2.18 for a two-level topology. As well as in the case of LCCs, connection with an AC grid is implemented through a transformer, which is most often the regulating transformer so that the converter voltage can be optimized with respect to the AC grid voltage. Contrary to LCCs, transformers are not exposed to low-order harmonics; hence, their design is to a large extent similar to that of standard power transformers. Since VSCs produce only high-order harmonics, filter requirements are low, and filters occupy rather a small surface. For MMCs, harmonics production is negligible, and filters can even be omitted. AC CBs are used to interrupt fault currents. The DC voltage is maintained using a large capacitor for a two-level topology while MMCs rely on distributed capacitors within the converter itself. A phase reactor, besides limiting fault currents, is an unavoidable element in converter stations because it enables the independent regulation of active and reactive power by using vector control. Filters on the DC side are rarely employed. The two-level VSC HVDC line shown in Fig. 2.18 uses a symmetric monopolar configuration. It consists of two conductors with opposite voltage polarity, and in the case of an outage of one of the lines, a ground cannot be used as a return path.

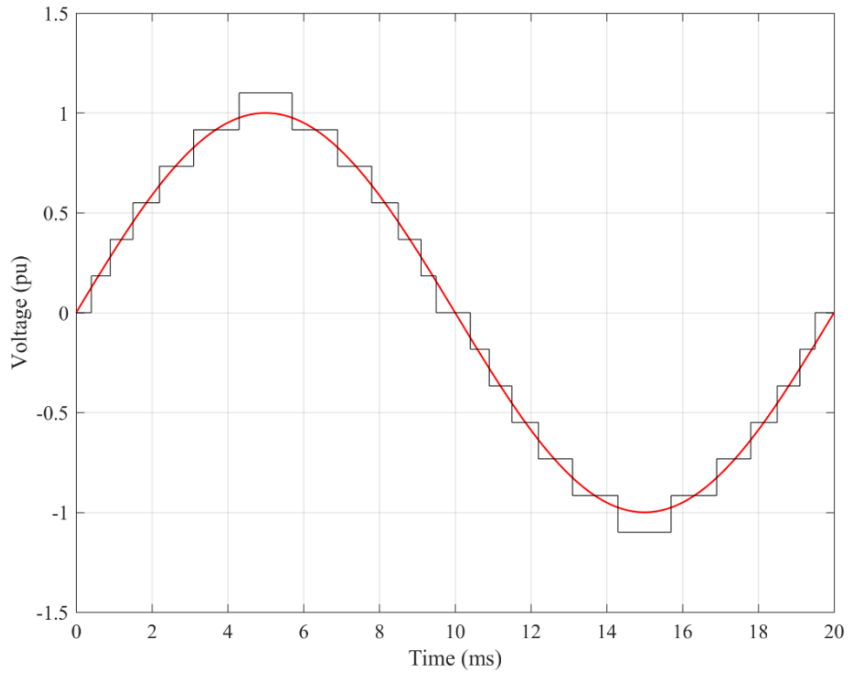

Figure 2.17: Switching pattern of an MMC topology

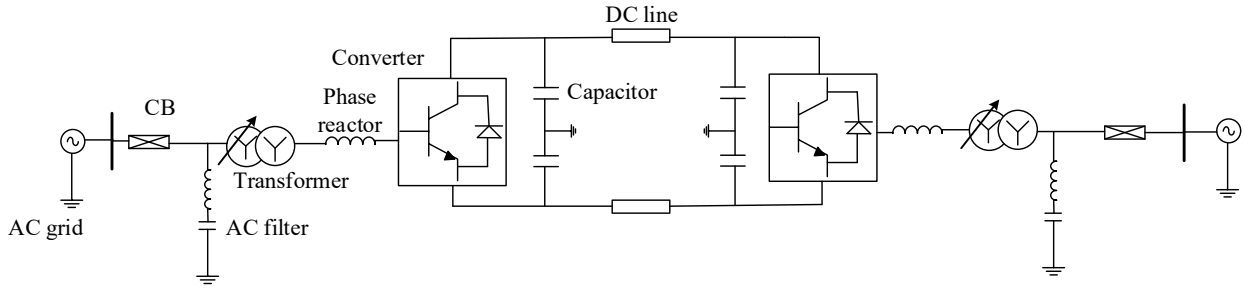

Figure 2.18: Symmetric monopolar configuration of a two-level VSC HVDC line

At the end of this chapter, one more advantage of VSCs in comparison to LCCs needs to be elaborated. VSC technology is much more convenient for developing DC grids. As for LCCs in multi-terminal configuration, fast communication is required because of the coordination of converter operation. Furthermore, power reversal can only be achieved by changing the voltage polarity, hence including mechanical switching. So far, three multi-terminal LCC-based grids have been built: Hydro-Quebec—New England, SACOI (connecting Sardinia and Corsica with mainland Italy), and North-East Agra in India [3, 4, 17, 30]. The first two systems have three terminals, and the last one four. All three grids have a simple line configuration, and developing truly meshed grids with a higher number of terminals is challenging for the above-mentioned

reasons. VSC technology does not face such obstacles. There are limited needs for the coordination between converters and a power reversal does not involve mechanical switching. There are two operational VSC HVDC grids in the world; both have radial configuration and are located in China: the Nanao grid with three terminals [5] and the Zhoushan Islands five-terminal grid [6]. Currently, the largest VSC-based HVDC grid is also being built in China [7]. It will operate at ±500 kV and will have a total capacity of 4500 MW. More importantly, it will be the first truly meshed HVDC grid. However, before a widespread deployment of DC grids, difficulties regarding protection, reliability, and control need to be resolved [31].

2.3. Conclusion

HVDC transmission has become an unavoidable element in modern power systems, and more and more projects are installed and planned worldwide. This chapter has systematically presented two types of converter technologies employed nowadays in HVDC transmission: LCCs and VSCs. Each technology has its advantages and drawbacks and is therefore preferred for different applications. Employment of high-power VSCs in the last decades has enabled new possibilities for HVDC transmission: connection of offshore wind power plants, reactive power support, increasing flexibility and controllability in AC grids, and simpler implementation of multi-terminal DC grids. With further technological development, VSCs are expected to be employed even more in modern power systems. Therefore, this thesis focuses on VSC-based HVDC systems.

3. CONTROL OF VOLTAGE SOURCE CONVERTER BASED HVDC SYSTEMS

In this chapter, the necessary methodological background is provided. First, the SSSA is described together with all important terms and properties. Afterwards, state-space models of two-level and MMCs are derived step-by-step. Finally, two main HVDC grid control methods are presented: voltage margin and voltage droop control.

3.1. Small-signal stability analysis

A dynamic system is said to be stable in a small-signal sense or locally stable if it remains within a small region surrounding the equilibrium point when it is subjected to a small perturbation [12]. The conventional small-signal power system assessment is typically limited to dominant dynamic devices in the AC system, that is, synchronous generators and the corresponding low-frequency electromechanical oscillations. However, with a broader application of power electronic devices in power systems, a wider frequency bandwidth needs to be considered. The two most commonly used methods for small-signal stability assessment in the frequency domain are impedance-based and eigenvalue-based (modal) analysis. The former evaluates the stability of a part of the system, while the latter provides an assessment of the entire system [32]. Eigenvalue or modal analysis, which is used in this thesis, will be described in more detail.

3.1.1. Linearization

A power system dynamic model can be expressed by its state-space representation, that is, by a set of first-order nonlinear ordinary differential equations:

$$\dot{\mathbf{x}} = \mathbf{f}(\mathbf{x},\mathbf{u}), \tag{3.1}$$

with $\mathbf{x} \in \mathbb{R}^n$ being the state-space vector and $\mathbf{u} \in \mathbb{R}^m$ the system input vector. Adjacent to these differential equations, output variables are expressed by a set of algebraic equations:

$$\mathbf{y} = \mathbf{g}(\mathbf{x},\mathbf{u}), \tag{3.2}$$

where $\mathbf{y} \in \mathbb{R}^p$ is the system output vector. A prerequisite for the employment of modal analysis is a linearization of a power system model around an equilibrium point.

Such an equilibrium point $(\mathbf{x}_0,\mathbf{u}_0)$ satisfies the following condition:

$$\mathbf{f}(\mathbf{x}_0,\mathbf{u}_0) = 0. \tag{3.3}$$

The system described by (3.1) and (3.2) is linearized around an equilibrium point by assuming a small perturbation $\mathbf{x} = \mathbf{x_0} + \mathbf{\Delta x}$ and $\mathbf{u} = \mathbf{u_0} + \mathbf{\Delta u}$:

$$\begin{aligned} \dot{\mathbf{x}}_0 + \mathbf{\Delta}\dot{\mathbf{x}} &= \mathbf{f}(\mathbf{x}_0 + \mathbf{\Delta x}, \mathbf{u}_0 + \mathbf{\Delta u}) \\ \dot{\mathbf{y}}_0 + \mathbf{\Delta}\dot{\mathbf{y}} &= \mathbf{g}(\mathbf{x}_0 + \mathbf{\Delta x}, \mathbf{u}_0 + \mathbf{\Delta u}). \end{aligned} \tag{3.4}$$

Considering only the first order of the Taylor series expansion, a linearized form is obtained:

$$\begin{aligned} \mathbf{\Delta}\dot{\mathbf{x}} &= \mathbf{A} \cdot \mathbf{\Delta x} + \mathbf{B} \cdot \mathbf{\Delta u} \\ \mathbf{\Delta y} &= \mathbf{C} \cdot \mathbf{\Delta x} + \mathbf{D} \cdot \mathbf{\Delta u}, \end{aligned} \tag{3.5}$$

where matrices $\mathbf{A}$, $\mathbf{B}$, $\mathbf{C}$, and $\mathbf{D}$ are the Jacobian matrices, that is, matrices of the first partial derivatives evaluated at an equilibrium point:

$$\begin{aligned} \mathbf{A} &= \begin{bmatrix} \frac{\partial f_1}{\partial x_1} & \cdots & \frac{\partial f_n}{\partial x_1} \\ \vdots & \ddots & \vdots \\ \frac{\partial f_1}{\partial x_n} & \cdots & \frac{\partial f_n}{\partial x_n} \end{bmatrix} \quad \mathbf{B} = \begin{bmatrix} \frac{\partial f_1}{\partial u_1} & \cdots & \frac{\partial f_n}{\partial u_1} \\ \vdots & \ddots & \vdots \\ \frac{\partial f_1}{\partial u_n} & \cdots & \frac{\partial f_n}{\partial u_n} \end{bmatrix} \\ \mathbf{C} &= \begin{bmatrix} \frac{\partial g_1}{\partial x_1} & \cdots & \frac{\partial g_n}{\partial x_1} \\ \vdots & \ddots & \vdots \\ \frac{\partial g_1}{\partial x_n} & \cdots & \frac{\partial g_n}{\partial x_n} \end{bmatrix} \quad \mathbf{D} = \begin{bmatrix} \frac{\partial g_1}{\partial u_1} & \cdots & \frac{\partial g_n}{\partial u_1} \\ \vdots & \ddots & \vdots \\ \frac{\partial g_1}{\partial u_n} & \cdots & \frac{\partial g_n}{\partial u_n} \end{bmatrix} \end{aligned} \tag{3.6}$$

3.1.2. Modal analysis

According to Lyapunov's first method [12], small-signal stability is examined by considering the solutions of the characteristic equation:

$$\det(\mathbf{A} - \lambda \cdot \mathbf{I}) = 0, \tag{3.7}$$

in which the n solutions $\lambda_1, \lambda_2, \ldots, \lambda_n$ are called the eigenvalues of the state-space matrix $\mathbf{A}$. To ensure that a system is stable, the following condition needs to be met:

$$\mathrm{Re}(\lambda_i) < 0 \quad \forall i \ . \tag{3.8}$$

The free-motion response of the dynamic system, that is, with zero input, is determined by a linear combination of dynamic modes which correspond to the eigenvalues of the state-space matrix. The time-domain response of mode λ_i is given by $e^{\lambda_i t}$. Hence, if λ_i is real, the mode behavior is non-oscillatory, that is, decaying for negative, and aperiodically increasing for positive

eigenvalues. If λ_i is complex (for real matrices, complex eigenvalues always appear as complex conjugate pairs), the mode behavior is oscillatory. Again, for a negative real part, oscillations are damped, while for a positive real part, oscillations have increasing amplitude. An oscillatory mode $\lambda = \sigma \pm j\omega$ is characterized by the frequency of oscillation:

$$f = \frac{\omega}{2\pi}, \tag{3.9}$$

and by the damping ratio defined as follows:

$$\zeta = \frac{-\sigma}{\sqrt{\sigma^2 + \omega^2}}. \tag{3.10}$$

The damping ratio provides information on the rate of decay of the amplitude of the corresponding mode.

A vector $\mathbf{\Phi}_i$ for which the following expression holds:

$$\mathbf{A} \cdot \mathbf{\Phi}_i = \lambda_i \cdot \mathbf{\Phi}_i \tag{3.11}$$

is called the right eigenvector, and it measures the activity of system state variables when a certain mode is excited. Similarly, a vector $\mathbf{\Psi}_i$ with the following property:

$$\mathbf{\Psi}_i \cdot \mathbf{A} = \mathbf{\Psi}_i \cdot \lambda_i \tag{3.12}$$

is called the left eigenvector, and it identifies a combination of state variables observed in a certain mode. Further details and mathematical derivations can be found in [12, 33].

Since eigenvectors are related to the physical units and scaling of associating state variables, it is not straightforward to use them for establishing a connection between state variables and system modes. Therefore, a dimensionless quantity called the participation factor is introduced. The relative participation of state variable x_k in mode λ_i is given by

$$p_{ki} = \Phi_{ki} \cdot \Psi_{ik}, \tag{3.13}$$

where Φ_{ki} is the *k*-th entry of the right eigenvector $\mathbf{\Phi}_i$, and Ψ_{ik} is the *k*-th entry of the left eigenvector $\mathbf{\Psi}_i$. Participation factors in this thesis are normalized such that the sum of the magnitudes of participation factors corresponding to one mode is equal to 1. Furthermore, a definition of the subsystem participation $p_{\alpha,i}$ in a certain mode λ_i has been adjusted from [34]:

$$p_{\alpha,i} = \sum p_{ki} \quad | \, x_k \in \alpha \, . \tag{3.14}$$

where α is the set of state variables describing a particular subsystem.

3.2. Modeling and control of voltage source converters

One difference between detailed and time-averaged converter models needs to be elaborated. On the one hand, detailed converter models, which include semiconductor components, are employed in electromagnetic transient simulation tools with the following research objectives: analysis of various converter topologies, various modulation techniques, converter losses, and others. On the other hand, time-averaged models are used in electromechanical stability programs to study converter control response in larger systems (although they can also be used in electromagnetic transient programs). By doing so, switching dynamics and high-frequency phenomena are neglected. Since research in this thesis is directed toward studying VSC HVDC control response in AC and DC grids, time-averaged models are used.

The behavior of VSCs toward an AC grid can be compared with that of synchronous machines. VSCs can regulate the amplitude and the phase angle of their synthesized alternating voltage. A PWM technique is often used to switch converter valves as discussed in Chapter 2. An equivalent scheme and a vector diagram of a VSC connected to an AC grid through an inductive line are shown in Fig. 3.1. The AC grid voltage is denoted with v_o, and V_o is its RMS value; e is the synthesized converter voltage, and E its RMS value; i_{cv} is the converter AC side current, X is the line reactance, and δ is the phase angle between a converter and an AC grid voltage. The equations describing active and reactive power flow are:

$$P_{ac} = \frac{V_o \cdot E}{X} \sin(\delta) \, , \tag{3.15}$$

$$Q_{ac} = \frac{V_o^2}{X} - \frac{E \cdot V_o}{X} \cos(\delta) \, . \tag{3.16}$$

The active power flow mostly depends on the phase angle between the converter and the AC grid (for small angles) while the reactive power flow mostly depends on the amplitude of the converter voltage. Since a VSC can regulate the amplitude and phase angle of a synthesized AC voltage, active and reactive power regulation is enabled. However, the regulation of active and reactive power is not completely independent by using this control approach, and more importantly,

converter currents cannot be limited. A limitation of currents is especially important because of the low overcurrent capabilities of converters.

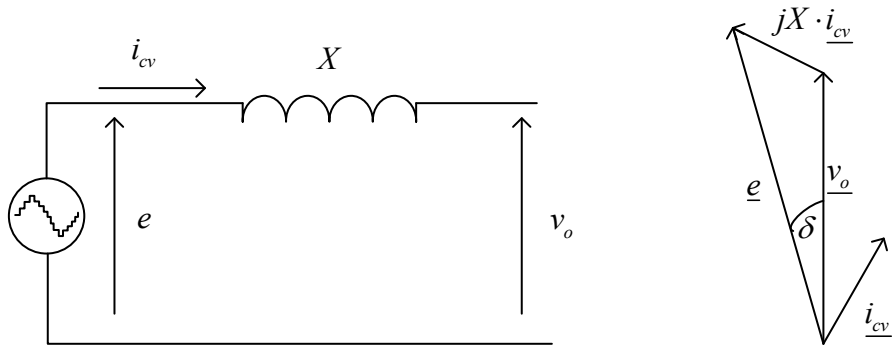

Figure 3.1: Equivalent scheme and vector diagram of a VSC connected to an AC grid

A standard control method used in VSCs is vector control. By using this method, converter currents are regulated directly in a synchronously rotating dq-reference frame. First, the Clarke transformation is used for the coordinate transformation of physical abc quantities into the αβ-frame, a stationary orthogonal reference frame in which alternating quantities are presented as vectors. This way, in the case of a balanced AC system, three-phase quantities become two-phase quantities. Fig. 3.2 shows converter and grid voltages and converter current as vectors which rotate with a synchronous speed in a steady state. Second, the Park transformation is used for the coordinate transformation into a synchronously rotating dq-reference frame. This way, vectors become standstill, that is, they have a constant value in a steady state, which is very useful from a control perspective. Furthermore, to reduce the complexity of some derivations, coordinate transformations between different dq-reference frames are employed, such as for grid studies. In large AC systems, the AC grid is modeled in a global DQ-reference frame and generators and converters in their local dq-reference frames.

Expressions for the active and reactive power in a dq-reference system are the following:

$$P_{ac} = v_{o,d} \cdot i_{cv,d} + v_{o,q} \cdot i_{cv,q}\,, \tag{3.17}$$

$$Q_{ac} = v_{o,q} \cdot i_{cv,d} - v_{o,d} \cdot i_{cv,q}\,. \tag{3.18}$$

By using a controller circuit called phase-locked loop (PLL), the grid voltage vector $\underline{v_o}$ is aligned with the reference frame, for instance, with the d-axis (the q-component of a grid voltage is equal

to 0 in this case). This can be observed in Fig. 3.2. Expressions for the active and reactive power (assuming perfect PLL) are then simplified to:

$$P_{ac} = v_{o,d} \cdot i_{cv,d} \,, \tag{3.19}$$

$$Q_{ac} = -v_{o,d} \cdot i_{cv,q} \,. \tag{3.20}$$

From equations (3.19) and (3.20), it can be observed that the active power depends only on the d-component of a converter current, and reactive power depends only on the q-component of the current. Thus, independent regulation of active and reactive power is enabled. Furthermore, it is now possible to limit converter currents. However, it needs to be emphasized that the choice of orientation of the reference frame is somewhat arbitrary and that the grid voltage can also be aligned with the q-axis of a reference frame. In this case, the active power would depend on the q-component and reactive power on the d-component of the converter current.

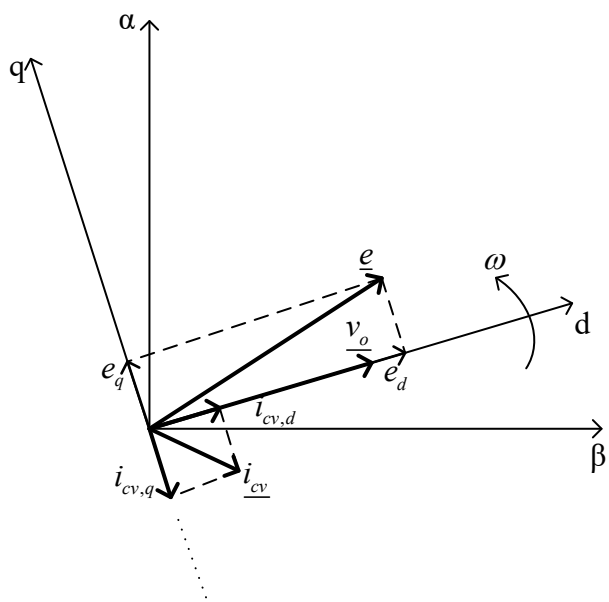

Figure 3.2: αβ- and dq-reference frames

Issues with the vector control typically occur when the converter is connected to a very weak AC system primarily because of the PLL dynamics. To overcome difficulties, a control method called power synchronization control has been developed [26]. This method mimics the behavior of a synchronous machine and omits the use of a PLL.

3.2.1. Two-level voltage source converters

A time-averaged model of a two-level VSC, shown in Fig. 3.3, consists of a controlled three-phase voltage source on the AC side and a controlled current source on the DC side. Controlled voltage sources are connected in series with a phase reactor and transformer which are represented by the corresponding inductance L_f and resistance R_f. A controlled current source is connected in parallel with the capacitor C_{dc}.

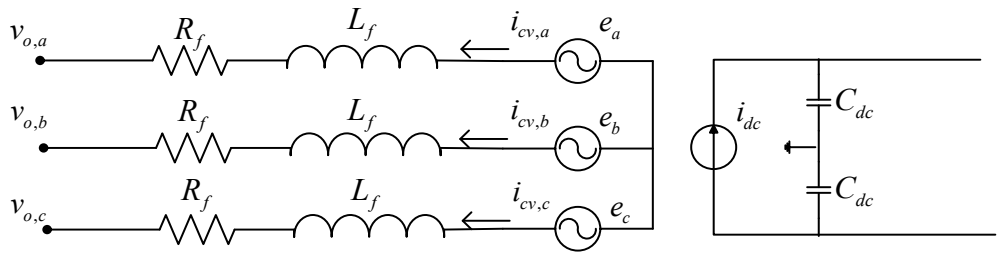

Figure 3.3: Time-averaged model of a two-level VSC

The VSC dynamic model, described in the continuation, is largely based on the representation specified in [35]. The modeling of the physical system and the control implementation is based on per unit quantities denoted by lower case letters. The variables in the dq-reference frame are written as $\underline{x} = x_d + j \cdot x_q$. The physical system, designated in Fig. 3.4 in blue, consists of the AC side circuit, the DC side circuit, and the converter itself. The AC side circuit includes a regulating transformer and a phase reactor, which is necessary for the independent control of active and reactive powers by using the vector control. The dynamics of converter AC currents are expressed in the following equation:

$$\frac{di_{cv,i}}{dt} = \frac{\omega_b}{L_f} e_i - \frac{\omega_b}{L_f} v_{o,i} - \frac{R_f \cdot \omega_b}{L_f} i_{cv,i} \quad i = a,b,c\,, \tag{3.21}$$

where ω_b is the base angular grid frequency. Transforming (3.21) into a dq-reference frame results in the following expression:

$$\frac{d\underline{i_{cv}}}{dt} = \frac{\omega_b}{L_f} \underline{e} - \frac{\omega_b}{L_f} \underline{v_o} - \left(\frac{R_f \cdot \omega_b}{L_f} + j \cdot \omega_g \cdot \omega_b \right) \cdot \underline{i_{cv}}\,, \tag{3.22}$$

where $\underline{i_{cv}} = i_{cv,d} + j \cdot i_{cv,q}$ is the converter current expressed in a dq-reference frame, and ω_g is the per-unit grid frequency. Similarly, the dynamics of the PCC voltage can be calculated as:

$$\frac{d\underline{v_o}}{dt} = \frac{\omega_b}{C_f}\underline{i_{cv}} - \frac{\omega_b}{C_f}\underline{i_o} + j \cdot \omega_g \cdot \omega_b \cdot \underline{v_o}\,, \tag{3.23}$$

with C_f being the filter capacitance and $\underline{i_o} = i_{o,d} + j \cdot i_{o,q}$ the external AC grid current. The voltage on the DC side is expressed as

$$\frac{dv_{dc}}{dt} = \frac{\omega_b}{C_{dc}} i_{dc} - \frac{\omega_b}{C_{dc}} i_{cable}\,, \tag{3.24}$$

with C_{dc} including capacitances of the converter and of the connecting lines and i_{cable} representing the sum of cable/line currents. Assuming a lossless average model, the power balance between the AC side and the DC side is described by the law of power conservation:

$$e_d \cdot i_{cv,d} + e_q \cdot i_{cv,q} = m \cdot v_{dc} \cdot i_{dc}\,, \tag{3.25}$$

where m is the number of transmission poles: $m = 1$ for a monopolar configuration and $m = 2$ for a bipolar configuration.

The control system has a hierarchical control structure designated in Fig. 3.4 in green. It consists of the inner current control (ICC), the outer control, and the PLL which is used for synchronization with an AC grid. In each control circuit, a conventional proportional-integral (PI) regulator is used. Regulator limits are not included since they are not necessary in SSSA.

Inner current control

The ICC circuit, in which the reference values of the AC side driving voltages $\underline{e^*} = e_d^* + j \cdot e_q^*$ are set, is described with the following equations:

$$\begin{aligned} \underline{e^*} &= k_{p,ICC}\left(\underline{i_{cv}^*} - \underline{i_{cv}}\right) + k_{i,ICC} \cdot \underline{\gamma} + j \cdot L_f \cdot \omega_{PLL} \cdot \underline{i_{cv}} + k_{ffv} \cdot \underline{v_o} \\ \frac{d\underline{\gamma}}{dt} &= \underline{i_{cv}^*} - \underline{i_{cv}}\,, \end{aligned} \tag{3.26}$$

where $\underline{i_{cv}^*} = i_{cv,d}^* + j \cdot i_{cv,q}^*$ is the reference value of converter currents; $k_{p,ICC}$ and $k_{i,ICC}$ are the proportional and integral coefficients of the PI regulator, respectively; $\underline{\gamma} = \gamma_d + j \cdot \gamma_d$ is its integrator state; ω_{PLL} is the per-unit grid frequency estimated by the PLL; and k_{ffv} is a binary constant for the feedforwarding of the PCC voltage. A feedforwarding of the PCC voltage is used to improve the dynamic performance of the ICC [26]. A current decoupling feedforward term

$j \cdot L_f \cdot \omega_{PLL} \cdot \underline{i_{cv}}$ is introduced in to control the d- and the q-current independently. The obtained reference values of the AC side driving voltages $\underline{e}^* = e_d^* + j \cdot e_q^*$ are further used in the PWM modulator. However, this control level is not further specified in time-averaged models.

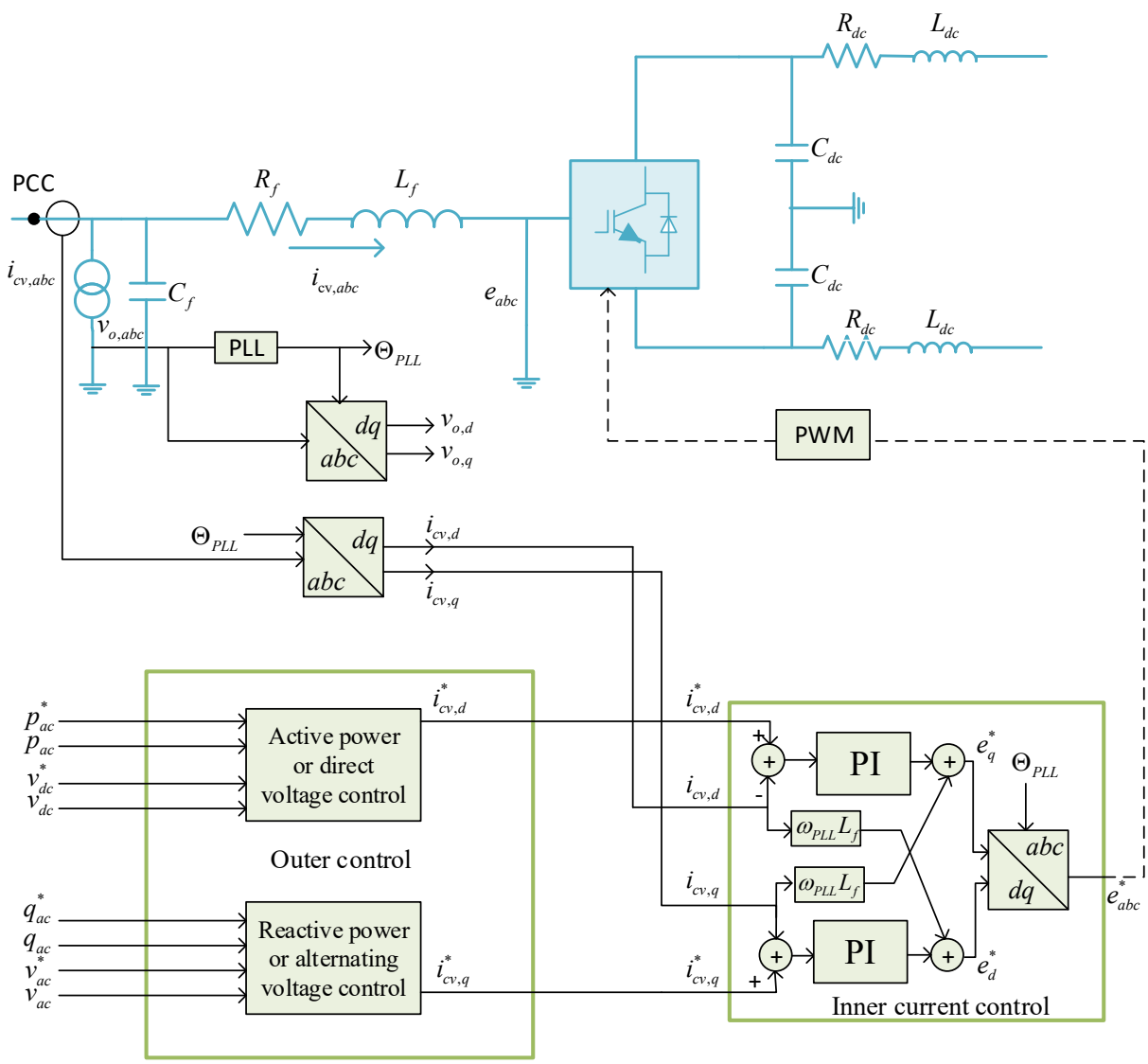

Figure 3.4: Overview of the VSC physical and control system

Outer loop control

Since the grid voltage is aligned with the d-axis of a reference frame, the d-component of converter current is related to the active power regulation as described by (3.19). The reference value of the d-component of converter current $i_{cv,d}^*$ is set in the outer controller by either the active

power controller (equation (3.27)) or the DC voltage controller (equation (3.28)). In these equations, the reference value of converter active power is denoted by p_{ac}^{*}, the actual value of active power by p_{ac}, the reference value of the DC voltage by v_{dc}^{*}; $k_{p,P}$ and $k_{i,P}$ are the proportional and integral coefficients, respectively; and ρ_d is the integrator state of the corresponding regulator. In a point-to-point HVDC line, a rectifier regulates the active power, and an inverter regulates the DC voltage of the line. Moreover, a combination of the active power and the DC voltage regulation is possible by applying a droop control described by (3.29). In this equation, the reference active power p_{ac}^{*}, which is an input to the outer loop PI controller, is influenced by a DC voltage droop coefficient k_{drp} while p_{ac}^{ref} is the external active power reference.

$$\begin{aligned} i_{cv,d}^{*} &= k_{p.P}\left(p_{ac}^{*} - p_{ac}\right) + k_{i,P}\rho_d \\ \frac{d\rho_d}{dt} &= p_{ac}^{*} - p_{ac} \end{aligned} \tag{3.27}$$

$$\begin{aligned} i_{cv,d}^{*} &= k_{p,P}\left(v_{dc}^{*} - v_{dc}\right) + k_{i,P}\rho_d \\ \frac{d\rho_d}{dt} &= v_{dc}^{*} - v_{dc} \end{aligned} \tag{3.28}$$

$$p_{ac}^{*} = k_{drp}(v_{dc}^{*} - v_{dc}) + p_{ac}^{ref} \tag{3.29}$$

Similarly, the q-component of the converter current is related to the reactive power regulation (equation (3.20). The reference value of the q-component of the converter current $i_{cv,q}^{*}$ is set in the outer controller by either the reactive power controller (equation (3.30)) or the AC voltage controller (equation (3.31)). The reference value of converter reactive power is denoted by q_{ac}^{*}, the actual value of reactive power by q_{ac}, the reference value of the AC voltage by v_{ac}^{*}; $k_{p,Q}$ and $k_{i,Q}$ are the proportional and integral coefficients; and ρ_q is the integrator state of the corresponding controller. The actual value of the AC voltage is determined by using relation (3.32). Again, a combination of the reactive power and the AC voltage regulation is possible by applying a droop control described by (3.33). The reference reactive power q_{ac}^{*}, which is an input to the outer-loop PI controller, is influenced by an AC voltage droop coefficient k_{drp} while q_{ac}^{ref} is the external reactive power reference.

$$i_{cv,q}^{*} = k_{p,Q}\left(q_{ac}^{*} - q_{ac}\right) + k_{i,Q}\rho_q$$
$$\frac{d\rho_q}{dt} = q_{ac}^{*} - q_{ac} \tag{3.30}$$

$$i_{cv,q}^{*} = k_{p,Q}\left(v_{ac}^{*} - v_{ac}\right) + k_{i,Q}\rho_q$$
$$\frac{d\rho_q}{dt} = v_{ac}^{*} - v_{ac} \tag{3.31}$$

$$v_{ac} = \sqrt{v_{o,d}^2 + v_{o,q}^2} \tag{3.32}$$

$$q_{ac}^{*} = k_{drp}(v_{ac}^{*} - v_{ac}) + q_{ac}^{ref} \tag{3.33}$$

Phase-locked loop

The PLL modeling is based on [26]. By using the PCC voltage, the signal $\Delta\varphi$ is created according to (3.34) and then fed into the PI controller described by (3.35). The controller's output is the frequency deviation $\Delta\omega_{PLL}$, with $k_{p,PLL}$ and $k_{i,PLL}$ being the proportional and integral coefficients, respectively, and ε_{PLL} the corresponding integrator state. In [26]. it is shown that in a linearized model, $\Delta\varphi$ is in fact a phase tracking error. Thus, the PLL can be assumed to accurately track the phase angle of the PCC voltage.

$$\Delta\varphi = \frac{v_{o,q}}{\sqrt{v_{o,d}^2 + v_{o,q}^2}} \tag{3.34}$$

$$\Delta\omega_{PLL} = k_{p,PLL} \cdot \Delta\varphi + k_{i,PLL} \cdot \varepsilon_{\mathrm{PLL}}$$
$$\frac{d\varepsilon_{\mathrm{PLL}}}{dt} = \Delta\varphi \tag{3.35}$$

The frequency deviation is integrated to create the angle deviation $\Delta\Theta_{PLL}$ signal:

$$\Delta\Theta_{PLL} = \int \Delta\omega_{PLL}\, dt \cdot \omega_b\,. \tag{3.36}$$

These two state variables (ε_{PLL} and $\Delta\Theta_{PLL}$) are sufficient for representing the PLL in a synchronously rotating frame (SRF). However, for dq-transformations indicated in Fig. 3.4, it is necessary to obtain the instantaneous grid angle Θ_{PLL}. First, the nominal grid frequency ω_g is added to the frequency deviation to obtain the instantaneous grid frequency estimated by the PLL

ω_{PLL} (equation (3.37)). Then, the instantaneous grid frequency is integrated to obtain the instantaneous grid angle Θ_{PLL} (equation (3.38)).

$$\omega_{PLL} = \Delta\omega_{PLL} + \omega_g \tag{3.37}$$

$$\Theta_{PLL} = \int \omega_{PLL}\, dt \cdot \omega_b \tag{3.38}$$

The state-space vector of the converter, described with the previous equations, thus contains 11 variables altogether:

$$\mathbf{x_{conv}} = \left[i_{cv,d}\ i_{cv,q}\ v_{o,d}\ v_{o,q}\ v_{dc}\ \gamma_d\ \gamma_q\ \rho_d\ \rho_q\ \varepsilon_{PLL}\ \Delta\Theta_{PLL} \right]. \tag{3.39}$$

A slightly different control approach is adopted in [36]. The only difference is that the DC voltage controller consists of a single control loop. Therefore, the state-space model of a converter has one fewer variable (usually an inverter operation in a point-to-point line):

$$\mathbf{x_{inv}} = \left[i_{cv,d}\ i_{cv,q}\ v_{o,d}\ v_{o,q}\ v_{dc}\ \gamma_q\ \rho_d\ \rho_q\ \varepsilon_{PLL}\ \Delta\Theta_{PLL} \right]. \tag{3.40}$$

A more detailed converter model can be obtained by including filtering and measurement dynamics. Low-pass filters of the following variables, employed in the outer control, are normally used: AC voltage (3.41), DC voltage (3.42), active power (3.43), and reactive power (3.44). The corresponding cut-off frequencies are denoted by $\omega_{ac,f}$, $\omega_{dc,f}$, $\omega_{p,ac}$ and $\omega_{q,ac}$. Furthermore, the PCC voltage is filtered for the application in the ICC and the PLL. In doing so, two different cut-off frequencies are used: $\omega_{ICC,f}$ for the ICC (3.45) and $\omega_{PLL,f}$ for the PLL (3.46).

$$\frac{dv_{ac,f}}{dt} = \omega_{ac,f}\left(v_{ac} - v_{ac,f}\right) \tag{3.41}$$

$$\frac{dv_{dc,f}}{dt} = \omega_{dc,f}\left(v_{dc} - v_{dc,f}\right) \tag{3.42}$$

$$\frac{dp_{ac,f}}{dt} = \omega_{p,ac}\left(p_{ac} - p_{ac,f}\right) \tag{3.43}$$

$$\frac{dq_{ac,f}}{dt} = \omega_{q,ac}\left(q_{ac} - q_{ac,f}\right) \tag{3.44}$$

$$\frac{d\underline{v_{ICC}}}{dt} = \omega_{ICC,f}\left(\underline{v_o} - \underline{v_{ICC}}\right) \tag{3.45}$$

$$\frac{d\underline{v_{PLL}}}{dt} = \omega_{PLL,f}\left(\underline{v_o} - \underline{v_{PLL}}\right) \tag{3.46}$$

By including the described filtering dynamics, the converter state-space model grows with 6 additional variables and has 17 variables in total:

$$\mathbf{x_{conv}} = \begin{bmatrix} i_{cv,d}\ i_{cv,q}\ v_{o,d}\ v_{o,q}\ v_{dc}\ \gamma_d\ \gamma_q\ \rho_d\ \rho_q\ \varepsilon_{PLL}\ \Delta\Theta_{PLL} \\ p_{ac,f}\ (v_{dc,f})\ q_{ac,f}\ (v_{ac,f})\ v_{ICC,d}\ v_{ICC,q}\ v_{PLL,d}\ v_{PLL,q} \end{bmatrix}. \tag{3.47}$$

The filtered DC voltage $v_{dc,f}$ in (3.47) appears in brackets since it is assumed that a converter regulates either the active power or the DC voltage. In case a droop control is applied, the number of state variables grows by one more since both the filtering of the active power and that of the DC voltage are employed. The same applies to the reactive power and the AC voltage control or a combination thereof.

3.2.2. Modular multilevel converters

MMCs, in comparison to the two-level topology, include additional dynamics related to internal capacitive energy storage and circulating currents which flow through the submodules of each converter leg. Namely, MMCs do not rely on a large capacitance on the DC side but have distributed capacitances throughout the converter submodules. The AC output voltage is synthesized by subtracting the voltages of the upper and lower converter arms, and the DC voltage is obtained by adding them. With a large number of submodules in each converter arm, voltages on the AC and DC side can be regulated with high precision. In this way, an MMC does not appear only as a voltage source from the AC side, but also as a voltage source from the DC side. Fig. 3.5 depicts a time-averaged model of an MMC. The equivalent circuit on the AC side used to design the controls, besides a filter, also includes half of both the arm inductance L_a and of the arm resistance R_a. An arm reactor is included in each converter arm to avoid high-frequency components in the circulating currents, to enable a smooth control of the circulating currents and in some cases, to limit fault currents. It should be emphasized that the filter inductance L_f for MMCs is primarily related to the leakage inductance and filter resistance R_f to the resistance of a transformer connecting the converter to an AC grid. Converter currents on the AC side are described using the similar expressions as with a two-level converter:

$$\frac{d\underline{i_{cv}}}{dt} = \frac{\omega_b}{L_f + \frac{L_a}{2}}\underline{e} - \frac{\omega_b}{L_f + \frac{L_a}{2}}\underline{v_o} - \left(\frac{\left(R_f + \frac{R_a}{2}\right)\cdot \omega_b}{L_f + \frac{L_a}{2}} + j \cdot \omega_g \cdot \omega_b \right) \cdot \underline{i_{cv}} \,. \tag{3.48}$$

The equivalent circuit on the DC side in Fig. 3.5 includes the circulating currents $i_{c,i}$ $(i = a,b,c)$ which are inherent to MMCs, voltages driving these circulating currents $v_{c,i}$ $(i = a,b,c)$, while the capacitance C_{dc} represents only the capacitances of the connecting lines/cables.

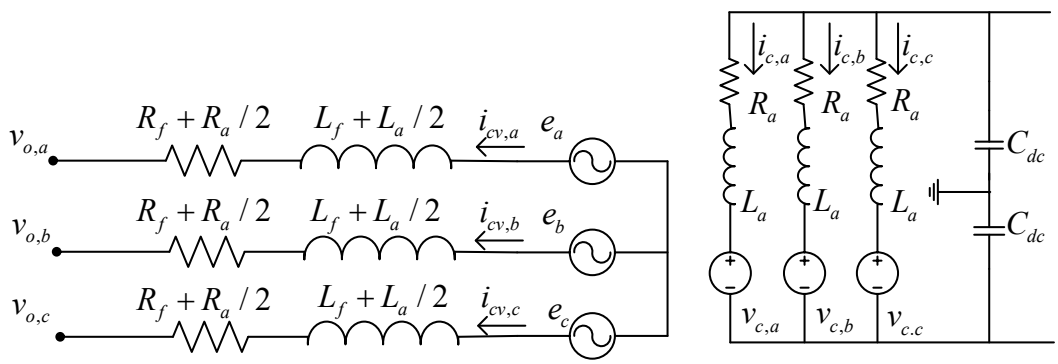

Figure 3.5: Time-averaged model of an MMC

An MMC behaves essentially like three single-phase converters which results in a double-frequency oscillation of the power between the phase legs. In addition, fundamental frequency oscillations appear between the upper and the lower arms. Thus, internal variables related to the MMC operation contain different low-frequency components. Using a Park transformation to one synchronously rotating reference frame (as with two-level converters) does not therefore put all variables into steady-state quantities, which is a necessity for SSSA. Different approaches have been developed to resolve this issue [37]. One solution is to use a harmonic superposition, in which each frequency component is transformed to its SRF. A more elegant solution is to apply an appropriate linear transformation to separate the variables with different frequencies and then apply corresponding transformations into different SRFs. More details about the operation and control of MMCs can be found in [26].

Since the work in this thesis focuses on converter control response in AC and DC grids, the state-space MMC model with simplified internal dynamics is adopted from [37] and [38]. It was shown that this simplified model is well-suited for power system–oriented studies because it

accurately represents the interface variables on the AC and the DC side of an MMC. It is an energy-based controlled MMC model with compensated modulation. The compensated modulation uses measured (or estimated) time-varying aggregated arm voltages in the calculation of insertion indices. This way, insertion indices include a continuous compensation for the oscillations in the converter arm voltages. Consequently, the converter voltages (the AC and the DC side driving voltages) are equal to their reference values. Moreover, the compensated modulation enables the derivation of the energy-based, steady-state, time-invariant representation of an MMC [37].

The MMC model with simplified internal dynamics includes only the zero-sequence components of the MMC internal variables which are inherently time-invariant in a steady state. The internal dynamics are expressed in the following equations:

$$\frac{dw_{\Sigma}}{dt} = \left[-(e_d \cdot i_{cv,d} + e_q \cdot i_{cv,q}) + 4v_{c,z} \cdot i_{c,z} \right] \frac{\omega_b}{8C_{eq}}, \tag{3.49}$$

$$\frac{di_{c,z}}{dt} = \frac{\omega_b}{L_a} v_{dc} - \frac{\omega_b}{L_a} v_{c,z} - \frac{R_a \cdot \omega_b}{L_a} i_{c,z}, \tag{3.50}$$

where w_{Σ} is the aggregated zero-sequence energy sum, $i_{c,z}$ is the zero-sequence of the circulating current, and C_{eq} is the equivalent per-arm capacitance of an MMC represented in the AC side per unit system. In [37], it has been shown that this simplified model can be derived from the full internal dynamics steady-state model by considering only the zero-sequence components of the internal variables and by neglecting the fundamental frequency dq-components of the DC driving voltage v_c (since they are significantly smaller than the zero-sequence component). The DC side circuit is expressed in (3.51) in which the zero-sequence of the circulating current is multiplied by four instead of three since it is represented in the AC side per unit system. More details can be found in [38].

$$\frac{dv_{dc}}{dt} = \frac{\omega_b}{C_{dc}} \left(i_{cable} - 4i_{c,z} \right) \tag{3.51}$$

In addition to the control system of a two-level converter, the control of MMC internal variables is highlighted in Fig. 3.6 in yellow. In the outer PI controller of the aggregated zero-sequence energy sum, the reference value of the circulating current $i_{c,z}^{*}$ is set, as described by equation (3.52). In the inner zero-sequence circulating current control, the reference of the zero-

sequence DC driving voltage $v_{c,z}^{*}$ is obtained, as described by equation (3.53). In these equations, $k_{p,w\Sigma}$ and $k_{i,w\Sigma}$ are the proportional and integral coefficients of the zero-sequence energy-sum controller and κ_{Σ} is the corresponding integrator state; $k_{p,cz}$ and $k_{i,cz}$ are the proportional and integral coefficients of the zero-sequence circulating current controller, respectively; and ζ_z is the corresponding integrator state. Reference values of the AC and the DC side driving voltages (e^{*} and $v_{c,z}^{*}$) are further employed in the calculation of the insertion indices, balancing, and modulation, as indicated in Fig. 3.6. However, as these controllers are not included in the time-averaged models, they are not described further.

$$\begin{aligned} i_{c,z}^{*} &= k_{p,w\Sigma}\left(w_{\Sigma}^{*} - w_{\Sigma}\right) + k_{i,w\Sigma}\kappa_{\Sigma} \\ \frac{d\kappa_{\Sigma}}{dt} &= w_{\Sigma}^{*} - w_{\Sigma} \end{aligned} \tag{3.52}$$

$$\begin{aligned} v_{c,z}^{*} &= -k_{p,cz}\left(i_{c,z}^{*} - i_{c,z}\right) - k_{i,cz}\zeta_z \\ \frac{d\zeta_z}{dt} &= i_{c,z}^{*} - i_{c,z} \end{aligned} \tag{3.53}$$

The state-space vector of an MMC has four additional variables (compared with a two-level model) describing internal dynamics and corresponding controllers. Thus, the state-space vector has 21 variables, including signal filtering variables:

$$\mathbf{x}_{\mathbf{conv}} = \begin{bmatrix} i_{cv,d}\ i_{cv,q}\ v_{o,d}\ v_{o,q}\ v_{dc}\ \gamma_d\ \gamma_q\ \rho_d\ \rho_q\ \varepsilon_{PLL}\ \Delta\Theta_{PLL} \\ p_{ac,f}\ (v_{dc,f})\ q_{ac,f}\ (v_{ac,f})\ v_{ICC,d}\ v_{ICC,q}\ v_{PLL,d}\ v_{PLL,q} \\ w_{\Sigma}\ i_{c,z}\ \kappa_{\Sigma}\ \zeta_z \end{bmatrix}. \tag{3.54}$$

3.3. Control of HVDC grids

The voltage in a DC grid has a similar role as the frequency in an AC grid. Any power mismatch in a DC grid is reflected in the change in DC voltage. However, there are two main differences in comparison to the frequency in an AC grid. First, unlike frequency, which is a global variable consistent throughout the entire AC system, DC voltage has different values in various nodes and depends significantly on the power flow in the grid. Second, time constants in a DC grid, related to charging/discharging converter and line capacitances, are much smaller in comparison to inertial time constants in an AC grid. Because of these, DC grid control is a cumbersome and

challenging task. Two basic control methods, described in the following sections, are voltage margin control and voltage droop control.

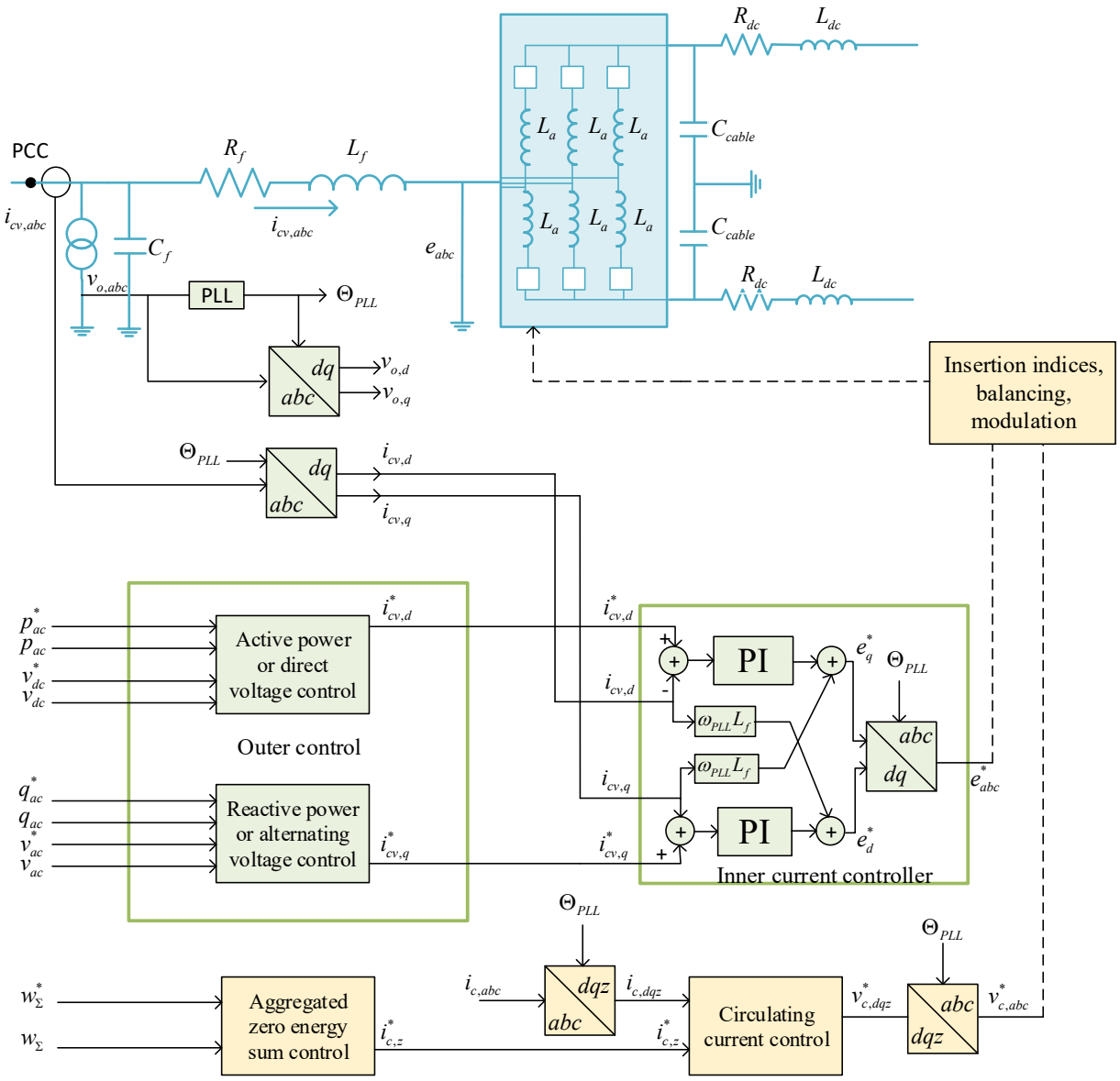

Figure 3.6: Overview of an MMC physical and control system

3.3.1. Voltage margin control

Voltage margin control is a centralized method similar to the control of a point-to-point DC line. One converter controls the grid voltage to a given reference, and the others control their active power injections. Fig. 3.7a shows the qualitative operating characteristic of the power controlling converter, and Fig. 3.7b shows that of the voltage controlling converter. Voltage and power limits are also indicated in the figures. The converter's upper voltage limit depends on the insulation of

switching components and other equipment while the lower voltage limit mostly depends on modulation restrictions. A converter only has an upper power limit that mostly depends on the semiconductor current limit, which is not explicitly indicated in the figures. The following sign convention is adopted: if power is flowing out of a DC grid (inverter operation), it has a positive sign, and if it is flowing into a DC grid (rectifier operation), it has a negative sign. A converter can maintain a constant active power injection as long as it is within its voltage limits, as can be observed from Fig. 3.7a. Also, a converter can maintain a constant DC voltage as long as it is within converter power limits. However, when the power limit is reached, a converter operates at the constant power characteristic. As described in Section 3.2.1, PI controllers in the outer control loops are used to regulate a constant active power or a constant DC voltage.

The operating principles of voltage margin control are illustrated in Fig. 3.8 in the case of a small DC grid with four terminals connecting three asynchronous AC grids. At each converter terminal, a simple active power–time characteristic is depicted with active power expressed in the absolute value for simplicity reasons. Converters 1 and 2 operate as rectifiers, injecting active power into the DC grid, and converters 3 and 4 operate as inverters, extracting the active power from the DC grid (as indicated by the arrows in Fig. 3.8). Converter 1 operates in the constant DC voltage mode while the other converters operate in the constant active power mode. In case of an outage in converter 2, converter and line/cable capacitances start to discharge because of power mismatch, and the voltages in the grid start to decrease. Voltage controlling converter 1 responds by injecting more active power into the grid while the powers of other two converters remain unaltered. However, in the case where the power limit in converter 1 is reached before the power equilibrium point is established (or in the case of an outage in converter 1), a backup is needed. This is achieved by setting different voltage margins at several converters. Voltage margin control is a satisfactory control for DC grids with a small number of terminals but is not suitable for large ones. Different power flow possibilities in large DC grids complicate the setting of appropriate voltage margins at different converters. If the voltage margins are set too closely, there is a possibility of detrimental oscillatory behavior in the system caused by the two converters controlling the voltage simultaneously.

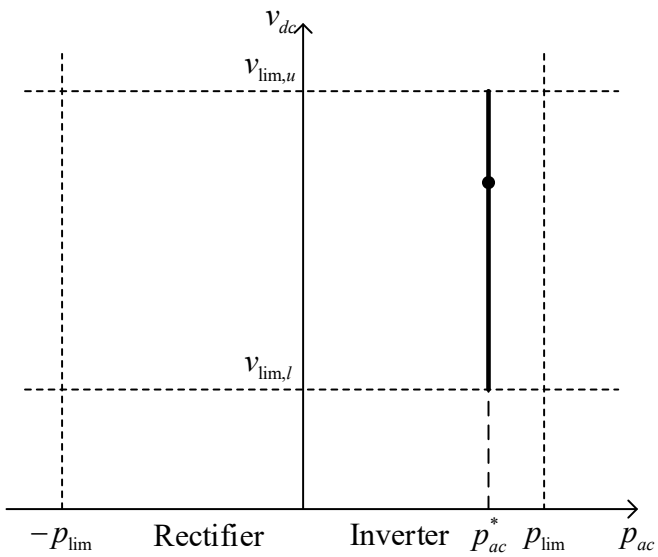

a)

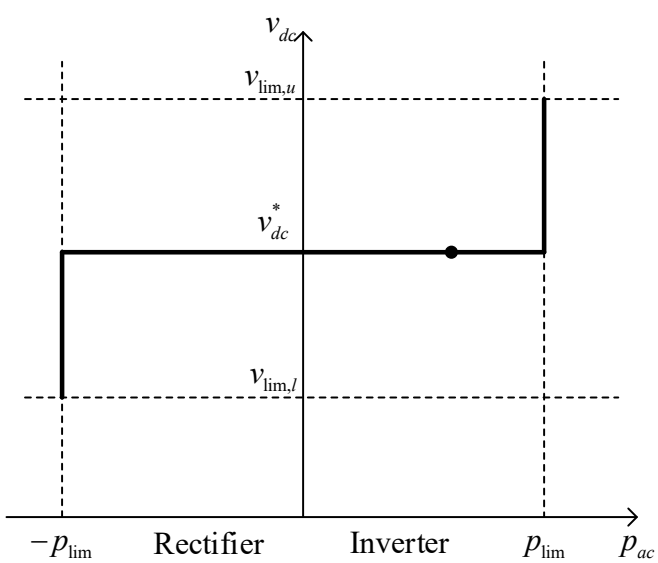

b)

Figure 3.7: Operating characteristic of a: a) power controlling converter; b) voltage controlling converter

3.3.2. Voltage droop control

Voltage droop control is a distributed control method in which two or more converters simultaneously participate in voltage control. An operating characteristic of the converter with droop control is shown in Fig. 3.9. Considering the adopted sign convention, the characteristic has a positive slope described in the following expression:

$$p_{ac} - p_{ac}^{*} = k_{drp}\left(v_{dc} - v_{dc}^{*}\right), \tag{3.55}$$

with k_{drp} being the inverse slope of the characteristic. A proportional controller is used for the control implementation with a proportional coefficient equal to $k_p = k_{drp}$. When the voltage in the DC grid rises, inverters increase their power extraction from the grid while rectifiers decrease their power injection into the grid. Similarly, when the voltage in a DC grid falls, inverters decrease their power extraction from the grid while rectifiers increase their power injection into the grid. Also, converters with higher values of droop coefficients participate to a larger extent in DC voltage regulation while converters with lower values of droop coefficients participate to a smaller extent in DC voltage regulation.

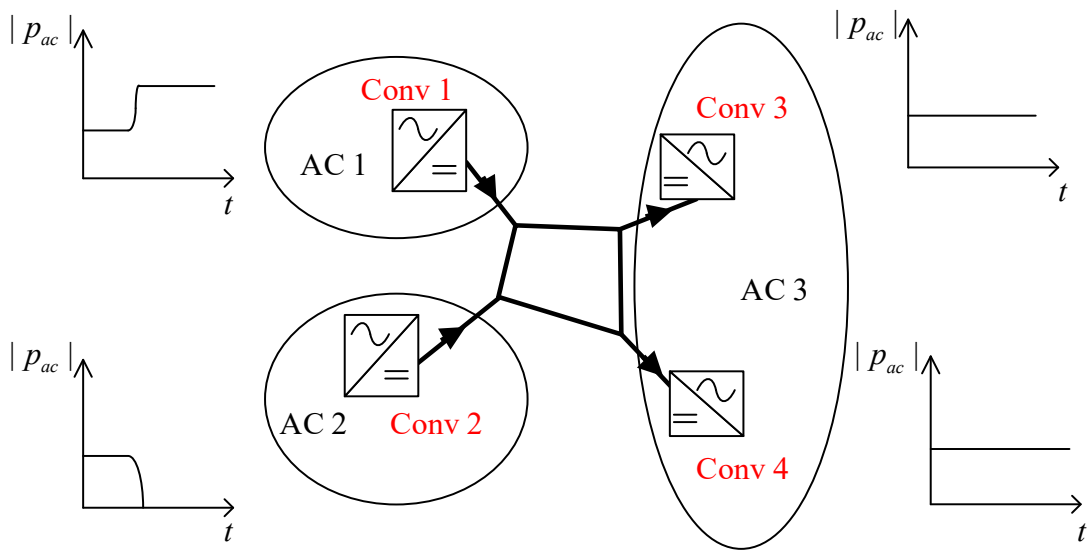

Figure 3.8: DC grid voltage margin control

The operating principles of voltage droop control are illustrated in Fig. 3.10 for the same grid as with the voltage margin control. In the case of an outage in converter 2, all droop-equipped converters participate in DC voltage regulation by adjusting their active power references. Rectifying converter 1 increases its active power injection into the grid while inverting converters 3 and 4 decrease their powers extracted from the grid. Different from the voltage margin control, the operating conditions of all converters are altered. Therefore, secondary voltage control is needed to restore the per-fault operating condition.

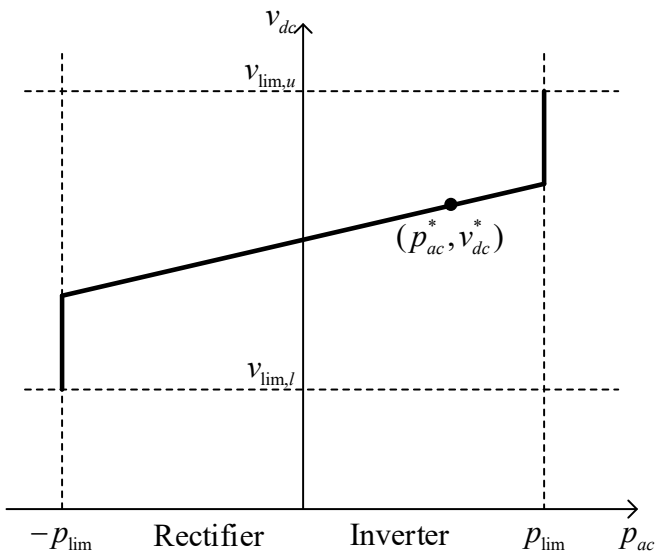

Figure 3.9: Operating characteristic of a converter with droop control

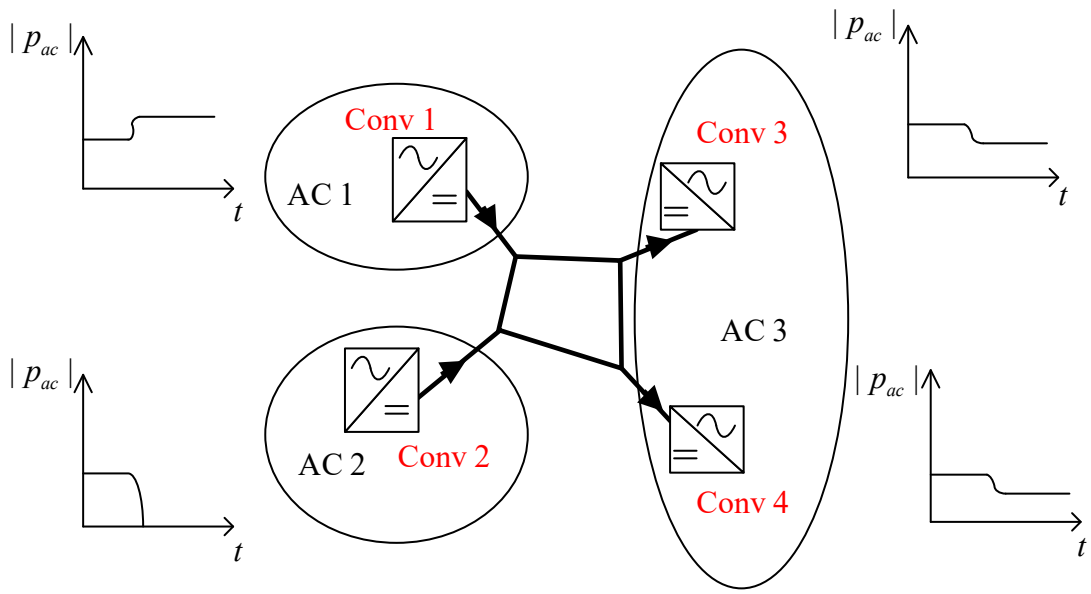

Figure 3.10: DC grid voltage droop control

3.4. Conclusion

This chapter has presented the methodology and modeling framework of this thesis. The prerequisite for eigenvalue-based SSSA is the state-space representation of system components. Therefore, the state-space models of two VSC topologies, a two-level and a modular multilevel topology, have been derived step-by-step. The two-level VSC model and the described DC grid control principles are used in Chapter 4 in the investigation of interaction modes in HVDC grids.

The MMC model is used in Chapters 5 and 6 for the modeling of the HVDC infeed to the connecting AC grid.

4. SMALL-SIGNAL STABILITY ANALYSIS OF INTERACTION MODES IN VSC MTDC SYSTEMS WITH VOLTAGE MARGIN CONTROL

Parts of this chapter have been published in: G. Grdenić and M. Delimar "Small-signal stability analysis of interaction modes in VSC MTDC systems with voltage margin control," Energies, vol. 10, no. 873, 2017. [39]

The main initiator of the development of MTDC grids is offshore wind generation. However, prior to their construction, a thorough investigation of different aspects of their implementation and operation is required. In this chapter, an MTDC grid with voltage margin control consisting of VSCs and a high-frequency cable model is implemented in Matlab/SIMULINK. A SSSA is carried out to investigate the sensitivity of the grid's interaction modes to the operating point, the structure of the grid, and the selection of the voltage controlling converter. Based on the findings of these analyses, a strategy for the droop control method is proposed and demonstrated.

4.1. Introduction

The deployment of VSCs has enabled the implementation of truly meshed MTDC grids since the power reversal in converters is possible without changing the voltage polarity. However, before the wide commissioning of HVDC grids, researchers worldwide are investigating different aspects of their control, operation and protection [40-44]. In this context, a SSSA is an analytical methodology tool that can provide answers to several questions.

A SSSA is essential for all dynamic systems to provide detailed insight into its behavior and has been used by a number of researchers to analyze the dynamic properties of VSCs within a frame of HVDC transmission. Many studies have used modal and participation factor analysis to investigate the interactions between the MTDC grid and the AC grid [45, 46]. It was shown that a clear distinction exists between the modes corresponding to AC and DC grid states. In [46], a sensitivity analysis of the control modes was performed with respect to gains in voltage droop control and converter capacitance. Similar research was done in [47], where investigators also explored the sensitivity of eigenvalues to droop gains and to the capacitance of the DC link. A detailed impact of VSC controls on the stability of MTDC grid and connecting AC system was

completed in [48, 49]. A SSSA was used to show that the maximum power transfer capability of a VSC was dependent on gains of the PLL and the SCR of the system. However, a few studies have been undertaken to explore the sensitivity of eigenvalues of the MTDC grid with respect to the operating point of the system. In [50], the authors tracked the eigenvalues of two-terminal and three-terminal systems under different loading conditions, that is, operating points and different gains of the DC voltage controller.

As in an AC system, oscillation modes in DC grids can be divided into local and interarea modes. The importance of interarea modes lies in the interaction of two converters which deteriorates the desired control actions. In [34], researchers established a methodology for identifying the interaction modes and conducted a parametric sensitivity analysis of the interaction modes with respect to line inductance (simulating the effects of DC circuit breakers) and variations of droop gains within voltage droop control.

MTDC grids, in this chapter, have been modeled with voltage margin control for two reasons. First, the number of interaction modes with such control is smaller than with droop control–as shown in [34]–which makes the analysis simpler. Second (and more important), this grid control method has some basic concepts that could possibly be generalized to droop control. As the sensitivity of interaction modes in a DC grid with respect to the operating point and structure of the grid has not been investigated thoroughly thus far, this is the main objective of this work. Furthermore, the study in this chapter also examines the stability of the dominant interaction mode with respect to the selection of a voltage controlling converter. A voltage controlling converter is mostly selected upon circumstances in connecting AC grid; however, in this research, another selection criteria, directly linked to the system's stability, is established.

The modeling of the DC grid consisting of VSCs and cables is described in Section 4.2. The methodology for identifying interaction modes from [34] is described in Section 4.3 and applied to a simple three-terminal DC grid. Sections 4.4 and 4.5 present the results and the discussion of the proposed analyses. A synthesis of the obtained conclusions is given in Section 4.6.

4.2. Modeling of MTDC grid

The lossless time-averaged dynamic model of the two-level VSC has been taken and adjusted from references [35, 36]. State-space vectors of rectifier and inverter are presented by (3.39) and (3.40) in Section 3.2.1 and repeated here for convenience reasons:

$$\mathbf{x_{rec}} = \left[i_{cv,d}\ i_{cv,q}\ v_{o,d}\ v_{o,q}\ v_{dc}\ \gamma_d\ \gamma_q\ \rho_d\ \rho_q\ \varepsilon_{PLL}\ \Delta\Theta_{PLL} \right], \tag{4.1}$$

$$\mathbf{x_{inv}} = \left[i_{cv,d}\ i_{cv,q}\ v_{o,d}\ v_{o,q}\ v_{dc}\ \gamma_q\ \rho_d\ \rho_q\ \varepsilon_{PLL}\ \Delta\Theta_{PLL} \right], \tag{4.2}$$

where $i_{cv,d}$ and $i_{cv,q}$ are the converter currents, $v_{o,d}$ and $v_{o,q}$ are the PCC voltages, v_{dc} is the DC side voltage, γ_d and γ_q are the integrator states of the ICC, ρ_d and ρ_q are the integrator states of outer controllers, ε_{PLL} and $\Delta\Theta_{PLL}$ are the PLL state variables.

The vector fitting method has been used for modeling the frequency dependent cable parameters [51-53]. The model consists of several π-sections that account for distributed line parameters while in each π-section there is a connection of multiple parallel branches. Cable model without frequency dependency can lead to false conclusions on the stability of HVDC systems. More details can be found in [54], and based on the results from that article, the cable model with five π-sections each with three parallel branches has been used in this research. In Fig. 4.1 R_{line}, L_{line} and C_{line} are the line resistance, inductance and capacitance, and L is the line length. The state-space representation of this cable model has 21 state variables (15 branch currents and six node voltages). Typical frequency dependency of cable resistance and inductance can be found in Appendix A. Here, it is important to emphasize that there also exist other methods for modeling frequency dependent cable parameters, but this approach–taken from [54]–is adjusted for a state-space representation.

4.3. Identification of interaction modes

A radial DC grid consisting of three converters (Fig. 4.2) has been built in Matlab/SIMULINK (R 2015b, The MathWorks, Inc., Natick, MA, USA). The electric and control parameters of all converters are equal and are given in Appendix A, where the parameters of the cables are also provided. The powers of the converters are equal to $P_{ac1} = 95.42\ \text{MW}$ (inverter), $P_{ac2} = -50\ \text{MW}$ and $P_{ac3} = -50\ \text{MW}$ (rectifiers), and all line lengths are equal to 100 km. One

converter (converter 1) regulates the DC voltage to the reference value (1 pu), while other converters regulate active power, that is, voltage margin control is employed in the grid. The model is linearized around the operating point using the Matlab *Linear Analysis Tool* and the system eigenvalues and eigenvectors are extracted. The model has 84 state variables altogether and therefore 84 eigenvalues. Since the emphasis in this chapter is on the DC grid dynamics, the PCC voltages are not represented as state variables.

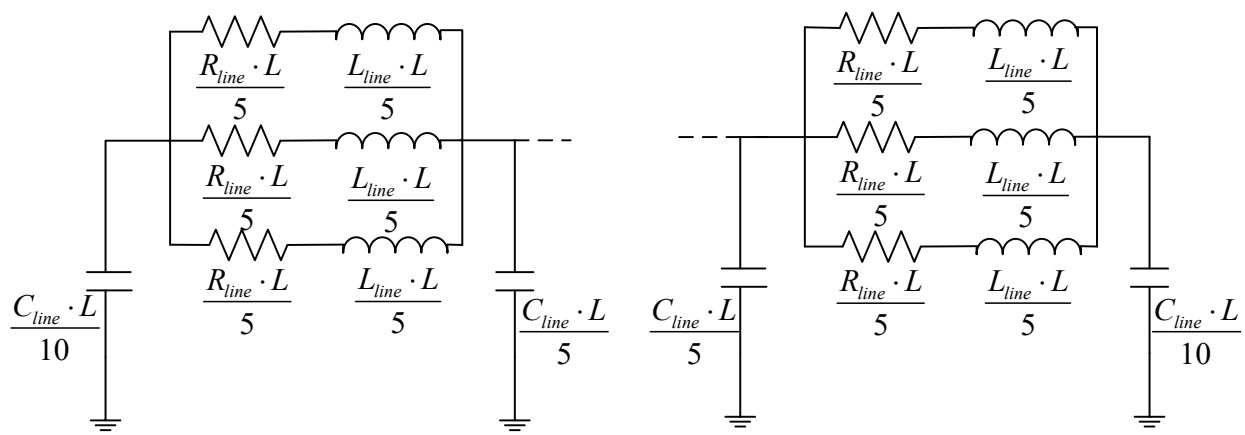

Figure 4.1: Frequency dependent cable model with five π-sections and three parallel branches

Similar to the definition from an AC grid, the modes in a DC grid can be classified as local modes—if they are related to the states from only one subsystem, or interaction modes—if they are related to the state variables from several subsystems. To determine whether a particular mode is local or interactive, a subsystem participation $p_{\alpha,i}$ defined in Section 3.1.2 is used:

$$p_{\alpha,i} = \sum p_{ki} \quad | x_k \in \alpha , \tag{4.3}$$

where p_{ki} is the normalized participation of state variable x_k in mode λ_i, and α is the set of state variables describing a particular subsystem. A mode is classified as an interaction mode if there exist at least two subsystems for which holds $p_{\alpha,i} > \mu$, where μ is the predefined threshold.

In this research, three subsystems corresponding to the three converters are considered. The threshold μ is set to 5% to obtain a limited set of interaction modes. After conducting the described analysis, there are three interaction modes identified, shown in Fig. 4.3: $\lambda_1 = -206.13 \pm j \cdot 1027.9$, $\lambda_2 = -185.65 \pm j \cdot 1026.8$, and $\lambda_3 = -15.33 \pm j \cdot 10.64$. Fig. 4.4 displays the normalized participation factors of these three modes related to converters' state variables. Modes 1 and 2 are

related to the state variables of converter DC voltages: $v_{dc,1}$, $v_{dc,2}$, $v_{dc,3}$; and mode 3 along with the DC voltages, is mostly related to the integrator state variable of the DC voltage controller at converter 1 (ρ_{d1}). Participation factors of the other converter state variables are negligible. Of these three modes, the most significant is mode 3 as its real part is the closest to the origin of a complex plane. This results in the visibility of this mode in the system response, so it is called the dominant mode.

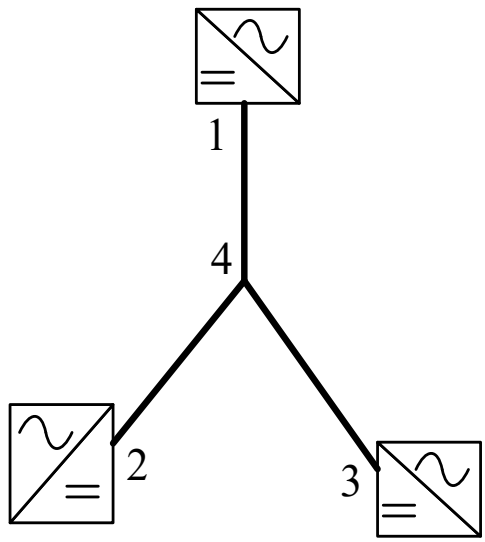

Figure 4.2: Radial DC grid with three converters

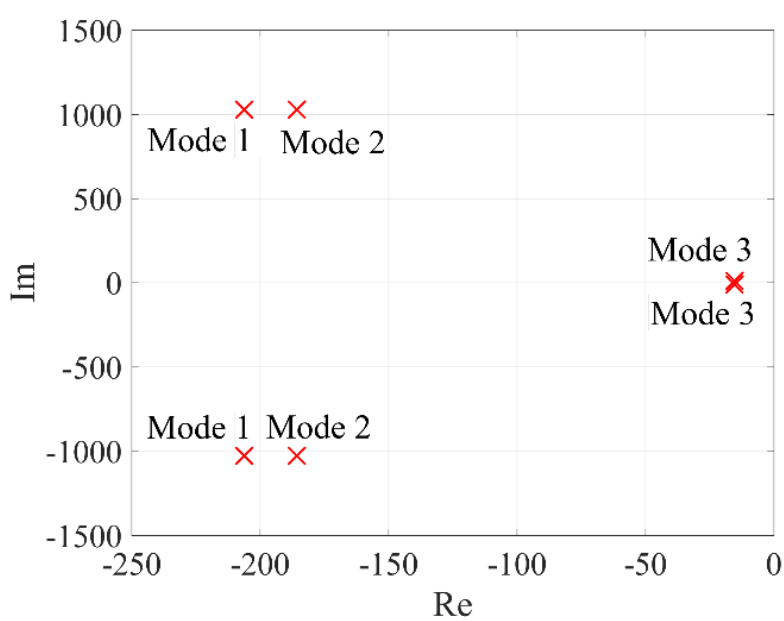

Figure 4.3: Interaction modes of the system from Fig. 4.2

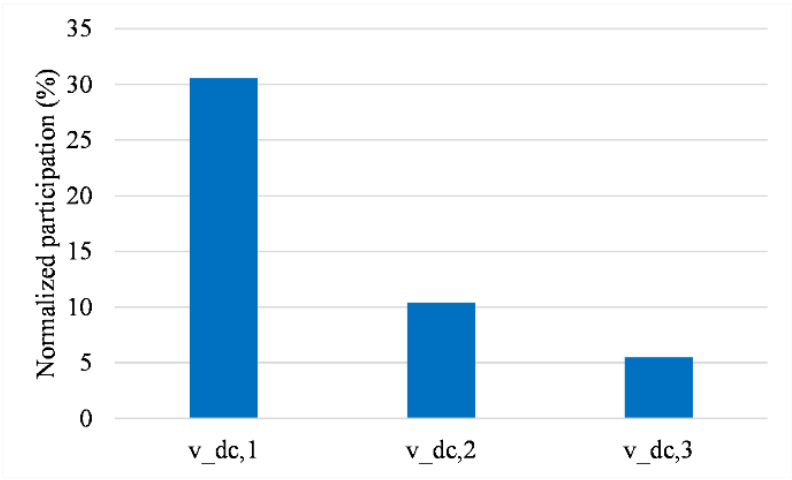

a)

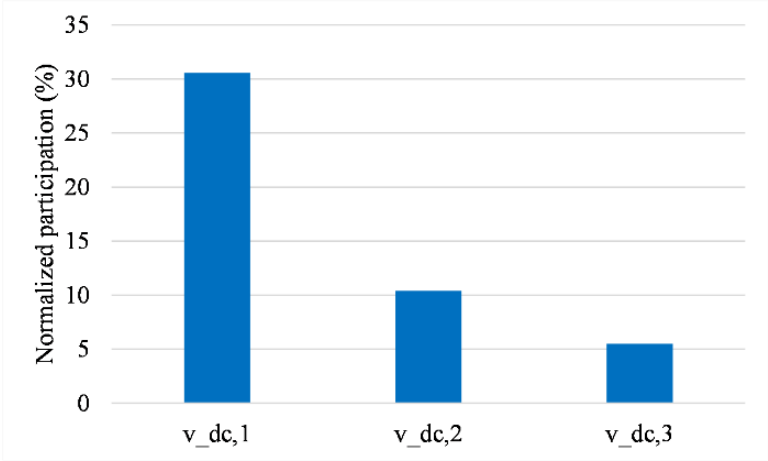

b)

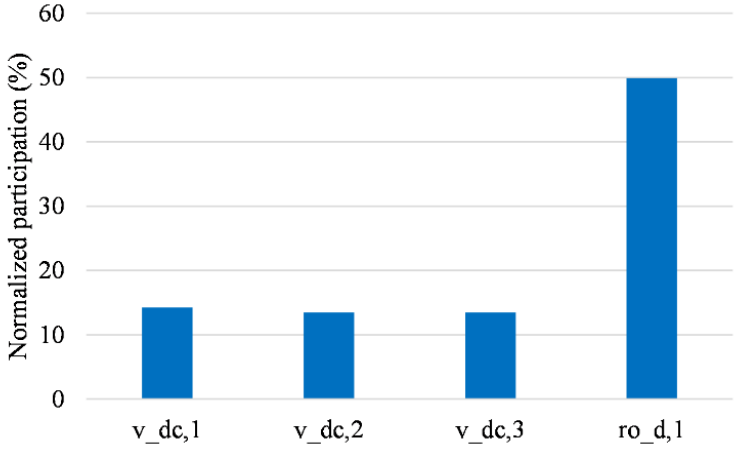

c)

Figure 4.4: Normalized participation factors of interaction modes: a) mode 1; b) mode 2; c) mode 3

4.4. Sensitivity of the interaction modes to the operating point and structure of the grid

This section contains the results and discussion of the sensitivity analysis of interaction modes in the grid to the operating point and, to some extent, to the structure of the grid. All simulations are conducted using the grid from Fig. 4.2. In Section 4.4.1, active powers of all converters in the grid are varied linearly at the same rate. Section 4.4.2 observes the grid's small-signal stability when the active power of one of the power controlling converters is held constant while in Section 4.4.3, the active power of the voltage controlling converter is held constant. Section 4.4.4 investigates the influence of the line lengths and Section 4.4.5 observes the magnitude of the reference voltage. In all study cases, converter 1 is always in charge of the voltage control in the grid while converters 2 and 3 regulate active power. The lengths of all lines are equal to 100 km, except in Section 4.4.4 where different line lengths are considered.

4.4.1. Varying active powers of all converters

The operating state of the grid varies according to Table 4.1. Powers of all converters increase linearly at the same rate. Converter 1 is in inverter operation mode, while converters 2 and 3 operate as rectifiers. Table 4.1 also contains the damping ratios of interaction modes, which are graphically depicted in Fig. 4.5.

Table 4.1: Converter powers and damping ratios of interaction modes (case 4.4.1a)

	$P_{ac,1}$ [MW]	$P_{ac,2}$ [MW]	$P_{ac,3}$ [MW]	ζ_1	ζ_2	ζ_3
pt 1	19.80	-10	-10	0.18	0.17	0.18
pt 2	39.23	-20	-20	0.18	0.17	0.35
pt 3	58.29	-30	-30	0.19	0.17	0.52
pt 4	77.02	-40	-40	0.19	0.18	0.67
pt 5	95.42	-50	-50	0.20	0.18	0.82

The real parts of all three interaction modes move to the left in the complex plane as designated by the arrows in Fig. 4.5 and damping ratios of all modes increase. The grid becomes more stable with an increased transmitted active power. The change is the most prominent in the most significant (dominant) interaction mode 3. This can be explained by the fact (as we have seen in the previous section in participation factors from Fig. 4.4 that modes 1 and 2 are mostly dependent on direct voltage state variables, while mode 3 (apart from direct voltages) is also

dependent on the integrator state of direct voltage controller ($\rho_{d,1}$). Here, it is important to emphasize that the described behavior of mode 3 is valid in the range in which this mode has an oscillatory shape. This also applies for other considerations in the rest of the chapter regarding this mode.

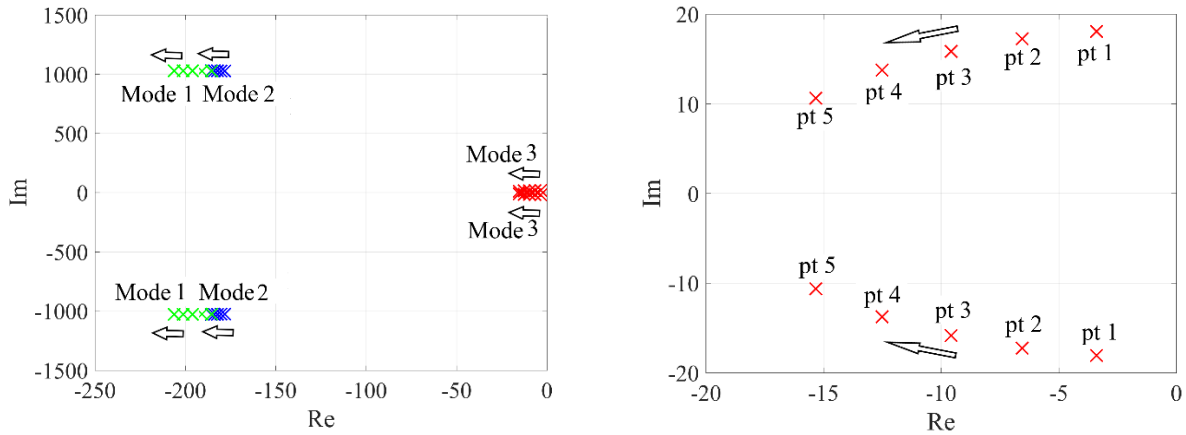

a) b)

Figure 4.5: Interaction modes (case 4.4.1a): a) all; b) zoom-in of mode 3

The SSSA is verified through time-domain simulations shown in Fig. 4.6. At $t = 10\,\mathrm{s}$, the reference voltage of converter 1 is changed from 1 to 1.02 pu. With the lowest active power in the grid (pt 1), the voltage transients have the highest amplitude of oscillations and are damped the least. By increasing the converter powers, the voltage response becomes less oscillatory and more damped.

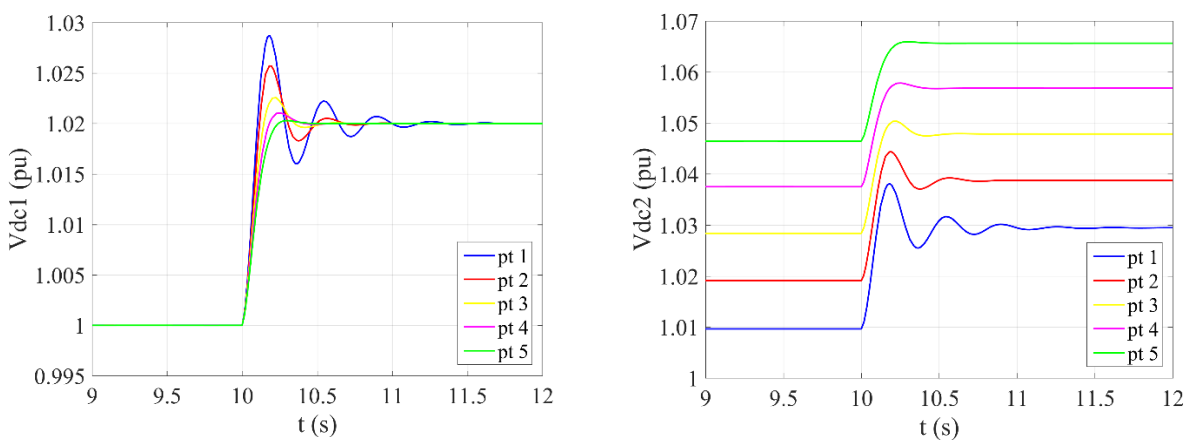

a) b)

Figure 4.6: Time-domain simulations (case 4.4.1a): a) direct voltage 1; b) direct voltages 2 and 3

In the case where there are two inverters and one rectifier in the grid, the behavior of interaction modes becomes slightly different. The powers of converters and damping ratios of interaction modes are listed in Table 4.2 and the interaction modes are shown in Fig. 4.7. Mode 2 becomes less stable as it moves to the right in the complex plane and its damping ratio decreases. Of importance is that the dominant mode 3 behaves in the same way as in the previous example.

Table 4.2: Converter powers and damping ratios of interaction modes (case 4.4.1b)

	$P_{ac,1}$ [MW]	$P_{ac,2}$ [MW]	$P_{ac,3}$ [MW]	ζ_1	ζ_2	ζ_3
pt 1	9.90	-20	9.90	0.18	0.17	0.09
pt 2	19.62	-40	19.62	0.18	0.17	0.17
pt 3	29.15	-60	29.15	0.19	0.16	0.25
pt 4	38.50	-80	38.50	0.19	0.16	0.31
pt 5	47.71	-100	47.71	0.20	0.16	0.37

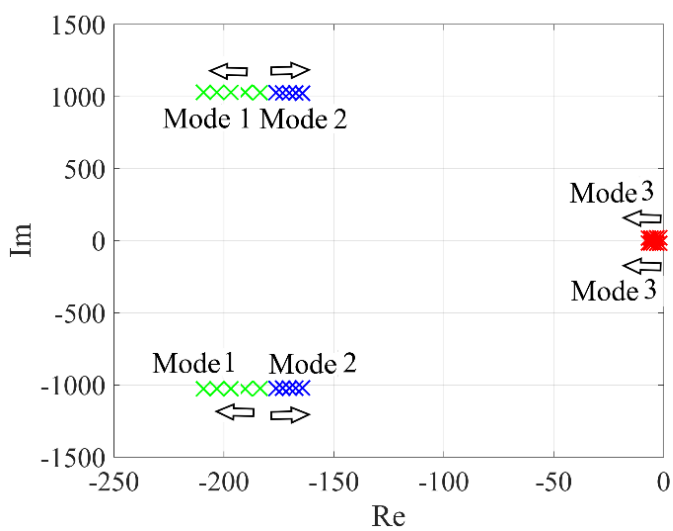

Figure 4.7: Interaction modes (case 4.4.1b)

4.4.2. Active power of power controlling converter held constant

In this case, the active power of converter 2 (one of the power controlling converters) is held constant, while the powers of converters 1 and 3 are varied. The operating points with damping ratios of the interaction modes are shown in Table 4.3. All interaction modes in this scenario become more stable, as can be seen from Fig. 4.8. A strong correlation between the stability of mode 3 and power through converter 1 (voltage controlling converter) can be established.

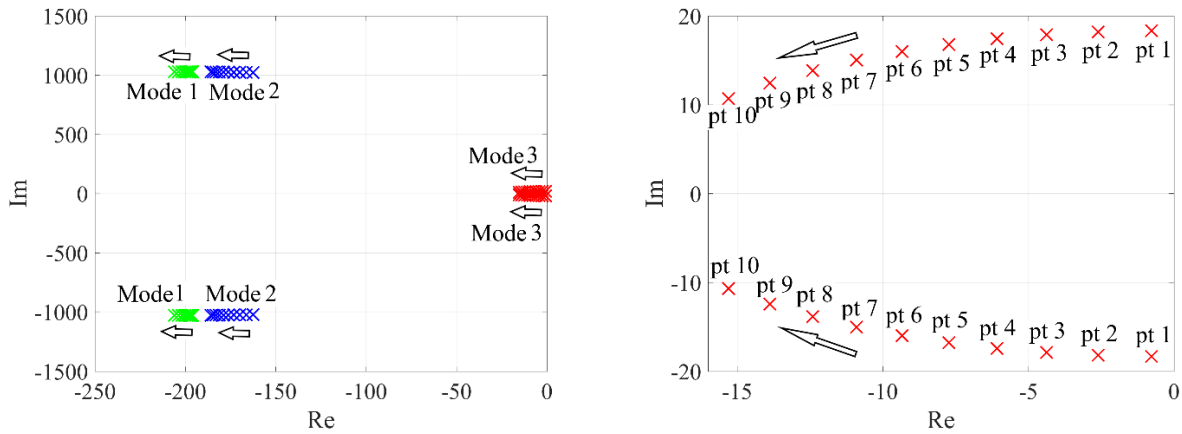

a) b)

Figure 4.8: Interaction modes (case 4.4.2): a) all; b) zoom-in of mode 3

Table 4.3: Converter powers and damping ratios of interaction modes (case 4.4.2)

	$P_{ac,1}$ [MW]	$P_{ac,2}$ [MW]	$P_{ac,3}$ [MW]	ζ_1	ζ_2	ζ_3
pt 1	7.96	-60	50	0.19	0.16	0.04
pt 2	18.20	-60	40	0.19	0.16	0.14
pt 3	28.29	-60	30	0.19	0.16	0.24
pt 4	38.24	-60	20	0.19	0.17	0.33
pt 5	48.07	-60	10	0.19	0.17	0.42
pt 6	57.76	-60	0	0.19	0.17	0.50
pt 7	67.34	-60	-10	0.19	0.17	0.59
pt 8	76.79	-60	-20	0.19	0.18	0.67
pt 9	86.13	-60	-30	0.19	0.18	0.75
pt 10	95.37	-60	-40	0.20	0.18	0.82

4.4.3. Active power of voltage controlling converter held constant

This scenario differs by the fact that the active power of voltage controlling converter is now held constant (converter 1), while the active powers of the other two converters are varied (Table 4.4). Fig. 4.9 shows the damping ratios of all three interaction modes. Modes 2 and 3 are the most stable in the middle of the characteristics and mode 1 is the least stable in this area. The operating point in the middle of the characteristics (pt 8) corresponds to the most symmetrical state in the grid, with the most similar powers of converters 2 and 3.

Table 4.4: Converter powers (case 4.4.3)

	$P_{ac,1}$ [MW]	$P_{ac,2}$ [MW]	$P_{ac,3}$ [MW]
pt 1	60	-105.1	40
pt 2	60	-94.2	30
pt 3	60	-83.5	20
pt 4	60	-72.9	10
pt 5	60	-62.4	0
pt 6	60	-52.1	-10
pt 7	60	-41.9	-20
pt 8	60	-31.8	-30
pt 9	60	-21.9	-40
pt 10	60	-12	-50
pt 11	60	-2.4	-60
pt 12	60	7.3	-70
pt 13	60	16.8	-80
pt 14	60	26.1	-90
pt 15	60	35.4	-100

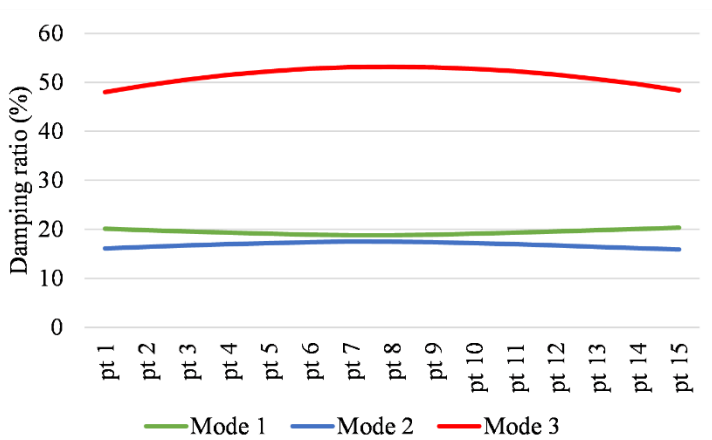

Figure 4.9: Damping ratios of interaction modes (case 4.4.3)

Here, it is also interesting to look at the participation factors of all interaction modes and how they change with different operating points (Fig. 4.10). It arises that mode 1 mostly depends on the voltage state(s) of the corresponding rectifier(s). At the first several points, only converter 2 injects the power into the DC grid, then both converter 2 and converter 3 inject the power, and at the last several points only converter 3 injects the power in the DC grid. A similar observation is valid for mode 2 which mostly depends on the voltage state(s) of the corresponding inverter(s).

The participation factors of mode 3 remain unaltered through all operating points in Table 4.4. Thus, from the participation factors of modes 1 and 2, it can be approximately determined if the converter is in rectifier or inverter operation mode.

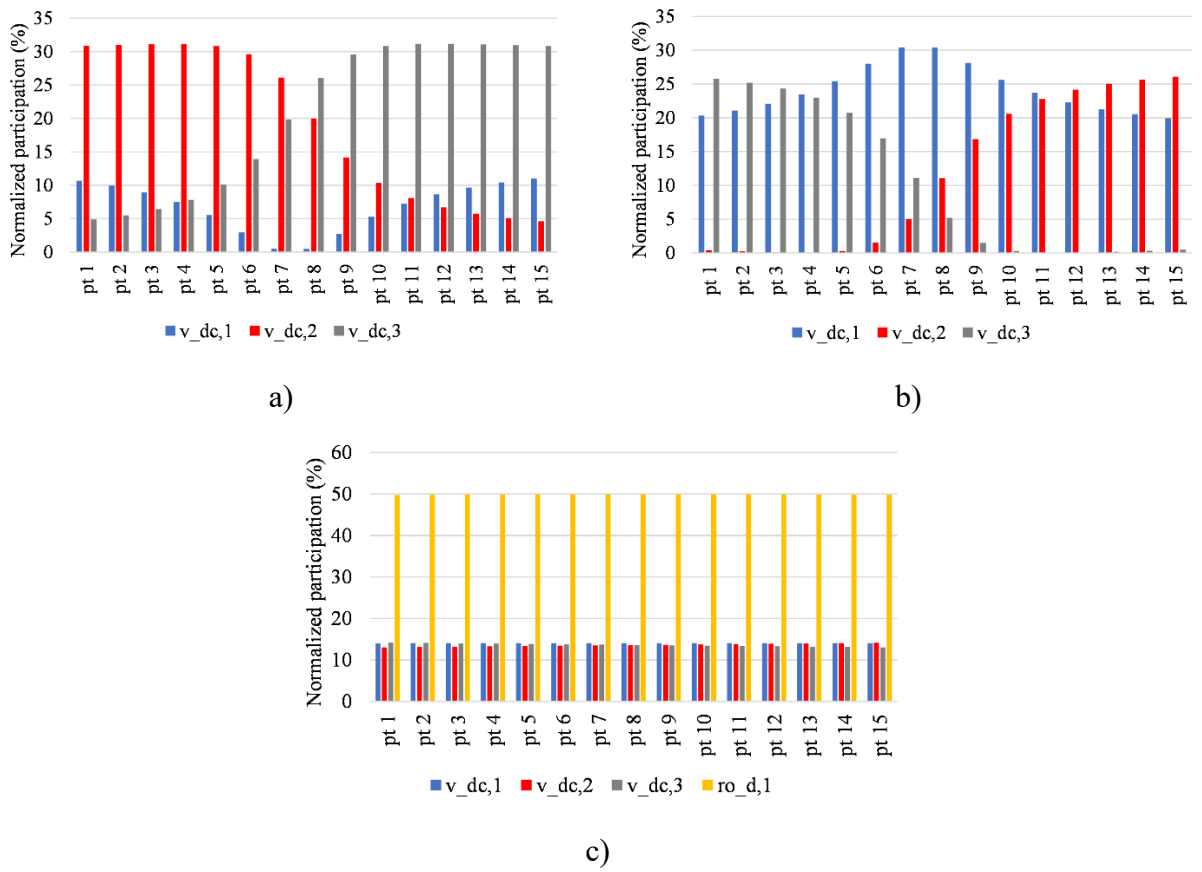

Figure 4.10: Normalized participation factors of interaction modes (case 4.4.3): a) mode 1; b) mode 2; c) mode 3

4.4.4. Varying electrical distance between converters

The line lengths to all three converters are increased linearly at the same rate, and the results are shown in Table 4.5 and in Fig. 4.11. The powers of the rectifiers remain the same while the power of the voltage controlling inverter slightly changes due to the different losses in the system. Damping ratios of modes 1 and 2 increase, but the damping ratio of mode 3 nevertheless decreases. In addition, it has been verified that all modes behave in the same way in the case of two inverters and one rectifier in the grid.

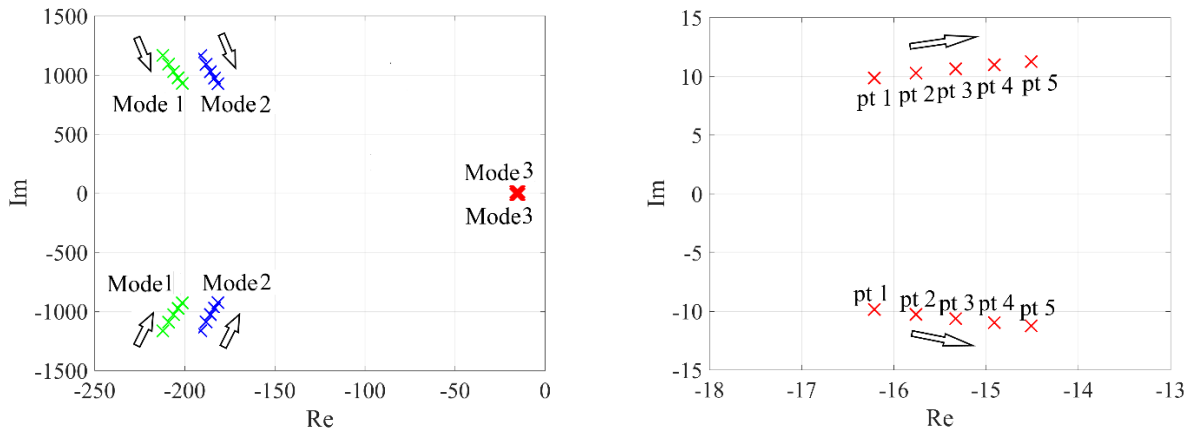

a) b)

Figure 4.11: Interaction modes (case 4.4.4): a) all; b) zoom-in of mode 3

Table 4.5: Line lengths, converter powers and damping ratios of interaction modes (case 4.4.4)

	L_1, L_2, L_3 [km]	$P_{ac,1}$ [MW]	$P_{ac,2}$ [MW]	$P_{ac,3}$ [MW]	ζ_1	ζ_2	ζ_3
pt 1	80	96.25	-50	-50	0.18	0.16	0.85
pt 2	90	95.83	-50	-50	0.19	0.17	0.84
pt 3	100	95.42	-50	-50	0.20	0.18	0.82
pt 4	110	95.02	-50	-50	0.20	0.19	0.81
pt 5	120	94.62	-50	-50	0.21	0.19	0.79

4.4.5. Varying the reference voltage magnitude

The goal of this section is to examine how the magnitude of the reference voltage affects the stability of the interaction modes. It can be observed in Table 4.6 and Fig. 4.12 that the stability of all modes decreases with higher voltages in the grid. The change is expressed the most in mode 3 and the least in mode 2. However, it has been verified that in the case of two inverters and one rectifier in the grid, mode 2 behaves differently and becomes less stable with higher voltages in the grid.

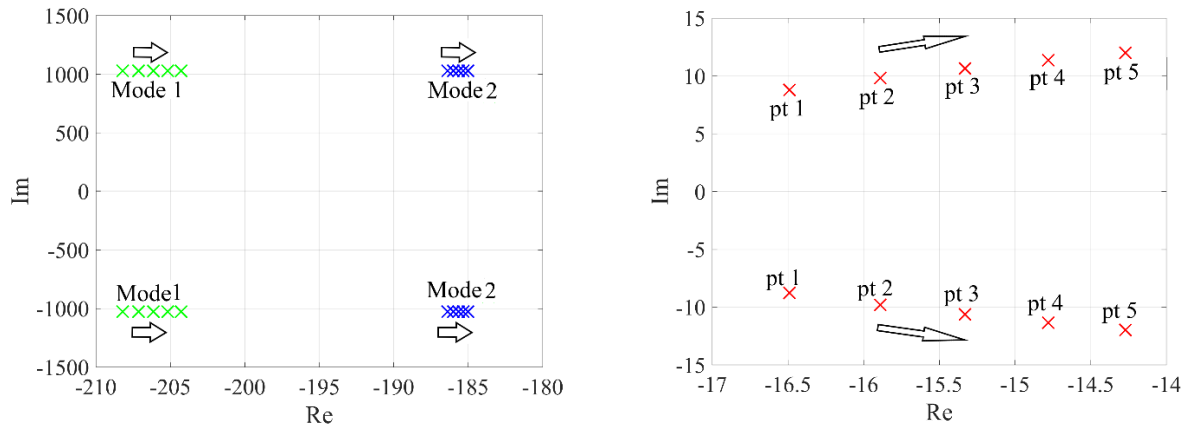

a) b)

Figure 4.12: Interaction modes (case 4.4.5): a) modes 1 and 2; b) mode 3

Table 4.6: Reference voltages, converter powers and damping ratios of interaction modes (case 4.4.5)

	$v_{dc,1}$ [pu]	$P_{ac,1}$ [MW]	$P_{ac,2}$ [MW]	$P_{ac,3}$ [MW]	ζ_1	ζ_2	ζ_3
pt 1	0.96	95.08	-50	-50	0.20	0.18	0.88
pt 2	0.98	95.25	-50	-50	0.20	0.18	0.85
pt 3	1.00	95.42	-50	-50	0.20	0.18	0.82
pt 4	1.02	95.58	-50	-50	0.20	0.18	0.79
pt 5	1.04	95.73	-50	-50	0.19	0.18	0.77

4.5. Sensitivity of the dominant mode to the selection of voltage controlling converter

The goal of this study is to determine what the best location is, that is, which inverter is the most appropriate to control the voltage in the grid, with respect to the stability of the interaction modes. In this section, only the mode with the lowest absolute value of real part is considered for two reasons: this mode mostly affects the response of the system and this mode (as seen from the participation factor analysis) is mostly affected by the integrator state of the voltage regulator at the voltage controlling converter. Tests in Sections 4.5.1–4.5.3 are carried out on the same grid as in Fig. 4.2, where one converter operates in rectifier mode (converter 1) while the other two converters operate in inverter mode (converters 2 and 3). Since the dominant mode has relatively

low frequency, the cable model with one π-section and one parallel branch is used. Rectifier voltage ($v_{dc,1}$) is always held at 1 pu.

4.5.1. Two inverters with different active powers and equal line lengths

All line lengths are equal to 100 km. The active power of converter 3 changes in steps of 1 MW as seen in Table 4.7, which also displays the converter voltages and currents as well as the damping ratios of dominant interaction modes for two cases: when converter 2 controls the voltage in the grid and when converter 3 controls the voltage in the grid. These modes are depicted in Fig. 4.13: red for converter 2 and blue for converter 3. While increasing the power of converter 3, the dominant interaction mode when converter 3 is in charge of voltage control becomes more stable (as we have seen previously due to higher power) and the dominant interaction mode when converter 2 is in charge of voltage control becomes less stable in this situation, which is indicated by the arrows in Fig. 4.13. This is valid for both the real parts of the interaction modes and for the damping ratios of the interaction modes. Higher stability of the dominant interaction mode, in this case, is achieved when the voltage controlling converter is the one with the higher power (or current). Of course, when the powers (currents) of the converters are equal, the corresponding modes are also equal (point 3).

Table 4.7: Converter powers, voltages, currents and damping ratios of dominant interaction modes (case 4.5.1)

	$P_{ac,1}$ [MW]	$P_{ac,2}$ [MW]	$P_{ac,3}$ [MW]	$v_{dc,1}$ [pu]	$v_{dc,2}$ [pu]	$v_{dc,3}$ [pu]	$i_{dc,2}$ [pu]	$i_{dc,3}$ [pu]	ζ_3 – conv 2	ζ_3 – conv 3
pt 1	-222.72	100	98	1	0.8914	0.8921	0.5609	0.5493	0.7298	0.7031
pt 2	-224.01	100	99	1	0.8909	0.8913	0.5612	0.5554	0.7257	0.7119
pt 3	-225.29	100	100	1	0.8905	0.8905	0.5615	0.5615	0.7208	0.7208
pt 4	-226.58	100	101	1	0.8901	0.8897	0.5617	0.5676	0.7166	0.7299
pt 5	-227.87	100	102	1	0.8896	0.8889	0.5621	0.5737	0.7119	0.7390

4.5.2. Two inverters with equal active powers and different line lengths

In order to study the effect of line lengths, the powers of converters 2 and 3, in this case, are held equal to 100 MW, but the length of the line to converter 3 is changed from 90 to 110 km in steps of 5 km. The lengths of the lines to converters 1 and 2 are held constant at 100 km. Table 4.8 contains all important data (line lengths to converter 3, converter powers, voltages and currents,

damping ratios of the interaction modes in the same two cases as in the previous subsection). The evolution of the dominant interaction modes is also depicted in Fig. 4.14. The interaction mode becomes less stable when converter 2 is in charge of voltage control (red labels), whereas stability of the interaction mode only changes slightly when converter 3 is in charge of voltage control (blue labels). From Table 4.8, it can be seen that the dominant mode is more stable if the voltage controlling converter has a smaller voltage and consequently a higher current (as powers of both converters are equal). Thus, it can be concluded that the magnitude of converter current (or voltage) can provide better insight into the small-signal stability of the grid.

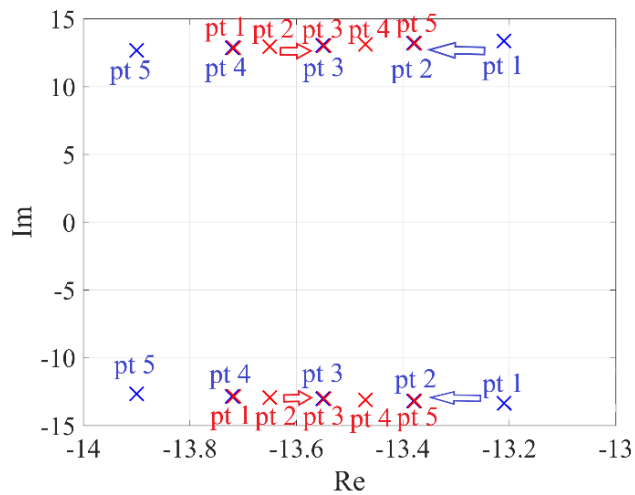

Figure 4.13: Dominant interaction modes (case 4.5.1)

Table 4.8: Line lengths, converter powers, voltages, currents and damping ratios of dominant interaction modes (case 4.5.2)

	L_3 [km]	$P_{ac,1}$ [MW]	$P_{ac,2}$ [MW]	$P_{ac,3}$ [MW]	$v_{dc,1}$ [pu]	$v_{dc,2}$ [pu]	$v_{dc,3}$ [pu]	$i_{dc,2}$ [pu]	$i_{dc,3}$ [pu]	$\zeta_3 -$ conv 2	$\zeta_3 -$ conv 3
pt 1	90	-224.77	100	100	1	0.8907	0.8945	0.5614	0.5590	0.7361	0.7203
pt 2	95	-225.03	100	100	1	0.8906	0.8925	0.5614	0.5602	0.7285	0.7205
pt 3	100	-225.29	100	100	1	0.8905	0.8905	0.5615	0.5615	0.7208	0.7208
pt 4	105	-225.56	100	100	1	0.8904	0.8885	0.5615	0.5627	0.7131	0.7211
pt 5	110	-225.82	100	100	1	0.8903	0.8865	0.5616	0.5640	0.7055	0.7229

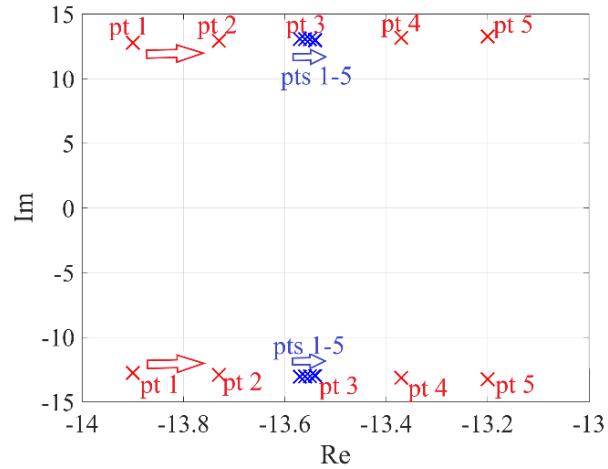

Figure 4.14: Dominant interaction modes (case 4.5.2)

4.5.3. Two inverters with different active powers and different line lengths

In this case study, the active power of converter 3 again changes in steps of 1 MW, as in Section 4.5.1, but the line lengths to converters 2 and 3 are different: 100 km to converter 2 and 60 km to converter 3 (line length to converter 1 is equal to 100 km). From Table 4.9 and Fig. 4.15, it can be seen that the interaction mode becomes less stable when the voltage controlling converter is converter 2 (red labels) and the interaction mode becomes more stable when the voltage controlling converter is converter 3 (blue labels) by increasing the power of converter 3. The real parts of the interaction modes are equal when the power of converter 3 is 105.5 MW and their damping ratios are equal when the power of converter 3 is slightly below 105 MW. Currents of these two converters are equal with a power at converter 3 of 101.6 MW.

Table 4.9: Converter powers, voltages, currents and damping ratios of dominant interaction modes (case 4.5.3)

	$P_{ac,1}$ [MW]	$P_{ac,2}$ [MW]	$P_{ac,3}$ [MW]	$v_{dc,1}$ [pu]	$v_{dc,2}$ [pu]	$v_{dc,3}$ [pu]	$i_{dc,2}$ [pu]	$i_{dc,3}$ [pu]	ζ_3 – conv 2	ζ_3 – conv 3
pt 1	-223.26	100	100	1	0.8912	0.9061	0.5610	0.5518	0.7797	0.7184
pt 2	-224.50	100	101	1	0.8908	0.9055	0.5613	0.5577	0.7764	0.7274
pt 3	-225.74	100	102	1	0.8904	0.9049	0.5615	0.5636	0.7727	0.7363
pt 4	-226.99	100	103	1	0.8899	0.9042	0.5619	0.5696	0.7693	0.7450
pt 5	-228.24	100	104	1	0.8895	0.9036	0.5621	0.5755	0.7658	0.7539
pt 6	-229.49	100	105	1	0.8892	0.9030	0.5623	0.5814	0.7619	0.7627
pt 7	-230.74	100	106	1	0.8887	0.9023	0.5626	0.5874	0.7586	0.7715

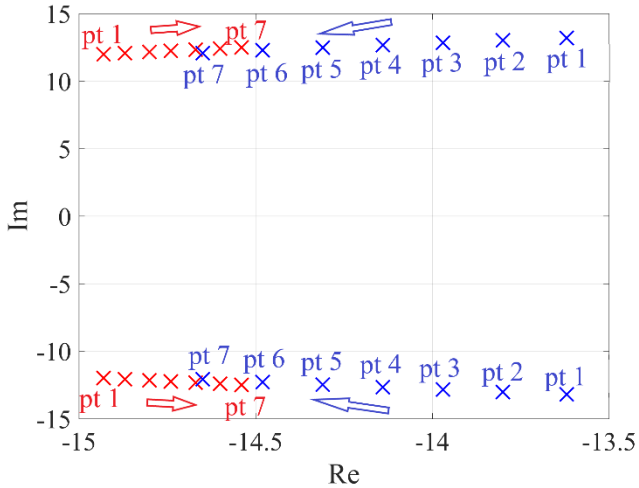

Figure 4.15: Dominant interaction modes (case 4.5.3)

The same procedure is repeated with different line lengths to converter 3 and the results are shown in Fig. 4.16. The powers of converter 3 are in the middle of the figure (x-axis) and the line lengths are on the left side of the figure (y-axis). Blue lines mark the power of converter 3 when it has the same current as converter 2, and red lines mark the power of converter 3 when it has the same real part of the dominant interaction mode (with respect to converter 2 with a power of 100 MW and line length of 100 km). Since the real parts and damping ratios of dominant interaction modes behave in the same way and the corresponding converter power does not differ much, considering only real parts of interaction modes as a measure of mode stability will not affect the results and conclusions drawn from this analysis.

Left from the blue lines is the area of lower current, and right from the blue lines is the area of higher current (compared with the converter 2 current). Likewise, left from the red lines is the area of lower stability, and right from the red lines is the area of higher stability of the dominant interaction mode (in comparison to the dominant interaction mode when converter 2 oversaw voltage control). The following conclusion can be drawn by comparing the positions of red and blue lines: if a converter with a higher power has a lower current, then the stability of the dominant interaction mode is lower (when it is in charge of voltage control) and if a converter with a smaller power has a higher current, then the stability of the dominant interaction mode is higher (when it is in charge of voltage control). However, the opposite does not work, that is, if a converter with a higher power has a higher current, we do not know if the stability of the dominant interaction mode is higher or lower (when it is in charge of voltage control), or if a converter with a lower power has

a lower current, we do not know if the stability of the dominant interaction mode is higher or lower (when it is in charge of voltage control). These conclusions help us to make assessments on the stability of the dominant interaction mode without carrying out a small-signal stability calculation of the grid. Similar conclusions can be drawn using converter voltages instead of currents, but in the continuation of this study, the formulation using converter currents will be used.

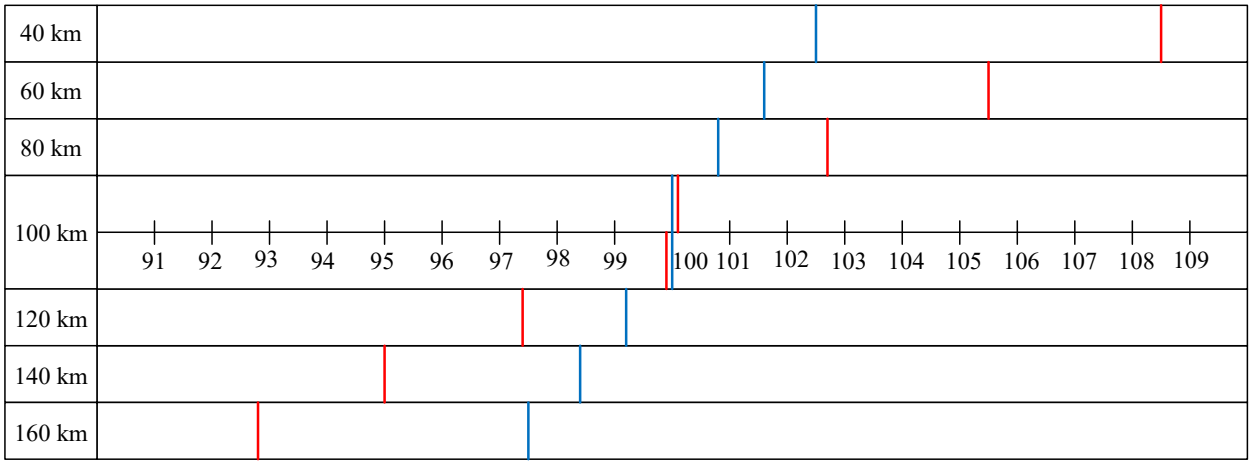

Figure 4.16: Points of equal currents and stability of the dominant interaction modes (case 4.5.3)

4.5.4. Triangular DC grid

The tests conducted in Sections 4.5.1-4.5.3 are repeated on a simple triangular grid shown in Fig. 4.17. The goal is to determine whether the structure of the grid–delta or star configuration of the connecting cables–affects the derived conclusions. For these reasons, the star-delta transformations of cable reactances and resistances (cable lengths, respectively) are conducted by well-known expressions:

$$
\begin{aligned}
L_{12} &= L_1 + L_2 + \frac{L_1 \cdot L_2}{L_3} \\
L_{13} &= L_1 + L_3 + \frac{L_1 \cdot L_3}{L_2} \\
L_{23} &= L_2 + L_3 + \frac{L_2 \cdot L_3}{L_1}.
\end{aligned}
\tag{4.4}
$$

Thus, the voltages and currents of all converters remain unaltered. This grid has three interaction modes and their values do not differ much from the case of a radial connected grid. Again, only the mode with the lowest absolute value of the real part is observed. In all cases, as in previous sections, converter 1 is in rectifier operation mode while converters 2 and 3 are in inverter

operation mode. In the first case, all line lengths are equal to 300 km, calculated by equation (4.4), and the results of varying converter 3 power are shown in Table 4.10 in addition to Table 4.7. When the voltage controlling converter is the one with a higher power, the dominant interaction mode has higher stability.

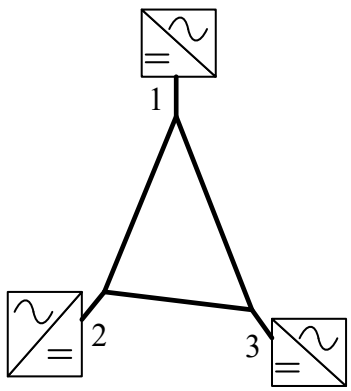

Figure 4.17: Triangular DC grid

Table 4.10: Damping ratios of dominant interaction modes (case 4.5.4a)

	ζ_3 – conv 2	ζ_3 – conv 3
pt 1	0.6320	0.6089
pt 2	0.6283	0.6165
pt 3	0.6242	0.6242
pt 4	0.6204	0.6320
pt 5	0.6162	0.6398

In the second case, the line lengths are varied based on the data from Table 4.11 and the powers of converters 2 and 3 are equal to 100 MW (Table 4.8). It can be seen that the dominant interaction mode is more stable when the corresponding converter has a higher current (and consequently a lower voltage). In the third case, the line lengths are equal to: $L_{12} = 367.67\,\text{km}$, $L_{13} = 220\,\text{km}$ and $L_{23} = 220\,\text{km}$; the power of converter 2 is held constant at 100 MW; and the power of converter 3 is varied (Tables 4.9 and 4.12). The same real part of the dominant interaction mode is achieved when the power of converter 3 is slightly above 105.5 MW and the same damping ratio when the power of converter 3 is slightly below 105 MW, in comparison to the scenario when converter 2 oversaw voltage control in the grid. These results are slightly different from the values obtained in Section 4.5.3. Converter 3 has the same current as converter 2 at the power of 101.6 MW. In the same way as in Section 4.5.3, it can also be concluded that if a certain converter of higher power has a lower current, then the stability of the dominant interaction mode (when this converter oversaw voltage control in the grid) is certainly lower compared to the scenario when another converter is in charge of voltage control. Thus, it is ascertained that the conclusions drawn for a radial-connected grid are also valid for a grid in triangular configuration.

Table 4.11: Line lengths and damping ratios of dominant interaction modes (case 4.5.4b)

	L_1 [km]	L_2 [km]	L_3 [km]	ζ_3 – conv 2	ζ_3 – conv 3
pt 1	311.11	280	280	0.6815	0.6273
pt 2	205.26	290	290	0.6784	0.6350
pt 3	300	300	300	0.6753	0.6427
pt 4	295.24	310	310	0.6722	0.6505
pt 5	290.91	320	320	0.6693	0.6583

Table 4.12: Damping ratios of dominant interaction modes (case 4.5.4c)

	ζ_3 – conv 2	ζ_3 – conv 3
pt 1	0.6815	0.6273
pt 2	0.6784	0.6350
pt 3	0.6753	0.6427
pt 4	0.6722	0.6505
pt 5	0.6693	0.6583
pt 6	0.6662	0.6661
pt 7	0.6627	0.6737

4.5.5. Radial DC grid with multiple nodes

The derived conclusions are also examined for the radial grid with five converters (Fig. 4.18) to generalize them to any radial or star-connected grid. Converter 1, as in previous sections, is in rectifier operation mode, and the other four converters are in inverter operation mode. In the first case (Table 4.13), the corresponding line lengths for all inverters are equal, but their powers differ. The most appropriate converter for grid voltage control with respect to the stability of the dominant interaction mode is, as expected, the one with the highest power, that is converter 5 (Table 4.13).

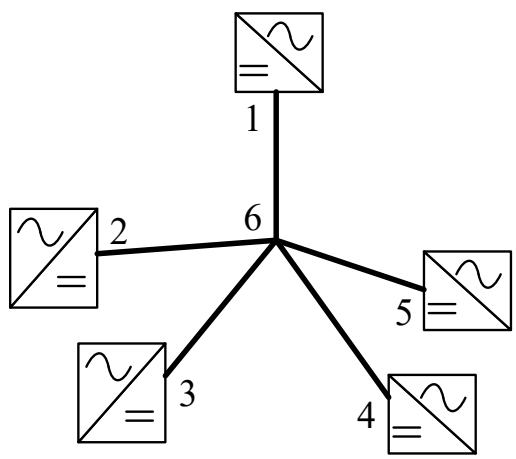

Figure 4.18: Radial DC grid with five converters

In the second case, all inverters have the same powers, but their line lengths from the central node are different. The case with the most stable dominant interaction mode is the one when the voltage controlling converter is connected to the longest line, that is, the converter with the highest

DC current (and the lowest DC voltage, that is converter 5). The relevant data is given in Table 4.14.

Table 4.13: Line lengths, converter powers, voltages, currents and dominant interaction mode (case 4.5.5a)

Converter	L [km]	P_{ac} [MW]	v_{dc} [pu]	i_{dc} [pu]	λ	ζ
Conv 1	20	-203.86	1	1.0193	-	-
Conv 2	20	50	0.9794	0.2553	-4.88±j14.71	0.3149
Conv 3	20	60	0.9787	0.3065	-6.15±j14.23	0.3967
Conv 4	20	70	0.9781	0.3578	-7.43±j13.61	0.4792
Conv 5	20	80	0.9774	0.4092	-8.71±j12.86	0.5608

Table 4.14: Line lengths, converter powers, voltages, currents and dominant interaction mode (case 4.5.5b)

Converter	L [km]	P_{ac} [MW]	v_{dc} [pu]	i_{dc} [pu]	λ	ζ
Conv 1	20	-204,93	1	1.0247	-	-
Conv 2	20	50	0.9834	0.2542	-4.82±j14.21	0.3212
Conv 3	40	50	0.9801	0.2551	-4.91±j14.21	0.3266
Conv 4	60	50	0.9767	0.2560	-5.00±j14.21	0.3319
Conv 5	80	50	0.9734	0.2568	-5.09±j14.21	0.3372

In the third case, line lengths to all inverters are different again, and their powers are equal except for the power at converter 2, which is slightly higher (Table 4.15). Although the power of converter 2 is higher than the power at converter 5, the current at converter 2 is lower than the current at converter 5. For this reason, the dominant interaction mode when converter 2 is in charge of voltage control is less stable in comparison to the scenario when converter 5 is in charge of voltage control in the grid. The current of converter 2 is higher than the currents at converters 3 and 4, so general conclusions on the stability of the corresponding interaction modes without conducting a small-signal stability calculation could not be made.

The obtained conclusions cannot be generalized to grids in general polygon configuration. However, these considerations in a grid with voltage margin control could be helpful for the determination of droop coefficients in the droop control method to ensure the highest possible small-signal stability margin. If the sequence of converters, with respect to the stability of the

dominant interaction mode, is known (in voltage margin control) then the droop coefficients should follow that sequence to ensure the highest stability of the dominant interaction mode.

Table 4.15: Line lengths, converter powers, voltages, currents and dominant interaction mode (case 4.5.5c)

Converter	L [km]	P_{ac} [MW]	v_{dc} [pu]	i_{dc} [pu]	λ	ζ
Conv 1	20	-205.45	1	1.0273	-	-
Conv 2	20	50.5	0.9833	0.2568	-4.88±j14.19	0.3252
Conv 3	40	50	0.9801	0.2551	-4.91±j14.21	0.3266
Conv 4	60	50	0.9767	0.2560	-5.00±j14.21	0.3319
Conv 5	80	50	0.9733	0.2569	-5.09±j14.21	0.3372

Droop control is described with the following equation from Section 3.3.2:

$$p_{ac} - p_{ac}^{*} = k_{drp}\left(v_{dc} - v_{dc}^{*}\right), \tag{4.5}$$

where k_{drp} is the droop coefficient; and p_{ac}^{*} and v_{dc}^{*} are the reference active power and direct voltage of a certain converter. Converters with a higher value of droop coefficient participate more, and the ones with a lower value of droop coefficient participate less in voltage control of the grid. Voltage margin control can be considered as a marginal case of voltage droop control where one converter has an infinite droop coefficient (voltage controlling converter) and others have zero droop coefficients (power controlling converters). In a grid with droop control, as shown in [34], there are more interaction modes than in a grid with voltage margin control; however, only the mode with the lowest absolute value of the real part is assessed.

Voltage droop control is implemented in the grid from Fig. 4.18 with the parameters and operating point given in Table 4.13. Only the inverters participate in voltage droop control, while the rectifier is in constant active power mode. Values of four droop coefficients are chosen arbitrarily and mutually different. They are arranged amongst the four inverters (converters 2–5) in all possible ways (as seen in Table 4.16), along with the corresponding dominant interaction mode. When the order of droop coefficients is equal to the order of dominant interaction modes (when a certain converter is in charge of voltage control in the grid; the last column in Table 4.13), the dominant interaction mode in the grid with voltage droop control is the most stable (the first row in Table 4.16). In contrast, when the order of droop coefficients is exactly the opposite, the stability of the dominant interaction mode is the lowest (the last row in Table 4.16). The stability

of the dominant interaction mode is reflected precisely by the order of droop coefficients; therefore, for any replacement of two droop coefficients, the stability of the dominant interaction mode changes accordingly.

Table 4.16: Droop coefficients and dominant interaction modes (case 4.5.5d)

	$k_{drp,2}$	$k_{drp,3}$	$k_{drp,4}$	$k_{drp,5}$	λ	ζ
1.	0.1	0.5	1	2.5	-1.2486±j22.4053	0.0556
2.	0.1	0.5	2.5	1	-1.2476±j22.4114	0.0556
3.	0.1	1	0.5	2.5	-1.2395±j22.3679	0.0553
4.	0.1	1	2.5	0.5	-1.2382±j22.3761	0.0553
5.	0.1	2.5	0.5	1	-1.2102±j22.2620	0.0543
6.	0.1	2.5	1	0.5	-1.2098±j22.2641	0.0543
7.	0.5	0.1	1	2.5	-1.2413±j22.3735	0.0554
8.	0.5	0.1	2.5	1	-1.2404±j22.3796	0.0553
9.	0.5	1	0.1	2.5	-1.2248±j22.3061	0.0548
10.	0.5	1	2.5	0.1	-1.2233±j22.3158	0.0547
11.	0.5	2.5	0.1	1	-1.1953±j22.1999	0.0538
12.	0.5	2.5	1	0.1	-1.1947±j22.2036	0.0537
13.	1	0.1	0.5	2.5	-1.2228±j22.2962	0.0548
14.	1	0.1	2.5	0.5	-1.2215±j22.3044	0.0547
15.	1	0.5	0.1	2.5	-1.2154±j22.2662	0.0545
16.	1	0.5	2.5	0.1	-1.2139±j22.2760	0.0544
17.	1	2.5	0.1	0.5	-1.1760±j22.1243	0.0531
18.	1	2.5	0.5	0.1	-1.1757±j22.1259	0.0531
19.	2.5	0.1	0.5	1	-1.1631±j22.0703	0.0526
20.	2.5	0.1	1	0.5	-1.1628±j22.0724	0.0526
21.	2.5	0.5	0.1	1	-1.1555±j22.0401	0.0524
22.	2.5	0.5	1	0.1	-1.1550±j22.0437	0.0523
23.	2.5	1	0.1	0.5	-1.1456±j22.0043	0.0520
24.	2.5	1	0.5	0.1	-1.1454±j22.0059	0.0520

4.6. Conclusions

The main findings regarding the stability of interaction modes in VSC HVDC grid can be summarized as follows:

- a dominant interaction mode becomes more stable with the increase of power flow in the grid;
- the stability of a dominant interaction mode is greatly influenced by the power at the voltage controlling converter;
- a dominant interaction mode is more stable when loads at converters are symmetrical;
- a converter operating mode is reflected in the participation factors of interaction modes;
- a dominant interaction mode becomes less stable with the increase of the electrical distance between converters; and
- a dominant interaction mode becomes less stable with the increase of voltages in the grid.

If, for example, an MTDC grid connecting wind power plants is considered, it can be concluded that the small-signal stability of such a grid will be reduced when the electricity production is low. This is especially highlighted in grids with long cables, that is, in grids with relatively small power to distance ratio.

The findings in Section 4.5 assist to make an appropriate selection of voltage controlling converter with respect to small-signal stability in voltage margin control for two grid configurations: for radial (or star-connected) grids, and for grids in triangular configuration. The following conclusions are derived:

- if all line lengths are equal, the dominant interaction mode is the most stable when the voltage controlling inverter has the highest power;
- if all inverter powers are equal, the dominant interaction mode is the most stable when the voltage controlling inverter has the highest current; and
- the inverter current in combination with inverter power can more precisely define the stability of the dominant interaction mode.

The three above-mentioned statements can also be used in the voltage droop control. If the order of the droop coefficients is equal to the order of the stability of the dominant interaction modes (when a certain converter is in charge of voltage control in the margin control method), the

dominant interaction mode is the most stable and vice versa. This conclusion can serve as one of the selection criteria for droop coefficients when the voltage droop control method is employed.

5. COMPARATIVE ANALYSIS ON SMALL-SIGNAL STABILITY OF MULTI-INFEED VSC HVDC SYSTEM WITH DIFFERENT REACTIVE POWER CONTROL STRATEGIES

Parts of this chapter have been published in: G. Grdenić, M. Delimar and J. Beerten "Comparative Analysis on Small-Signal Stability of Multi-Infeed VSC HVDC System With Different Reactive Power Control Strategies," IEEE Access, vol. 7, 2019. [55]

VSC-based HVDC technology is used more and more in modern power systems. Consequently, in the AC network, an increasing number of converters are appearing in mutual electrical proximity, thus forming MI-HVDC systems. For VSC technology, several aspects of MI-HVDC system operation are less well understood compared to LCC HVDC systems. This chapter studies an MI system which consists of two VSC HVDC schemes based on MMCs interconnected with an AC line and connected to an external grid. The aim of the study is to identify the small-signal stability properties of such a system, thereby focusing on the impact of different outer control loops for reactive power and AC voltage regulation.

5.1. Introduction

Power systems are experiencing a growing use of HVDC transmission. Consequently, more and more converters are being located in electrical proximity to each other, forming MI-HVDC systems in AC grids. Since the main active components as seen from the AC system are power electronic devices, the investigation of their mutual interactions and their impact on the AC grid is largely based on methodologies which are also used in research regarding other FACTS devices, for example relative gain array or, more often, SSSA [56, 57].

Several decades of experience are behind us in the application of LCC HVDC systems. Their operation and control have been studied thoroughly, as have been MI-HVDC systems with these types of converters. MI systems containing both types of converters (VSC and LCC), usually called hybrid MI-HVDC systems, have also been presented in the literature. For example, an investigation of the impact of control system parameter settings on small-signal stability in a hybrid MI-HVDC system was conducted in [58], showing the significant importance of the PLL gains in VSC and LCC stations and of the AC voltage controller gains in VSC station. Researchers in [59] examined the effect of the AC system strength at the PCC of LCC (VSC) station and of the tie-line

length between the LCC and VSC inverter stations on the system's small-signal dynamics. In addition, an optimization of the control parameters was conducted to enhance the stability of this hybrid MI-HVDC system connected to relative weak AC grid.

However, much less attention has been dedicated to MI-HVDC systems consisting only of VSC converters. A power flow algorithm, including current and voltage limits of all converters, was developed in [60]. In [61] an eigenvalue sensitivity analysis was used for the implementation of wide-area control for swing modes damping. The influence of outer control loops on small-signal and transient stability in the Northern Scotland transmission model was investigated in [62] and further expanded in [63] by implementing and comparing different tuning approaches for AC voltage control. Valuable work, from the perspective of the study in this chapter, was presented in [64], in which the authors summarized the main factors affecting the small-signal stability of a VSC-based AC/DC power systems. Admittance-based stability assessment was performed in [65] to address control interactions and interferences between two grid-side VSC HVDC converters, thereby proving the necessity of considering higher-frequency dynamics of VSCs, as well as of the connected AC network. The importance of addressing higher-frequency control interactions has recently been demonstrated in a number of research studies including VSC HVDC converters. Stability analyses have indicated the impact of converter control and AC network parameters on the resonance occurrence, e.g. gains of outer loop controllers in [66], the feedforward filter, AC line length, and power transfer in [67].

What largely has been missing so far, is a systematic assessment of the influence of different converter outer control loops on the small-signal stability in MI-HVDC systems. The objective of this chapter is therefore to investigate the impact of different reactive power control strategies (reactive power control, AC voltage control, AC voltage droop control and remote bus voltage control) of two independent VSC-HVDC converters in a generic MI system. In addition, the sensitivity to a change in influencing system parameters is examined in order to provide more general insights. In contrast to [62] and [63], in which the influence of outer control loops on the low-frequency electromechanical modes was examined, the study in this chapter takes into account a wider frequency range. Differently from [65], small-signal properties are examined by modal and participation analysis in order to associate critical modes with corresponding state variables to gain better insights into the cause of possible instabilities.

This chapter is structured as follows. Section 5.2 describes the methodology used in the research, i.e. the modeling of converters and of the AC line, as well as the SSSA. Results and a discussion are presented in Section 5.3. The chapter ends with Section 5.4 in which the most important conclusions are summarized.

5.2. Methodology

5.2.1. Modeling approach

In Fig. 5.1, the configuration of the studied MI-HVDC system is shown, consisting of two VSC converters mutually interconnected with an AC line, with one of the converters connected to an external grid, represented as a voltage source behind its SCR impedance. This generic configuration represents a reduced AC/DC system model and has been used as well in a number of studies, e.g. in [63, 68]. It has been selected in this research to gain a clearer insight into the system's behavior in order to provide a useful guidance for more specific MI-HVDC systems. The AC network is modeled in a global DQ-reference frame, and each of the converters in their local dq-reference frame. The converter model used in this research is based on the simplified time-averaged representation of the MMC converter adjusted for SSSA presented in Section 3.2.2.

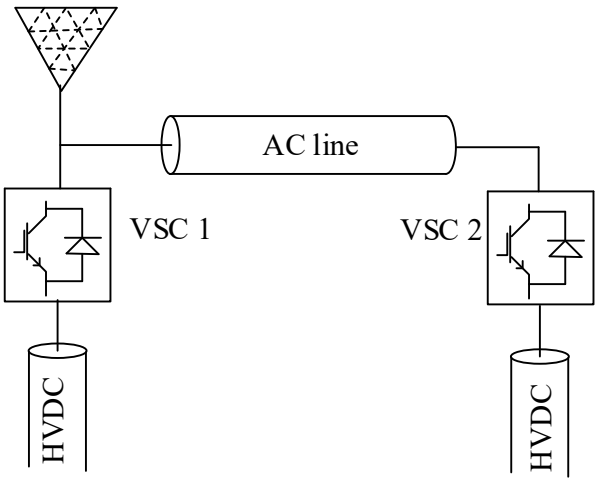

Figure 5.1: Configuration of the investigated MI-HVDC with two VSCs

The simplified representation of converter control structure is shown in Fig. 5.2. Differently from the representation in Fig. 3.6, instead of abc/dq transformations, DQ/dq transformations are employed. Therefore, AC variables modeled in common DQ-frame are denoted with $\underline{v_O}$ and $\underline{i_{CV}}$. Moreover, since the emphasis in this research is on converters' AC-side dynamics and on the impact of converters' outer/slower control loops, the HVDC lines are modeled by a current source

behind a capacitor C_{dc} that represents the equivalent capacitance of an HVDC cable. Consequently, the converter active power regulation also includes the DC voltage droop control for stability reasons [38].

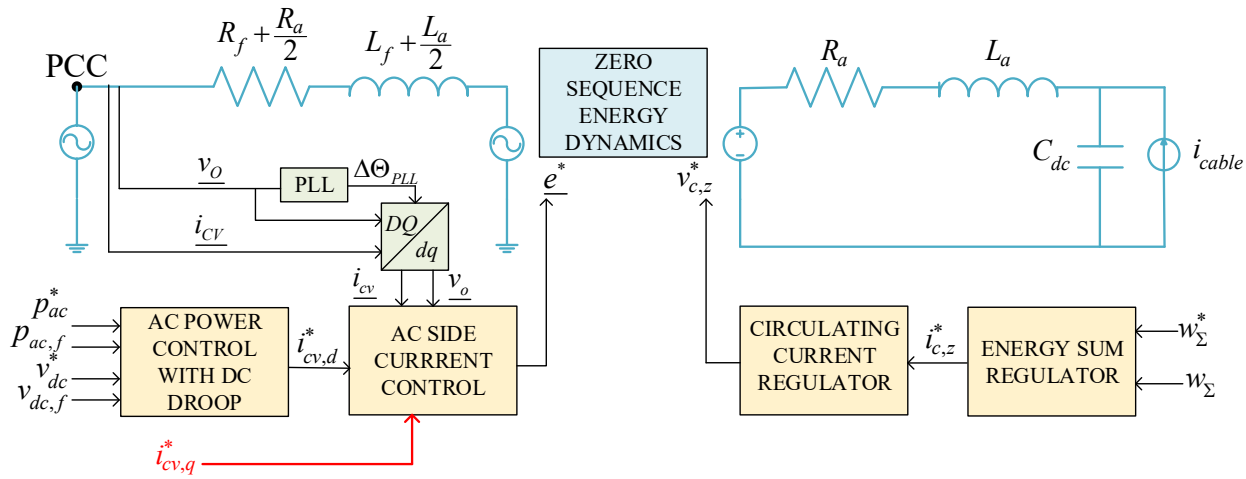

Figure 5.2: MMC control structure

The reference value of converter current q-component ($i^*_{cv,q}$) is determined by an outer control loop for regulating reactive power and/or AC voltage, depending on the control strategy applied: a) reactive power control, with q^*_{ac} and $q_{ac,f}$ respectively the reference and measured reactive powers in Fig. 5.3a), b) AC voltage control, with v^*_{ac} and $v_{ac,f}$ the reference and measured PCC voltages in Fig. 5.3b), c) AC voltage droop control, with k_{drp} the droop coefficient in Fig. 5.3c), or d) remote bus voltage control, with $v^*_{ac,rem}$ and $v_{ac,f,rem}$ the reference and measured remote bus AC voltages in Fig. 5.3d). In the last control configuration, that is remote bus voltage control, the converter regulates the voltage of a remote AC bus, instead of the PCC voltage. This remotely controlled AC bus has an arbitrary location along the AC transmission line. It is common in AC grids to control the voltage at a bus other than the terminal of a reactive power source [69]. Therefore, the objective here was to investigate the influence of this control configuration with other commonly applied reactive power control strategies for VSC HVDC converters. In the comparison of different reactive power controllers, equal PI coefficients have been used throughout this research.

The AC transmission line is modeled with two series connected π-sections with lumped parameters, shown in Fig. 5.4. Symbols R_{line}, L_{line} and C_{line} denote transmission line resistance,

inductance and capacitance respectively, with L the line length. The adequacy of π-section line model is validated by comparing its frequency characteristics with frequency-dependent line model in PSCAD for line parameters employed in the research and for 200 km long AC line. The two models coincide well for frequencies below 300 Hz (around 2000 rad/s) as can be observed from Figs. 5.5a and 5.5b. It has also been observed that for longer line lengths, a matching frequency is moving slightly, but not significantly to lower values. Using two π-sections for the modeling of an AC line is therefore justified for the frequencies within the bandwidths of interest (the converter's outer control) and for the observed AC line lengths. In further considerations, only modes within this bandwidth are taken into account for comparison purposes.

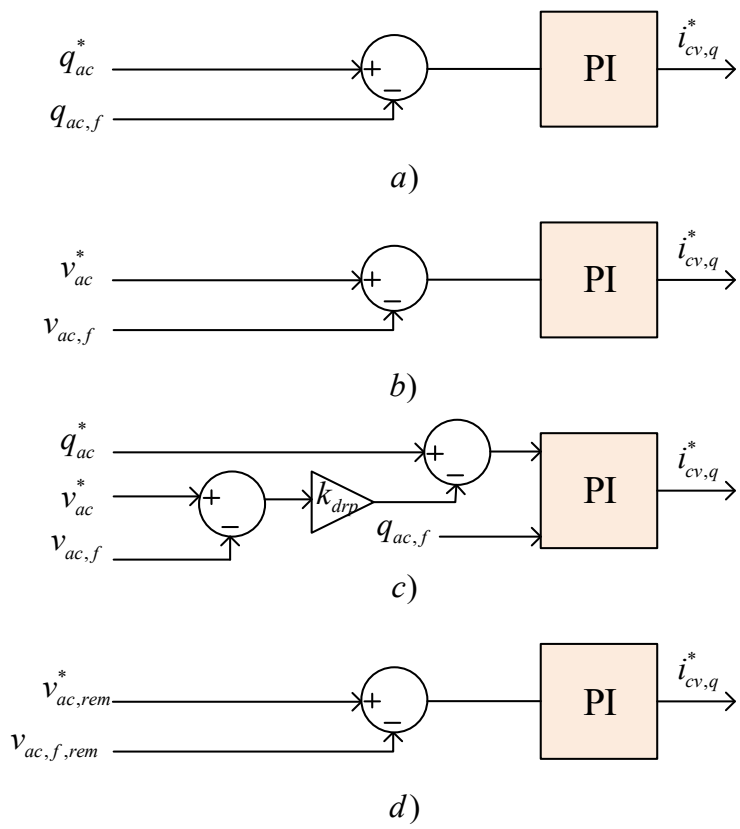

Figure 5.3: Different reactive power outer control loops

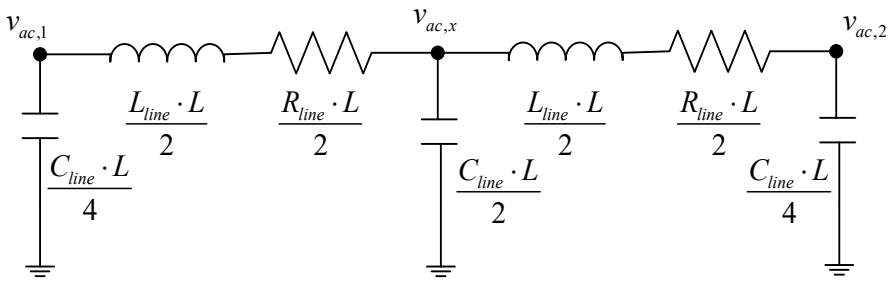

Figure 5.4: AC transmission line model

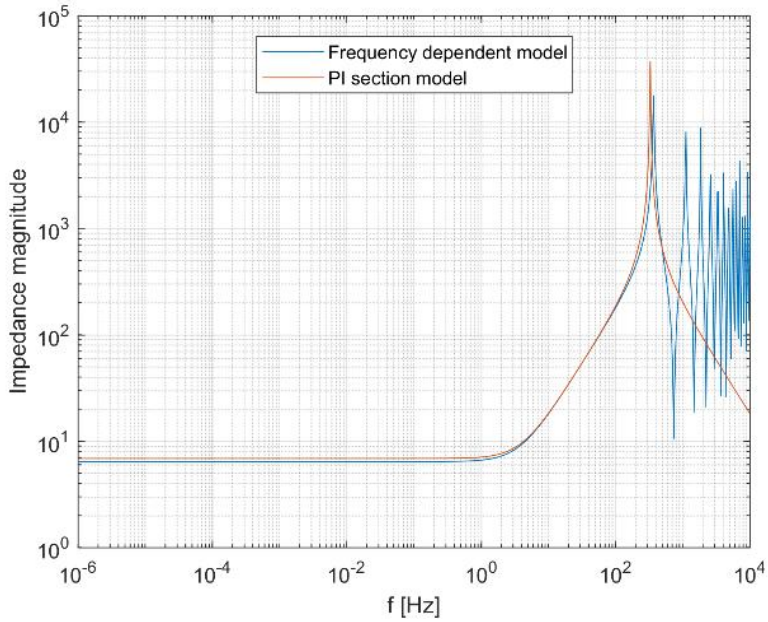

a)

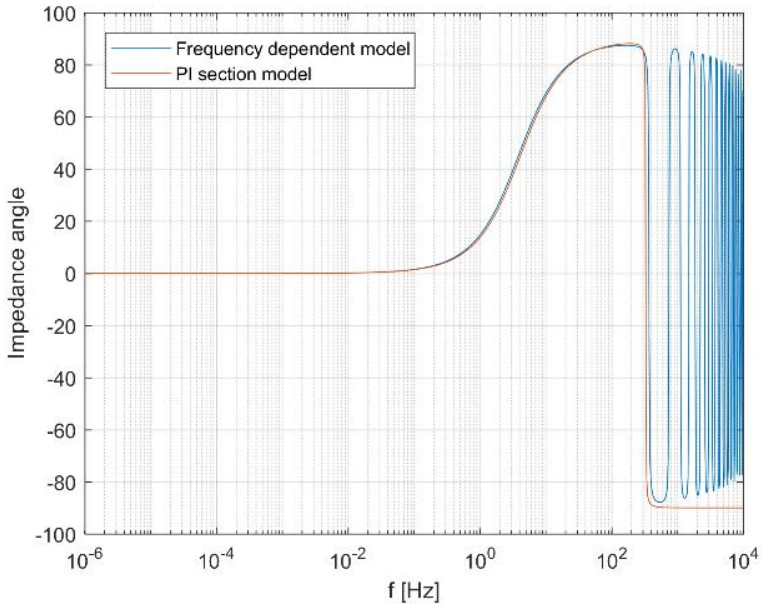

b)

Figure 5.5: Frequency characteristics of a π-section line model and a frequency-dependent line model: a) impedance magnitude; b) impedance angle

5.2.2. Small-signal stability analysis

The described differential algebraic model of the system shown in Fig. 5.1 has been built and linearized using Matlab/Simulink for a 150 km long AC line. Physical parameters and control parameters for the converters have been taken from [37]. The AC grid parameters are provided in

Appendix B. The external grid voltage has been set to 1.05 pu, whilst the power orders of both converters are equal to the nominal power. Both converters are operating as rectifiers with no reactive power injection into the AC grid. The linearized state-space representation of the system is established in the form of:

$$\Delta\dot{\mathbf{x}} = \mathbf{A}\cdot\Delta\mathbf{x} + \mathbf{B}\cdot\Delta\mathbf{u}\,, \tag{5.1}$$

with $\mathbf{x}$ and $\mathbf{u}$ vectors of the system's state and input variables, and $\mathbf{A}$ and $\mathbf{B}$ system's state-space and input matrices. The linearization of the system equations around the operating point has been carried out automatically by using the embedded *Linear Analysis Tool* in Matlab/Simulink. The system's state variables vector is described by (5.2) and consists of 52 state variables: 22 for each converter and 8 additional state variables for the AC line currents and voltages ($i_{LINE,D,1}$, $i_{LINE,Q,1}$, $i_{LINE,D,2}$, $i_{LINE,Q,2}$, $v_{ac,x,D}$, $v_{ac,x,Q}$) and currents to the external grid ($i_{O,D}$, $i_{O,Q}$).

$$\mathbf{x} = \begin{bmatrix} i_{cv,d,i}\ i_{cv,q,i}\ v_{o,d,i}\ v_{o,q,i}\ v_{dc,i}\ \gamma_{d,i}\ \gamma_{q,i}\ \rho_{d,i}\ \rho_{q,i}\ \varepsilon_{PLL,i}\ \Delta\Theta_{PLL,i} \\ p_{ac,f,i}\ v_{dc,f,i}\ q_{ac,f,i}\ (v_{ac,f,i})\ v_{ICC,d,i}\ v_{ICC,q,i}\ v_{PLL,d,i}\ v_{PLL,q,i} \\ w_{\Sigma,i}\ i_{c,z,i}\ \kappa_{\Sigma,i}\ \zeta_{z,i} \\ i_{LINE,D,i}\ i_{LINE,Q,i}\ v_{ac,x,D}\ v_{ac,x,Q}\ i_{O,D}\ i_{O,Q} \end{bmatrix} \quad i = 1,2 \tag{5.2}$$

When AC voltage control is used instead of reactive power control, the measured PCC voltage $v_{ac,f}$ is used instead of the measured reactive power $q_{ac,f}$. In case the AC voltage droop control is applied, the number of state variables grows with one more. The system eigenvalues are calculated from the state-space matrix $\mathbf{A}$ in order to assess the small-signal stability properties of the system. The participation of different subsystems p_α is calculated according to the definition from chapter 3.1.2:

$$p_\alpha = \sum p_{ki} \quad | \, x_k \in \alpha \tag{5.3}$$

where p_{ki} is the normalized participation factor of state variable x_k in eigenvalue λ_i, and α the set of state variables describing one of the four subsystems: converter 1, converter 2, AC line and external grid.

5.3. Results and discussion

5.3.1. Comparison of basic control configurations

Four different reactive power control methods have been employed and compared from the perspective of small-signal stability of the whole MI-HVDC system:

1. Reactive power control in both converters (Q1-Q2)
2. AC voltage control in converter 1 and reactive power control in converter 2 (Vac1-Q2)
3. Reactive power control in converter 1 and AC voltage control in converter 2 (Q1-Vac2)
4. AC voltage control in both converters (Vac1-Vac2)

The system oscillatory modes slower than 1500 rad/s and with real part larger than -1200 for four different control methods are presented in Fig. 5.6. Seven different modes related to the same state variables were traced for different configurations. These modes and their corresponding dominant participating state variables are listed in Table 5.1.

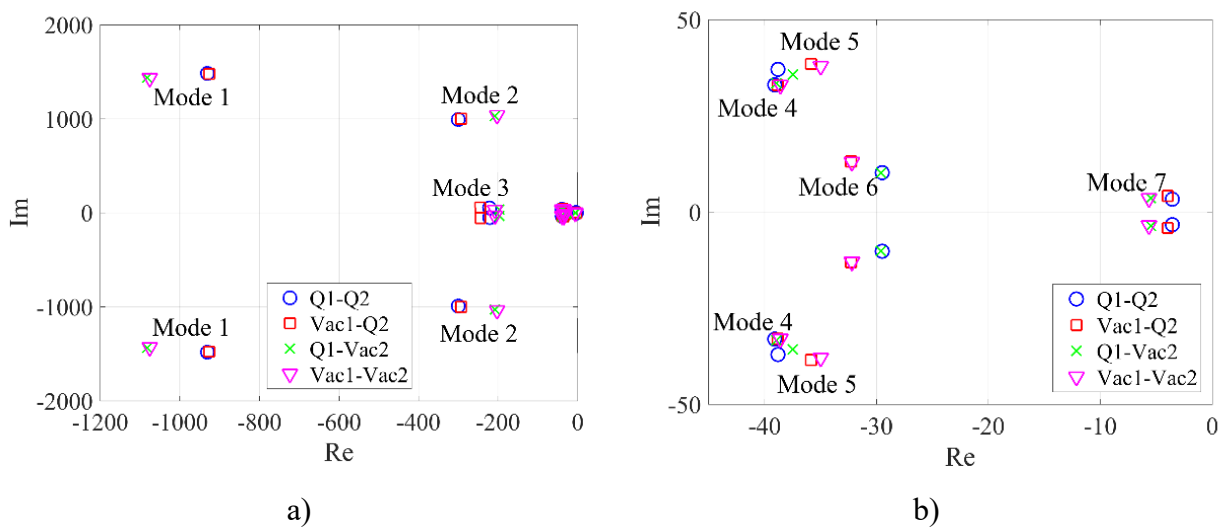

Figure 5.6: System oscillatory modes for different reactive power control methods: a) all; b) zoom-in

Mode 1 is mostly related to the q-component of the filtered and feedforward PCC voltage at converter 2 ($v_{ICC,q,2}$) and to the q-component of converter 2 current ($i_{cv,q,2}$). Mode 2 is related to the measured active power of converter 2 ($p_{ac,f,2}$) and to the d-component of the filtered feedforward PCC voltage at converter 2 ($v_{ICC,d,2}$). Mode 3 mostly depends on the reactive power or AC voltage measurement from converter 2 ($q_{ac,f,2}$ or $v_{ac,f,2}$) and in the cases when the reactive

power control is applied in converter 1, mode 3 also depends on the measured reactive power from converter 1 ($q_{ac,f,1}$). Modes 4 and 5 are related to the active power integrator state (ρ_p) and total zero-sequence energy sum dynamics (w_Σ) of respectively converter 1 and 2; while, modes 6 and 7 are related to the PLL state variables (ε_{PLL}, $\Delta\Theta_{PLL}$) of respectively converters 1 and 2.

Table 5.1: Dominant participating state variables in system oscillatory modes

Mode	State variables
1	$v_{ICC,q,2}$, $i_{cv,q,2}$
2	$p_{ac,f,2}$, $v_{ICC,d,2}$
3	$q_{ac,f,2}$, ($v_{ac,f,2}$), $v_{PLL,q,2}$, $q_{ac,f,1}$, $v_{PLL,q,1}$
4	$\rho_{p,1}$, $w_{\Sigma,1}$, $\zeta_{z,1}$
5	$\rho_{p,2}$, $w_{\Sigma,2}$, $\zeta_{z,2}$
6	$\varepsilon_{PLL,1}$, $\Delta\Theta_{PLL,1}$
7	$\varepsilon_{PLL,2}$, $\Delta\Theta_{PLL,2}$

The most noticeable difference observed in the damping ratios of these system modes (Fig. 5.7) is that the least damped mode (that is, mode 2) becomes less damped when AC voltage control is employed in the remote converter 2 (Q1-Vac2 and Vac1-Vac2 methods). Modes 5 and 6 become less damped when voltage control is employed in converter 1 and mode 7 becomes more damped when voltage control is employed in converter 2. The behavior of mode 2 is also clear from the time-domain simulation in Fig. 5.8, which shows the active power response of converter 2, following the active power reference step. The response overshoot is more pronounced when voltage control is applied in converter 2 (the converter connected to the PCC with a lower SCR), while the type of control applied in converter 1 (converter with the higher SCR) has a negligible impact on this response.

The reasoning for this behavior can be found by considering the q-component reference value of the converter 2 current ($i^*_{cv,q,2}$), which is set by the outer reactive power or by the AC voltage control loop. When reactive power control is employed in converter 2, the q-component reference current remains unaltered, i.e. $i^*_{cv,q,2} = \text{const}$, when changing the converter's active power.

However, when AC voltage control is employed in converter 2, the q-component reference current changes, i.e. $i^*_{cv,q,2} \neq \text{const}$, when changing the converter's active power due to the effect the active power order change has on the voltage. The change of this reference value ($\Delta i^*_{cv,q,2}$) is more pronounced in a weak AC system because the AC voltage change (Δv_{ac}) is larger for the same amount of active power change (Δp_{ac}) compared to the situation in a strong AC system. The rate of change of $i^*_{cv,q,2}$ can be limited by decreasing the speed of the outer control loop when AC voltage control is employed.

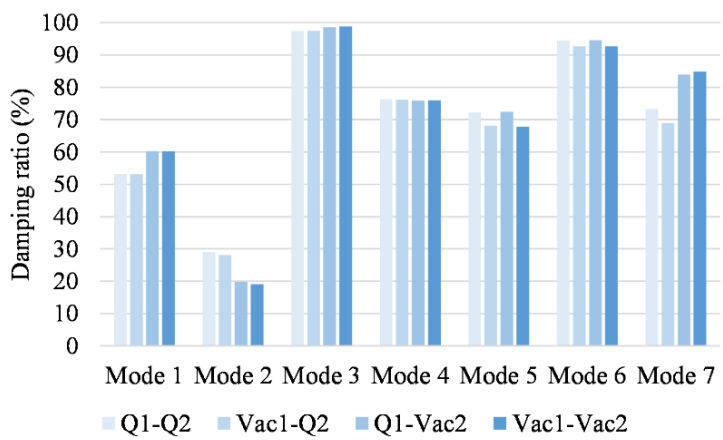

Figure 5.7: Damping ratios of system modes for different reactive power control methods

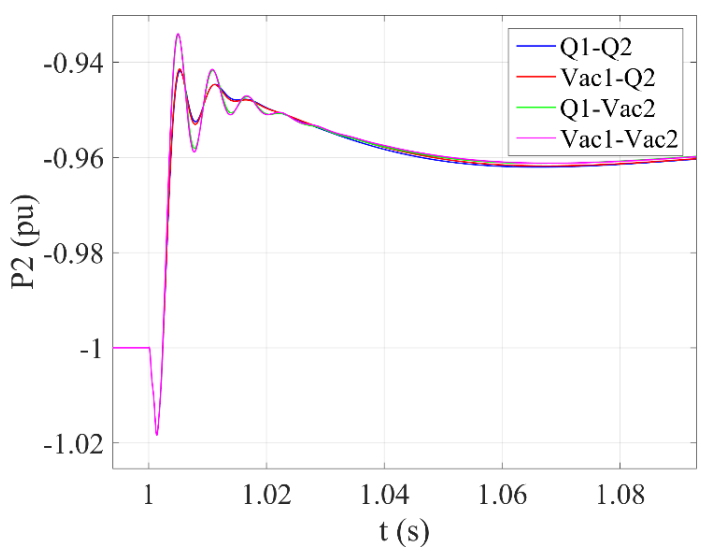

Figure 5.8: Converter 2 active power response for different reactive power control methods

Fig. 5.9 shows the participation of the four different subsystems (converter 1, converter 2, ac line and external grid) in the seven observed modes as defined in equation (5.3). The most significant difference occurs in mode 3 linked to the reactive power or AC voltage measurement from converter 2, which becomes almost entirely decoupled from the converter 1 state variables when voltage control is applied in converter 1. Voltage control in converter 1 also has a positive decoupling impact on the PLL mode of converter 1 (mode 6), but much less pronounced. On the contrary, it has a negative coupling effect on modes 4 and 5 and on the converter 2 PLL mode (mode 7), especially when Vac1-Q2 control is applied. In the following two subsections, the influence of the AC line length and of the active power on the AC transmission line are examined in a system with the Vac1-Vac2 control configuration.

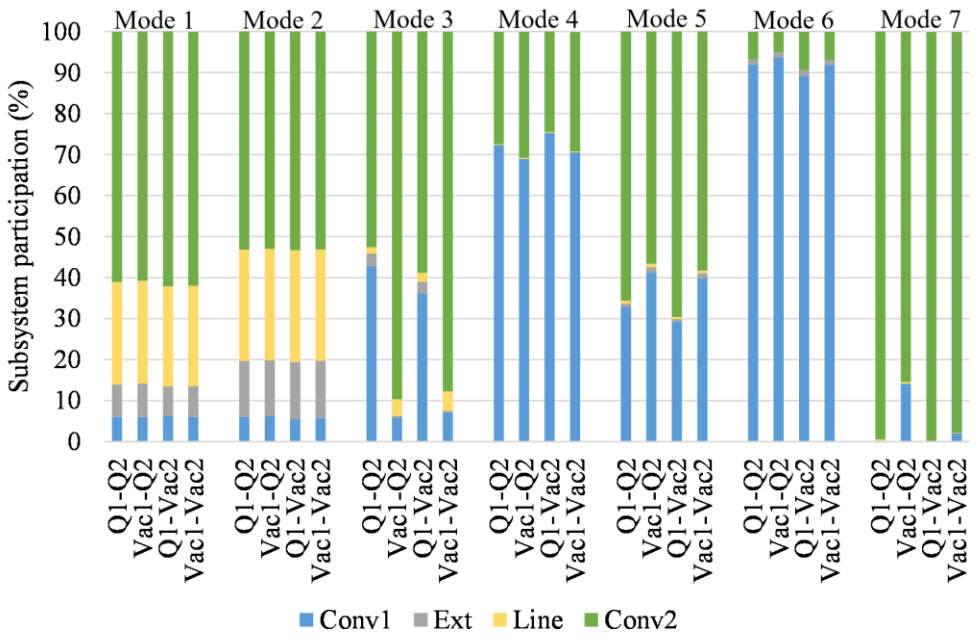

Figure 5.9: Participation contribution of different subsystems for different reactive power control methods

AC line length variation

By varying the AC line length, the SCR of converter 1 largely remains unaltered while the SCR for converter 2 changes. The effect of increasing the AC line length on the damping ratios of system modes is shown in Fig. 5.10, for four different lengths: 100 km, 125 km, 150 km and 175 km. Almost all modes experience decreased damping for increased line lengths. The change is the most pronounced in modes 1 and 2 linked respectively to the converter 2 filtered feedforward AC voltage and converter 2 active power measurement.

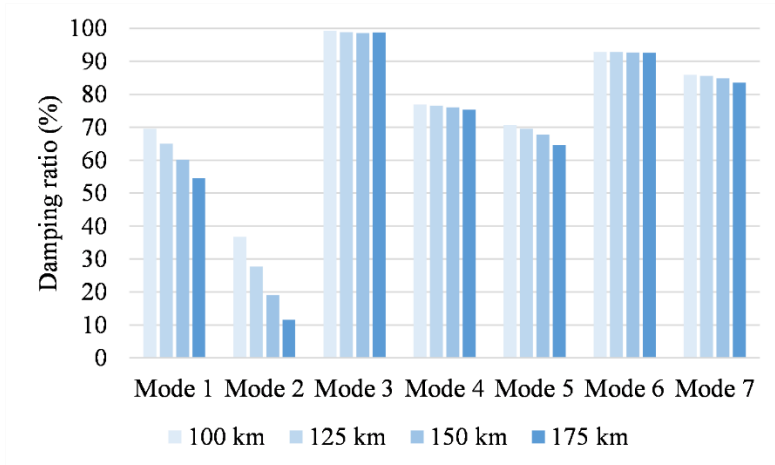

Figure 5.10: Damping ratios of system modes for different AC line lengths

This behavior is also apparent in the time-domain simulations for a reference active power step in converter 2 for two different lengths (150 km and 175 km) and for the two different control configurations (Vac1-Q2 and Vac1-Vac2) in Fig. 5.11. The response overshoot is more pronounced in case of a longer line since the SCR of converter 2 is decreased with increasing AC line length. This observation holds for both control configurations. When considering the participation of the different subsystems (Fig. 5.12), the contribution of the line increases in modes 1 and 2 with the increased line length. Modes 4 and 5, linked to the active power PI controller's integrator and total zero-sequence energy sum of respectively converter 1 and 2, become more decoupled.

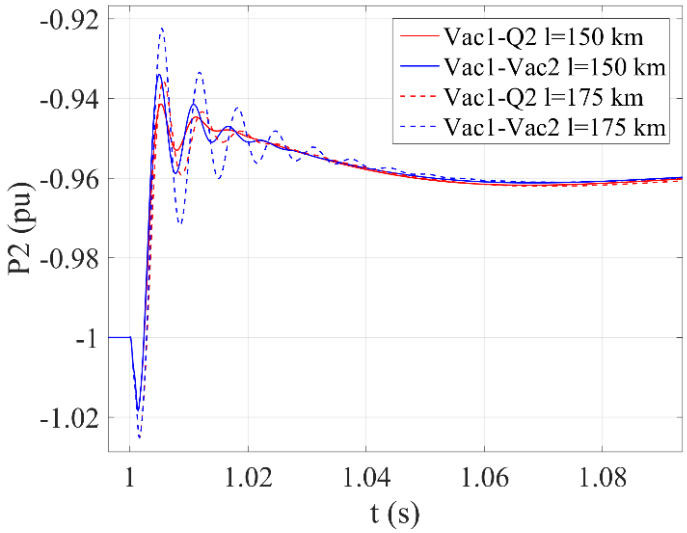

Figure 5.11: Converter 2 active power response for different AC line lengths and reactive power configurations

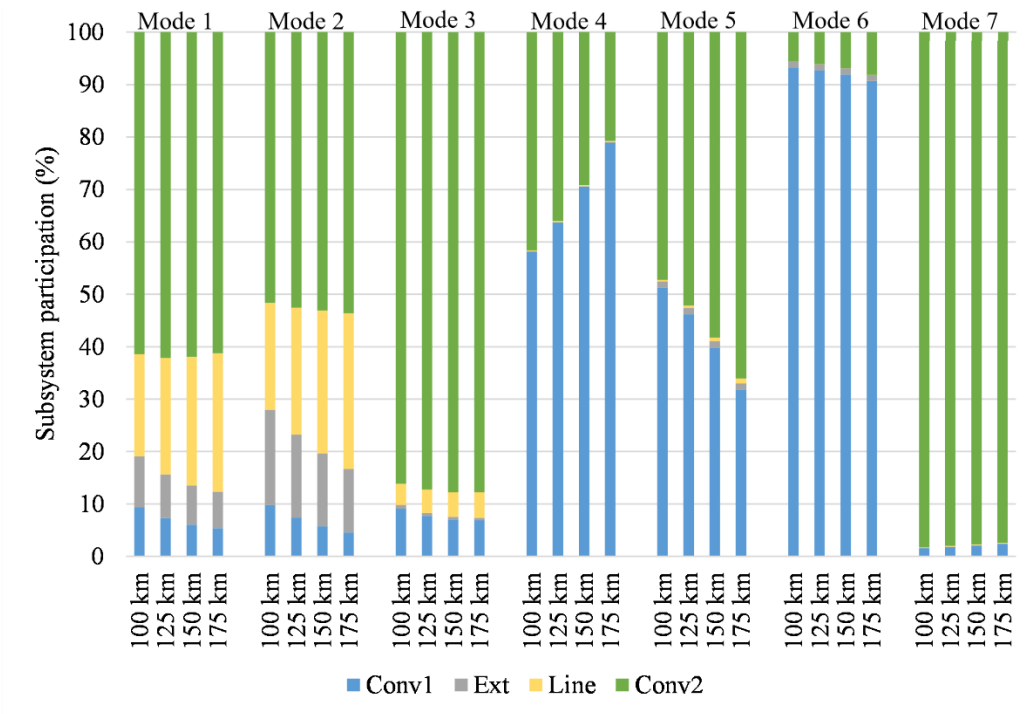

Figure 5.12: Participation contribution of different subsystems for different AC line lengths

AC line power flow variation

In this section, the active power of converter 2 is varied. Damping ratios of the observed modes are shown in Fig. 5.13 for four different converter active powers: 1000 MW, 750 MW, 500 MW and 250 MW. The largest change can be observed in the mode related to the active power control of converter 2 (mode 5), which becomes less damped in the case of low active power. On the contrary, the least damped mode (mode 2) becomes more damped in the lightly loaded system.

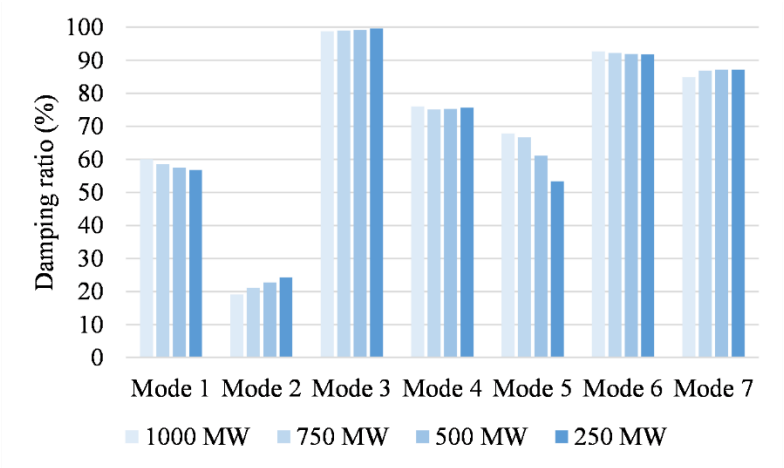

Figure 5.13: Damping ratios of system modes for different active powers of converter 2

Lower converter 2 active power, and consequently lower AC line active power flow, generally has a positive decoupling impact on converters' control as can be observed in Fig. 5.14: higher participation of converter 1 state variables in mode 4 (converter 1 active power mode) and of converter 2 state variables in mode 5 (converter 2 active power mode). Similar, but far less pronounced trends are observed in the converters' PLL modes (modes 6 and 7).

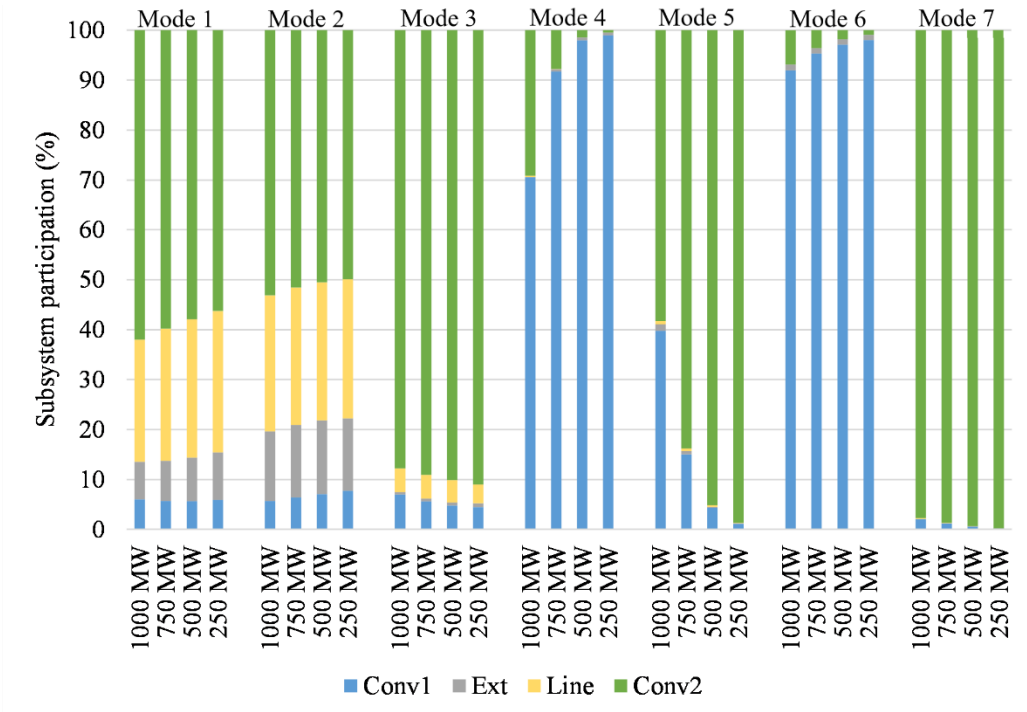

Figure 5.14: Participation contribution of different subsystems for different active powers of converter 2

5.3.2. AC voltage droop control

AC voltage droop control is first been implemented in converter 1 while AC voltage control is employed in converter 2. The parameters of the PI regulators have remained the same compared to the previous subsection. The maximum achievable droop coefficient equals $k_{drp,1} = 43.3$ before the system becomes unstable. In contrast, the maximum achievable droop coefficient when droop control is employed in converter 2 (and voltage control in converter 1) is only equal to $k_{drp,2} = 3.5$. The influence of the converter 2 droop coefficient on the observed system modes is demonstrated in Fig. 5.15. By increasing the value of the droop coefficient, mode 2—related to the filtered feedforward AC voltage and active power measurement of converter 2—becomes insufficiently damped while the damping ratios of other modes either improve or remain unaltered.

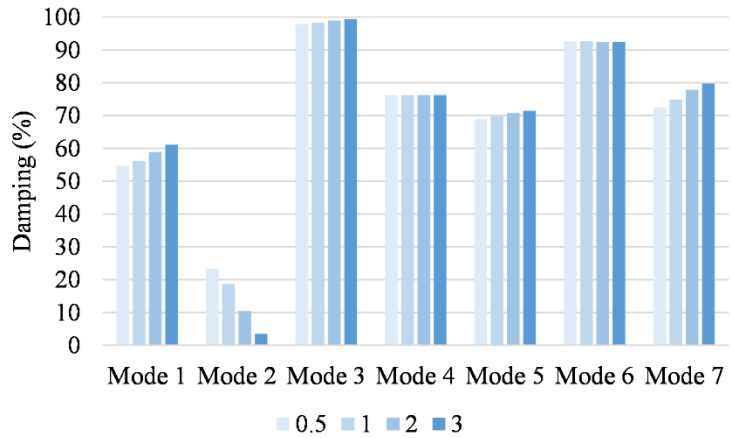

Figure 5.15: Damping ratios of system modes for different AC voltage droop coefficients of converter 2

The normalized participation factors of state variables higher than 5% are shown in Fig. 5.16 for the case when mode 2 is approaching the stability margin ($k_{drp,2} = 3.5$). It can be observed that for this specific case, besides the active power measurement ($p_{ac,f,2}$) and the filtered PCC voltage used in the ICC ($v_{ICC,d,2}$), mode 2 has an even higher participation from the AC voltage measurement used in the outer controller ($v_{ac,f,2}$) and from the d-components of respectively line, external grid and converter 2 currents ($i_{LINE,D,1}$, $i_{O,D}$ and $i_{cv,d,2}$).

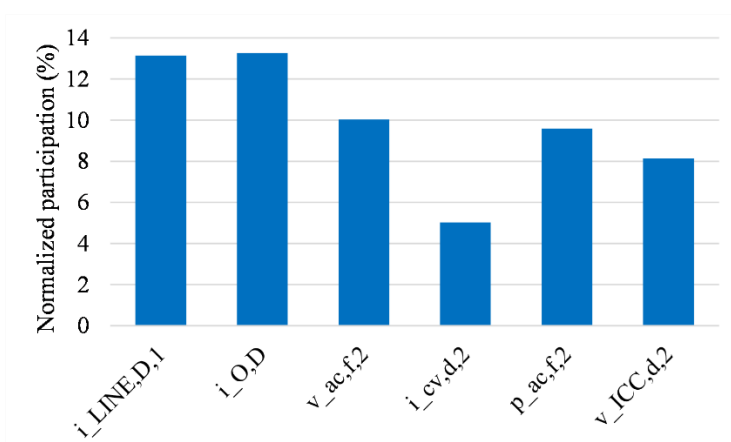

Figure 5.16: Participation factor analysis of mode 2 ($k_{drp,2} = 3.5$)

The damping of mode 2 is further investigated for two different AC line models: the dynamic model used throughout this chapter and a steady-state representation—neglecting current and voltage dynamics. Results are presented in Fig. 5.17 for two different line lengths. It can be

observed that with the steady-state representation of the transmission line, the stability of mode 2 is significantly overestimated for increased droop coefficients. Higher droop coefficients, as can be observed from Fig. 5.17, are achievable with shorter AC line, i.e. with a resulting higher SCR at the PCC of the remote converter.

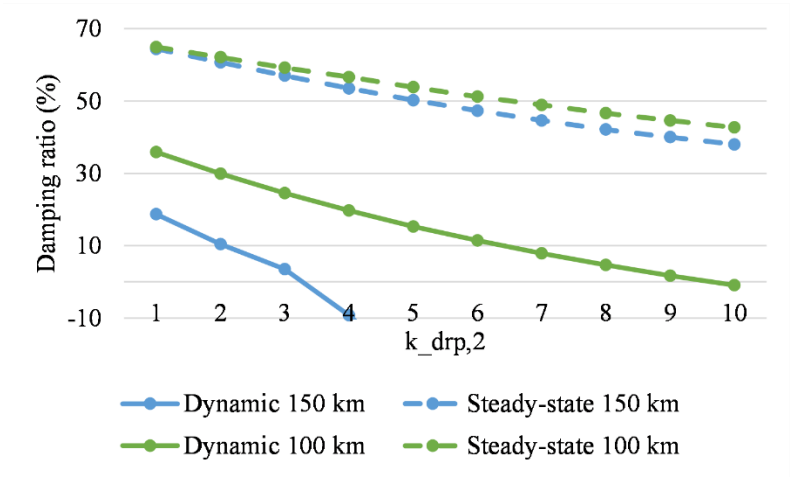

Figure 5.17: Comparison of mode 2 damping ratios for dynamic and steady-state transmission line representation

5.3.3. Remote bus voltage control

In this control configuration, the measurements of the AC voltage employed in the outer control of converter 2 are taken at different locations along the AC line: (i) at the PCC, (ii) at 75% of the line length (referred to as remote location 1, or Rem1), (iii) at 50% of the line length (Rem 2) and (iv) at 25% of the line length (Rem 3). For the implementation of these control configurations, adjustments were made in the transmission line model from Fig. 5.4 and voltage measurements were taken at the connection of the two cascaded π-sections. It was verified that varying the lengths of the two π-sections only has an influence on the very high-frequency LC oscillations, well above the control bandwidth under consideration. Additionally, in the feedback remote bus voltage signals, time-delays equal to 50 ms have been added to model the communication delay. Equal delays have been employed for different distances because of comparison purposes, and moreover, the propagation delay through the communication medium consists only a smaller part of the overall delay when considering that the speed at which the data is sent through the communication medium is very high (0.6c to c with c being the speed of light) [70].

Fig. 5.18 illustrates the damping ratios of the previously observed modes and of the new low-frequency mode (denoted with mode 8, $f \approx 6\ \text{Hz}$) originated by the linearization of the time-delay block by using the 2nd order of Padé approximation. The most significant change by varying the location of voltage measurement occurs in new mode 8 which is mostly related to state-variables of the time-delay block. By increasing the distance, this mode becomes more damped. The change in other modes is less pronounced. Modes 2 and 5 become more damped, while modes 1 and 7 become less damped with an increasing distance of the location of the voltage measurement.

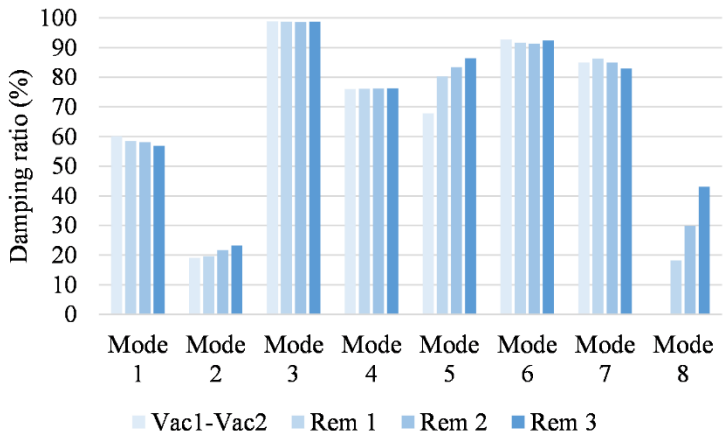

Figure 5.18: Damping ratios of system modes for different location of AC voltage measurements

5.4. Conclusion

The small-signal stability properties of the following reactive power control methods have been compared in this chapter for a MI-HVDC system composed of two MMC-based converters: reactive power, AC voltage control, AC voltage droop control and remote bus voltage control. The system response is significantly affected by the type of control employed in the converter with a lower SCR, rather than the one with a higher SCR. Furthermore, AC voltage control in the converter with a lower SCR improved the relative stability of some system modes, but it also aggravated the stability of the least damped mode.

Increasing the AC line length was generally found to have a negative impact on the system stability, while low active power flow on the connecting line had a positive impact on some modes and a negative impact on others. Participation factor analysis of different subsystems showed that low active power flow on the transmission line and increasing the AC line length generally have a positive decoupling effect on the converters' active power and zero-sequence energy sum control.

Remote bus voltage control introduces new low-frequency mode originating from the linearization of the time-delay block. With an increasing distance of the location of AC voltage measurements, this mode becomes more damped while the influence on other modes is less pronounced.

Larger droop coefficients were possible when AC voltage droop control was employed in the converter connected at the bus with a higher SCR. It has been shown that steady-state representation of the AC line is overestimating small-signal stability of the system. Thus, the importance of AC line/grid modeling, as well as converter modeling, within an appropriate bandwidth was demonstrated. The observations for the generic test case presented in this study can serve as a valuable guidance for other more specific topologies.

6. ASSESSMENT OF AC NETWORK MODELING IMPACT ON SMALL-SIGNAL STABILITY OF AC SYSTEMS WITH VSC HVDC CONVERTERS

The increasing number of FACTS devices and HVDC systems is changing perspectives on small-signal stability in AC grids, as traditional steady-state modeling does not allow representing higher-frequency interactions between synchronous generators, AC grid and power electronic-based devices. Since dynamically modeling all grid components typically result in an overly complex system model with a very high order, hybrid network models have been put forward as a compromise to increase the scope of the study, whilst keeping the overall system model order manageable. They do so by combining grid dynamics in the vicinity of the power electronic devices with steady-state assumptions for the rest of the network. This chapter examines the impact of converter and grid parameters on the outcome of the stability analysis through comparative examples of a double MI-HVDC system and a single and double HVDC infeed in the IEEE 39 bus system and by using either steady-state or dynamic line models. Doing so, it determines the most relevant parameters to the boundary selection between a dynamic and a static AC grid model in hybrid network models.

6.1. Introduction

In power system studies, SSSA has traditionally been used to identify low-damped electromechanical oscillations between synchronous generators [12]. Since these oscillations occur at low frequencies, it has been commonplace to model the AC network by means of algebraic or steady-state equations for the analysis, thereby neglecting faster electromagnetic transients. With more and more power electronics-based equipment entering the transmission system, the frequency range over which dynamic interactions occur is increasing, and consequently the conventional view on small-signal stability in power system is changing accordingly. In order to be able to identify and mitigate problems w.r.t. these faster interactions between synchronous generators, AC grid and power electronic-based devices, SSSA should also be able to capture these phenomena. In this sense, the steady-state AC network model no longer suffices and dynamic line models are needed.

Researchers in [71] showed that dynamic based AC line modeling is necessary for accurately assessing the system's small signal stability for the case of two LCC HVDC lines in a MI-HVDC system. Moreover, the comparative analysis in [72] on a point-to-point VSC link

suggests that steady-state modeling of the Thevenin AC network equivalent cannot always reflect the actual stability of the system, even when mainly focusing on slower system modes. Reflecting on the observations from [71] and [72], the steady-state network modeling can give rise to misleading conclusions about the system stability margin. As a result, dynamic modeling of the AC network has found its way into a number of recent small-signal studies. Usually, however, these are small AC systems, like island systems [73] or systems where the external AC network is represented with Thevenin equivalents, as has been done, for example, in [34, 49, 74, 75]. Some researchers have started using dynamic modeling of the AC network also in larger grids, as has been carried out in [76-78].

Dynamic modeling of the entire AC network, however, implies a significant increase in the number of state variables of the system model, and consequently of the size of the state-space matrix of the linearized system, necessary for determining the system's eigenvalues. As long as the size of the AC grid is small this does not produce difficulties, but in large multi-machine AC networks, dynamic modeling of all static elements (transmission lines, power transformers, capacitors, and inductors) can lead to very large state-space matrices from which it can become difficult to calculate the eigenvalues [79]. Moreover, it is not clear whether dynamically representing all elements is strictly necessary for an accurate assessment of small-signal stability of the system.

One solution to this problem is to model the AC network dynamically only in the vicinity of power electronic-based devices and keep the rest of the network modeled using algebraic steady-state equations. This approach has been proposed in [13], resulting in a hybrid network model for SSSA of power systems. However, the boundary selection between these two approaches, that is, static and dynamic AC network modeling has not been examined in more detail. Similar modeling partition can also be found in some other work which is not exclusively related to SSSA. For example, in [80], a platform for analyzing power systems has been developed in which the entire power system is modeled as a multivariable feedback control system (FCS) and divided similarly into dynamic and static parts. The developed FCS model has been verified on the IEEE 9 bus test system with HVDC links (both LCC and VSC), though, the selection of the boundary between static and dynamic parts has not been discussed in the paper. However, defining the boundary between dynamically and statically modeled sections of an AC grid is not an unambiguous problem

with a straightforward solution which holds in all possible cases. The primary goal of this research is therefore to systematically investigate the impact of relevant converter and grid parameters to this boundary selection. First, the influence that AC line modeling has on system small-signal stability properties is demonstrated on the generic example of a VSC-based MI-HVDC system. Afterward, converter and grid parameters have been assessed in order to identify the most relevant ones to the boundary selection between statically and dynamically modeled parts of an AC grid. This has been carried out by the comparison procedure based on SSSA in the case of a single and double VSC HVDC infeed in a relatively larger AC network.

The rest of the chapter is organized as follows. Section 6.2 describes the assembling of steady-state, dynamic and hybrid network models and establishes the comparison procedure of different system models. Section 6.3 introduces the case of a generic VSC-based MI-HVDC system and in Section 6.4 the assessment of converter and grid parameters has been carried out in the IEEE 39 bus grid with VSC HVDC converters. The main findings are summarized in the conclusion section.

6.2. Methodology

6.2.1. Modeling

The studied systems include three types of network elements: VSCs, synchronous generators and AC lines. For the modeling of the VSC, an ideal lossless MMC model with simplified internal dynamics, which is described in Section 3.2.2, is used. It is adjusted from [38] and described by the 20th order system with its parameters taken from [37] and can also be found in Appendix B. Generally, the model can be described by a set of differential and algebraic equations:

$$\begin{aligned} \dot{\mathbf{x}}_{\mathbf{vsc}} &= \mathbf{f}(\mathbf{x}_{\mathbf{vsc}}, \mathbf{u}_{\mathbf{vsc}}, \underline{v_{vsc}}) \\ \underline{i_{vsc}} &= \mathbf{g}(\mathbf{x}_{\mathbf{vsc}}, \mathbf{u}_{\mathbf{vsc}}, \underline{v_{vsc}}) \end{aligned}, \tag{6.1}$$

where $\mathbf{x}_{\mathbf{vsc}}$ and $\mathbf{u}_{\mathbf{vsc}}$ are the converter state and input vectors, $\underline{v_{vsc}}$ is the voltage at the PCC and $\underline{i_{vsc}}$ is the corresponding injection current expressed in dq-reference frame.

For the synchronous generator modeling, the 6th order model [81] is used together with the AC4A excitation system model [82]. Differential and algebraic equations of the models can be

found in Appendix C. It can be also represented succinctly with the following set of differential and algebraic equations:

$$\begin{aligned} \dot{\mathbf{x}}_{\mathbf{gen}} &= \mathbf{f}(\mathbf{x}_{\mathbf{gen}}, \mathbf{u}_{\mathbf{gen}}, \underline{i_{gen}}) \\ \underline{v_{gen}} &= \mathbf{g}(\mathbf{x}_{\mathbf{gen}}, \mathbf{u}_{\mathbf{gen}}, \underline{i_{gen}}) \end{aligned}, \tag{6.2}$$

where $\mathbf{x}_{\mathbf{gen}}$ and $\mathbf{u}_{\mathbf{gen}}$ are the generator state and input vectors, $\underline{v_{gen}}$ is the voltage at the connection point and $\underline{i_{gen}}$ is the corresponding injection current expressed in qd-reference frame.

The AC network is modeled in a global DQ-reference system, synchronous generators in their local qd-reference systems and converters in their local dq-reference systems. Corresponding transformations have been applied in order to integrate the individual elements into an AC/DC system. Depending on how the AC network is modeled, different overall system models have been established.

Steady-state network model

In this system model, the dynamics of the AC grid, that is, AC lines and transformers, are neglected. The AC grid is represented by the set of algebraic (nodal) equations using a standard admittance matrix assembled with network parameters evaluated at the nominal frequency:

$$\mathbf{i}_{\mathbf{bus}} = \mathbf{Y}_{\mathbf{bus}} \times \mathbf{v}_{\mathbf{bus}}, \tag{6.3}$$

where $\mathbf{i}_{\mathbf{bus}}$ and $\mathbf{v}_{\mathbf{bus}}$ are the vectors of injection currents and bus voltages, respectively. The converter and generator models described by (6.1) and (6.2) are combined with the admittance matrix as described in [12]. Loads are modeled as constant admittances and included in the admittance matrix.

Dynamic network model

In the dynamic network model, the π line model has been employed. The adequacy of the π line model has been validated for the observed line lengths and for the frequencies within the bandwidth of interest (the converter's control). The dynamics of the line currents $\underline{i_{LINE}} = i_{LINE,D} + j \cdot i_{LINE,Q}$ and bus voltages $\underline{v} = v_D + j \cdot v_Q$ in this system model are taken into account and described with the following differential equations in the global DQ-reference frame:

$$\frac{d}{dt}\underline{i_{LINE}} = \frac{\omega_b}{L_{line}}\underline{v_S} - \frac{\omega_b}{L_{line}}\underline{v_R} - \left(\frac{\omega_b \cdot R_{line}}{L_{line}} + j \cdot \omega_b \cdot \omega_g\right) \cdot \underline{i_{LINE}}, \tag{6.4}$$

$$\frac{d}{dt}\underline{v} = \frac{\omega_b}{C_{line}} \Sigma \underline{i_{LINE}} - j \cdot \omega_b \cdot \omega_g \cdot \underline{v}, \tag{6.5}$$

where $\underline{v_S}$ and $\underline{v_R}$ are the sending-end and receiving-end voltages on a transmission line, ω_b and ω_g the base and per-unit grid frequencies, and L_{line}, R_{line} and C_{line} the line inductance, resistance and capacitance, respectively. Doing so, the number of state variables in the system grows significantly since each of the line currents and bus voltages are described with two state variables. The synchronous generator model used in this system model, also includes two additional state variables, describing the stator winding dynamics. Kirchhoff's laws are used for the integration of grid's currents and voltages with the differential algebraic equations of synchronous generator and VSC models.

Hybrid network model

In the hybrid network model, the methodology from [13] is adopted and includes a combination of the two previously described approaches. In the vicinity of a power electronic-based device (in this case, a VSC), the AC grid is modeled dynamically, and the rest of the grid is modeled by using the admittance matrix. This way, a number of state variables in a system does not grow significantly; and conversely, an accurate system behavior in the vicinity of a power-electronic device is preserved. The VSC model is combined with the dynamic grid model by using Kirchhoff's laws establishing the current injection model in the form:

$$\begin{aligned} \dot{\mathbf{x}}_{\mathbf{dyn}} &= \mathbf{f}(\mathbf{x}_{\mathbf{dyn}}, \mathbf{u}_{\mathbf{dyn}}, \mathbf{v}_{\mathbf{dyn}}) \\ \mathbf{i}_{\mathbf{dyn}} &= \mathbf{g}(\mathbf{x}_{\mathbf{dyn}}, \mathbf{u}_{\mathbf{dyn}}, \mathbf{v}_{\mathbf{dyn}}), \end{aligned} \tag{6.6}$$

where $\mathbf{x}_{\mathbf{dyn}}$ and $\mathbf{u}_{\mathbf{dyn}}$ are the state and input vectors of the dynamic network area, and $\mathbf{v}_{\mathbf{dyn}}$ and $\mathbf{i}_{\mathbf{dyn}}$ are the vectors of voltages and injection currents at the boundary between dynamic and a steady-state network area. Subsequently, this dynamic network area model is integrated with the admittance matrix of the rest of the grid which is modeled in a steady state.

6.2.2. Comparison procedure

For the comparison of different system models, a quantitative measure based on eigenvalue and participation factor analysis is established. Different system models are built and linearized

using Matlab/Simulink. The size of the state-space matrix, and consequently the number of eigenvalues, is the highest for a dynamic model and the lowest for a steady-state model, with a hybrid model being situated in-between. Therefore, for comparison purposes, only the eigenvalues for which the normalized participation of state variables of a power electronic-based device (VSC) has the dominant share, are used:

$$\lambda_i \in A_X \mid \sum_{x_k \in B} p(x_k, \lambda_i) > 0.5\,, \tag{6.7}$$

where A_X is the set of eigenvalues λ_i, related to the VSC obtained from the system model X ; B is the set of state variables x_k describing the VSC model.

The thus obtained sets of eigenvalues of the different system models are compared by calculating the total sum error of the damping of the eigenvalues related to the same state variables. The total sum error is defined as:

$$\varepsilon_\zeta = \sum_{\substack{\lambda_i \in A_{X1} \\ \lambda_j \in A_{X2}}} \frac{\mathrm{abs}(\zeta(\lambda_j) - \zeta(\lambda_i))}{\zeta(\lambda_i)}\,, \tag{6.8}$$

where λ_i and λ_j are the eigenvalues from the sets A_{X1} and A_{X2} related to the same state variables and with $\zeta(\lambda_i)$ the mode damping:

$$\zeta(\lambda_i) = \frac{-\mathrm{Re}(\lambda_i)}{\mathrm{Abs}(\lambda_i)}\,. \tag{6.9}$$

The obtained oscillatory modes (related to the VSCs) have the frequency of oscillation low enough to be adequately represented by a single π line model or they are confined to the converter's DC side. Therefore, in the comparison of different system models, the dynamic model of the entire system, is taken as the reference model. The proposed quantitative indicator, that is the total sum error, bundles all eigenvalues related to the VSC model into one single piece of information. Hence, the purpose of this indicator is not a discrimination between highly and poorly damped eigenvalues, but an overall indication of a first comparison of different system models.

6.3. Case study I: multi-infeed system with two converters

The layout of a generic VSC-based MI-HVDC system consisting of two converters, representing a reduced AC/DC system model, is shown in Fig. 6.1. The same configuration has also been used in the research in Chapter 5. The SCR at the PCC of converter 2 is lower in

comparison to the converter 1 SCR since converter 2 is connected to an external grid through an AC line. The state-space representations of two different models of the described system are established: a dynamic model – in which all elements are modeled dynamically and a hybrid model – in which the dynamics of the AC line is neglected. The overall number of state variables in the two system models and by different system elements, are summarized in Table 6.1. Both converters operate as rectifiers at their nominal power and without reactive power injection into the AC grid.

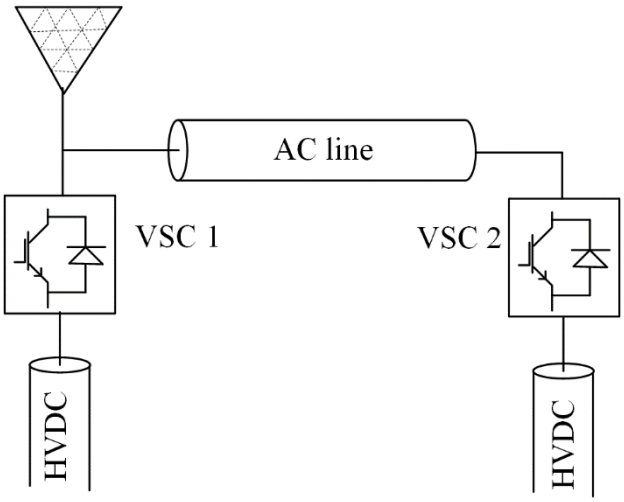

Figure 6.1: VSC-based MI-HVDC layout

Table 6.1: Number of state variables in different MI-HVDC models

Model elements	**Dynamic model**	**Hybrid model**
Converter 1	20	20
Converter 2	20	20
AC line	6	0
External grid	2	2
Overall	**48**	**42**

Fig. 6.2 shows the eigenvalues of the system extracted from the state-space matrices of the MI-HVDC dynamic and hybrid models and a 150 km long AC line. System modes slower than 2000 rad/s and with real parts larger than -4000 are presented. The green lines represent a 90% damping boundary; and modes with higher damping are not taken into consideration. A satisfactory matching of the two models can be observed, except for the two modes denoted by Mode 1 and Mode 2. Participation factor analysis of the dynamic model is employed to further analyze these

two modes (Figs. 6.3a and 6.3b). Mode 1 mostly depends on participation from the state variables related to the q-component of the filtered PCC voltage of converter 2 ($v_{ICC,q,2}$) employed as a feedforward term in the ICC and the Q-component of the AC line current ($i_{LINE,Q}$). Mode 2 is mostly related to the active power measurement of converter 2 ($p_{ac,f,2}$), the d-component of the filtered PCC voltage of converter 2 ($v_{ICC,d,2}$), employed as a feedforward term in the ICC and the D-component of the AC line current ($i_{LINE,D}$). The significant participation of the AC line state variables in the observed modes causes a difference between the models, since these variables are not present in the hybrid model. The different behavior of the two models is also demonstrated by the time-domain simulation in Fig. 6.4 for a converter 2 active power reference step.

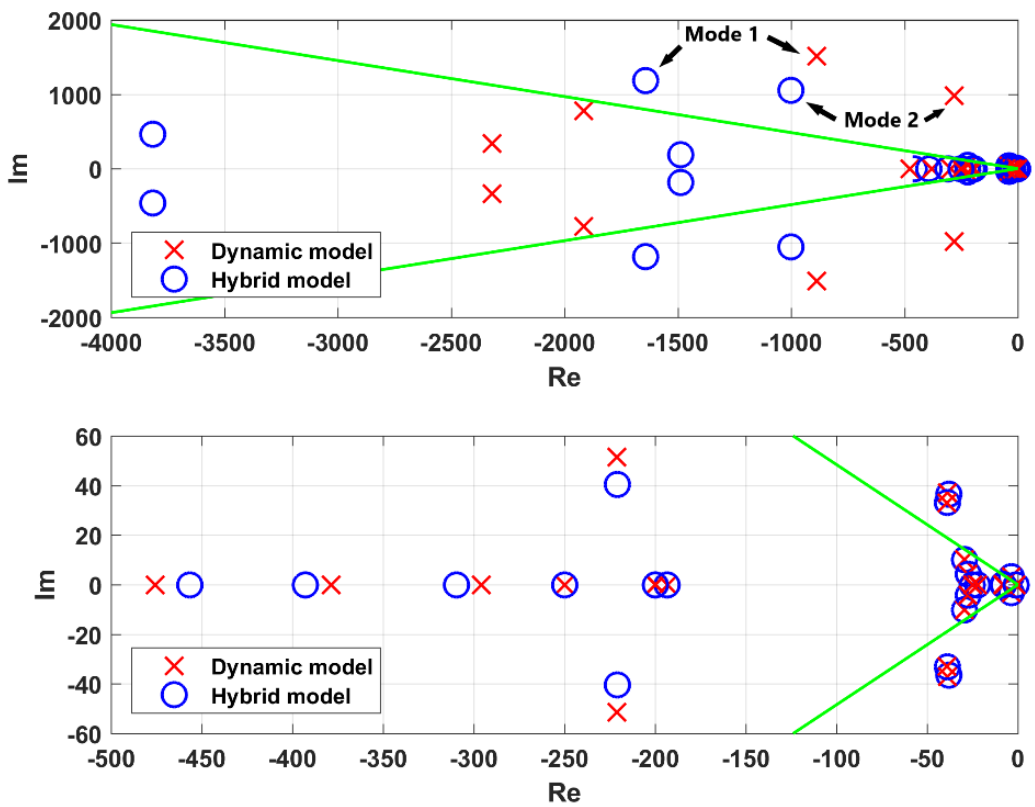

Figure 6.2: Eigenvalues of dynamic and hybrid MI-HVDC models

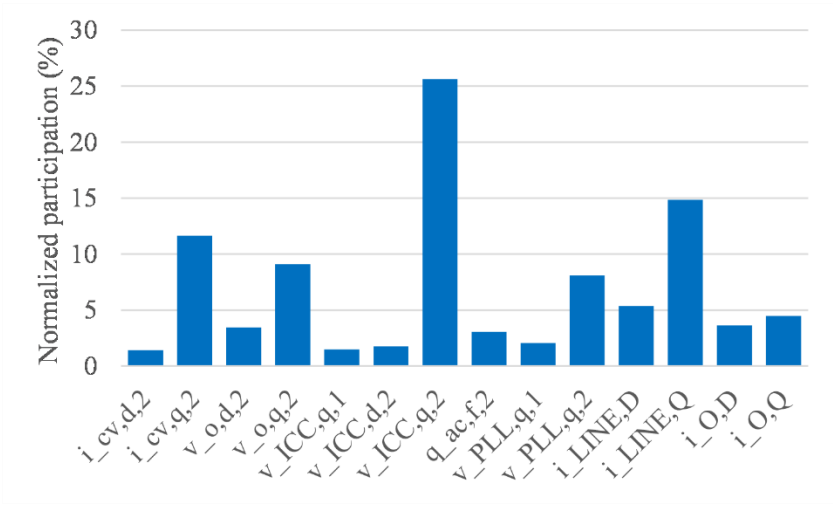

a)

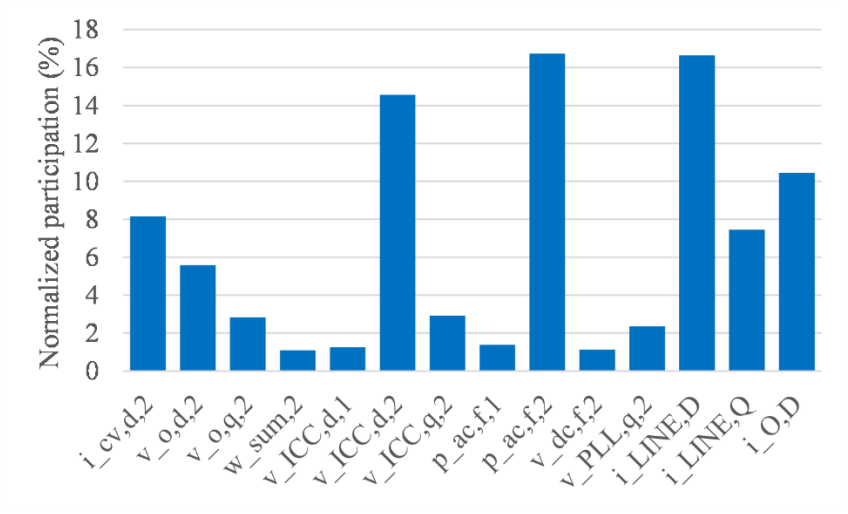

b)

Figure 6.3: Normalized participation factors in dynamic model of: a) Mode 1; b) Mode 2

The influence of the AC line length on damping of the observed modes is demonstrated in Fig. 6.5a. In the dynamic model, the observed modes become less damped, whereas in the hybrid model they remain almost unaltered. Therefore, the difference between the models is increased for longer AC lines. Similar behavior can be observed in Fig. 6.5b, where the influence of the PCC filter capacitance is examined. While the modes in the dynamic model become less damped with an increased value of filter capacitance, Mode 1 in the hybrid model remains almost unaltered, while the damping of Mode 2 becomes gradually lower. However, in some situations, these modes may become unstable. This is shown in Fig. 6.5c, demonstrating the influence of the droop coefficient value in the case when the AC voltage droop control is implemented in converter 2

(equation (3.33)). For values of the coefficient larger than 3.5, the dynamic model becomes unstable (damping of Mode 2 becomes negative) and this instability is not detected in the hybrid model. The conducted analysis shows an inadequacy of the steady-state AC line model in accurately representing system's small-signal stability.

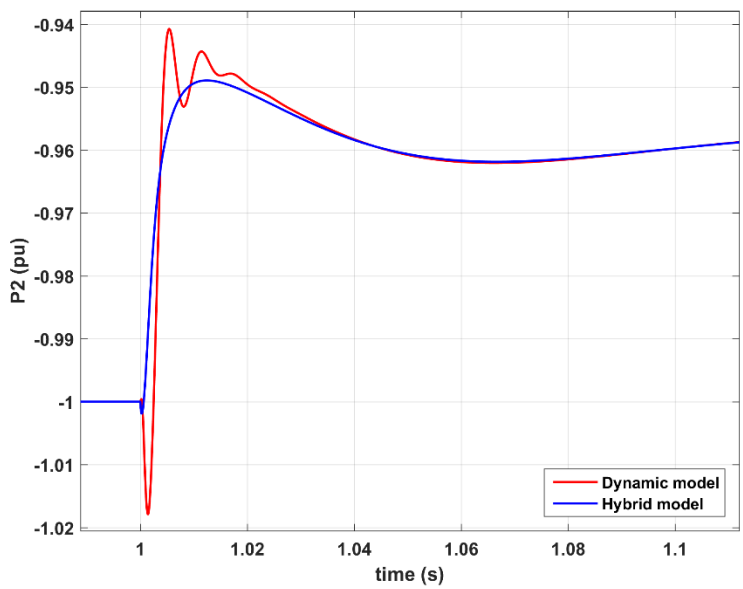

Figure 6.4: Time-domain response following a converter 2 active power reference step

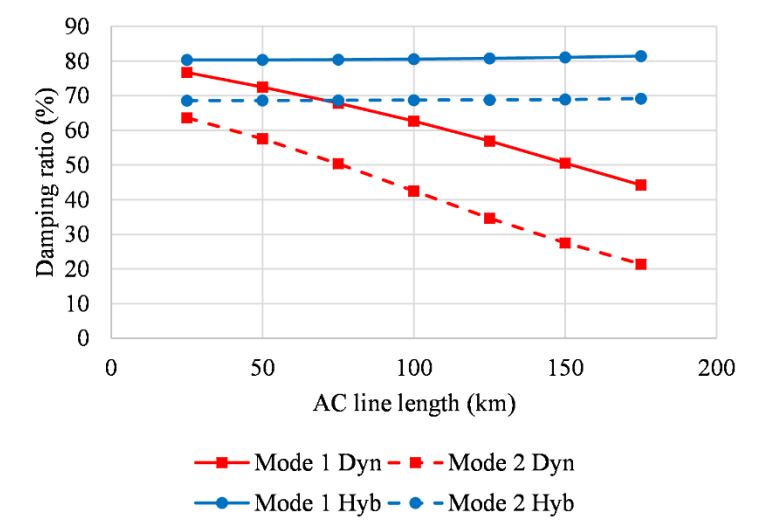

a)

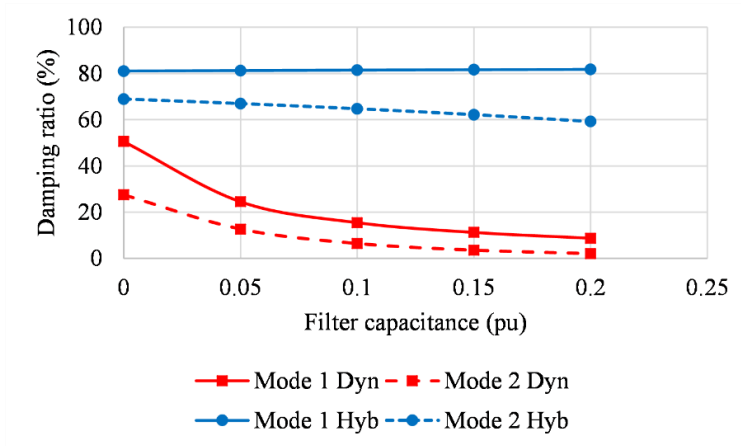

b)

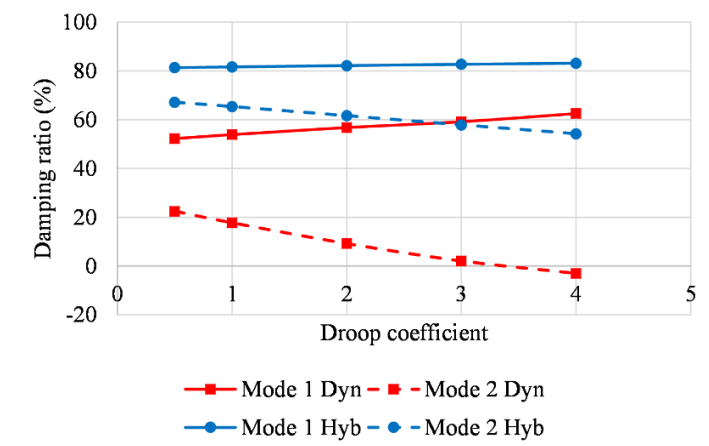

c)

Figure 6.5: Mode 1 and Mode 2 damping ratios for different: a) AC line lengths; b) PCC filter capacitances; c) AC voltage droop coefficients

6.4. Case study II: IEEE 39 bus system

The procedure for comparison of different system models described in Section 6.2.2 is applied to the IEEE 39 bus test system. The parameters of the test system are taken from [83] and can be found in Appendix C. First, analyses are performed with a single VSC HVDC station in the test system, and afterward with two VSC stations to represent the case with a MI-HVDC system embedded in the grid.

6.4.1. Single VSC station

First, the influence that location of the VSC HVDC station has on the accuracy of the steady-state model in relation to the dynamic-based model is assessed. In Fig. 6.6, the total sum error of the steady-state model for the first twelve buses, i.e. when the VSC station is located in

each of the buses, is depicted together with the corresponding three-phase short-circuit (SC) power at those buses. A clear relationship can be observed: with decreasing SC power, the total sum error of the steady-state model increases. SC powers are calculated using PSS/E and pre-fault bus voltages from power flow. In continuation, the VSC station installed at the bus with a relatively high SC power–bus 3–is considered.

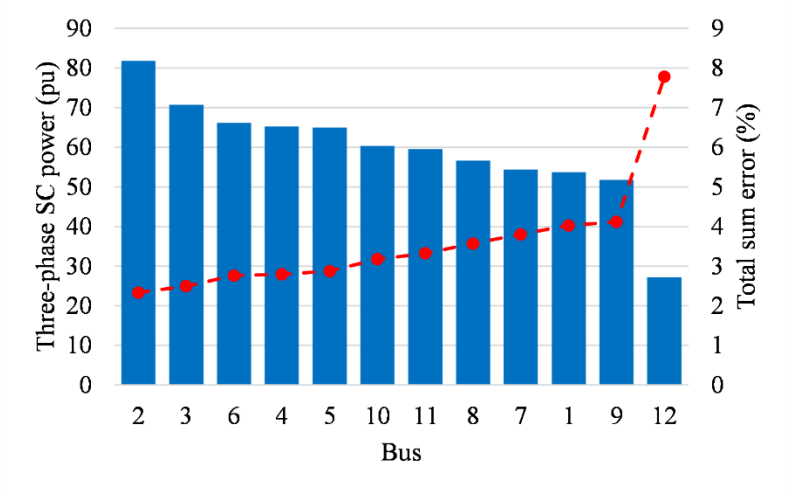

Figure 6.6: Total sum error of steady-state model and different locations of VSC station in the grid

Apart from dynamic and steady-state models, two more hybrid models are assembled. In hybrid model 1, bus 3 (connection of VSC) and adjacent lines (lines 2-3, 3-4 and 3-18) are modeled dynamically, as designated by the red color in Fig. 6.7. In hybrid model 2, more buses and lines are modeled dynamically—those adjacent to the previously mentioned ones and designated in Fig. 6.7 with the blue color. The generator connected to bus 30, in this case, is also modeled dynamically by taking into account stator dynamics. The number of state variables in different models and in different system elements are summarized in Table 6.2. The overall number of state variables in the dynamic model is approximately three times higher in comparison to the steady-state model.

Table 6.2: Number of state variables in different IEEE 39 models with embedded single VSC station

Model elements	**Dynamic model**	**Steady-state model**	**Hybrid model 1**	**Hybrid model 2**
Converter	20	20	20	20
AC grid	168	0	8	28
Generators	90	72	72	74
Overall	**278**	**92**	**100**	**122**

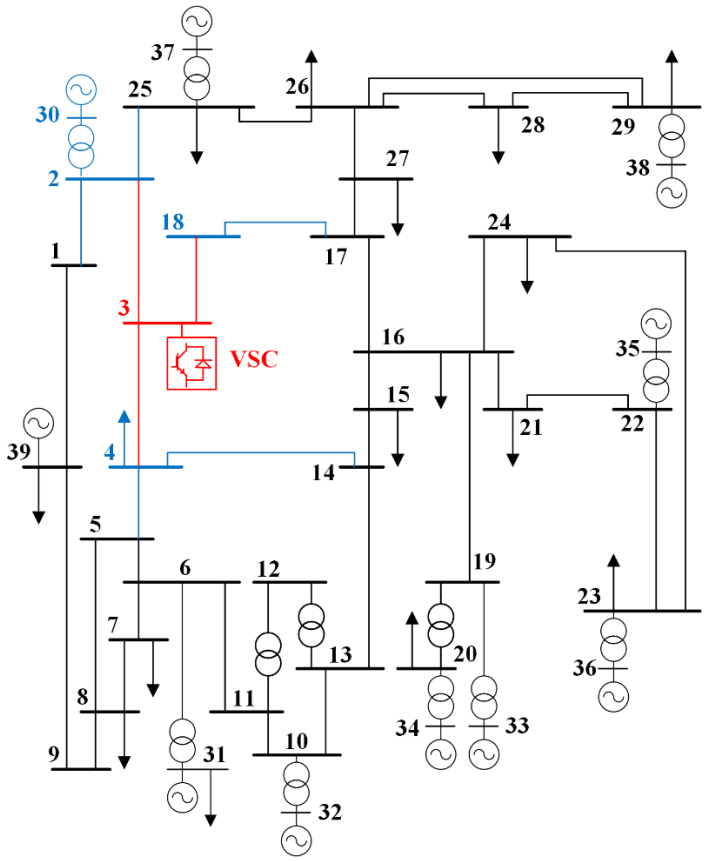

Figure 6.7: IEEE 39 bus test system with one VSC station

The influence of the following converter parameters on the total sum error of different models has been examined: a PLL speed response, an active power control speed response, an active power setpoint, and a type of reactive power control. The speed response of control loops is in close correlation with coefficient values of PI regulators. The parameters of the base case are given in Table 6.3 and the parameters of different observed cases in Table 6.4. Case 1 considers slower PLL control, Case 2 slower active power control, Case 3 lower converter active power and Case 4 AC voltage control instead of reactive power control. The results are presented in Fig. 6.8. It can be observed that the total sum error for each investigated case decreases when more buses and lines are modeled dynamically (hybrid models in comparison to steady-state model). The PLL speed response has the largest influence on the total sum error and the difference between steady-state and hybrid models is the lowest (Case 1). After this follows the type of reactive power control, then the active power setpoint. The speed response of the active power control has the smallest influence on the total sum error amongst the investigated cases. These results are also confirmed by the fact that the relative error of the eigenvalues related to the PLL states are the highest in the base case.

Table 6.3: Parameters of the base case

Phase-locked loop: $k_{p,PLL} = 50$, $k_{i,PLL} = 833$
Active power control: $k_{p,P} = 1$, $k_{i,P} = 50$
Active power setpoint: $P_{ac} = 500$ MW
Reactive power control: $Q_{ac} = 0$ MVAr

Table 6.4: Parameters of different observed cases

Case	Parameters
Case 1	$k_{p,PLL} = 25$, $k_{i,PLL} = 208$
Case 2	$k_{p,P} = 0.5$, $k_{i,P} = 25$
Case 3	$P_{ac} = 250$ MW
Case 4	AC voltage control ($Q_{ac} = 0$ MVAr)

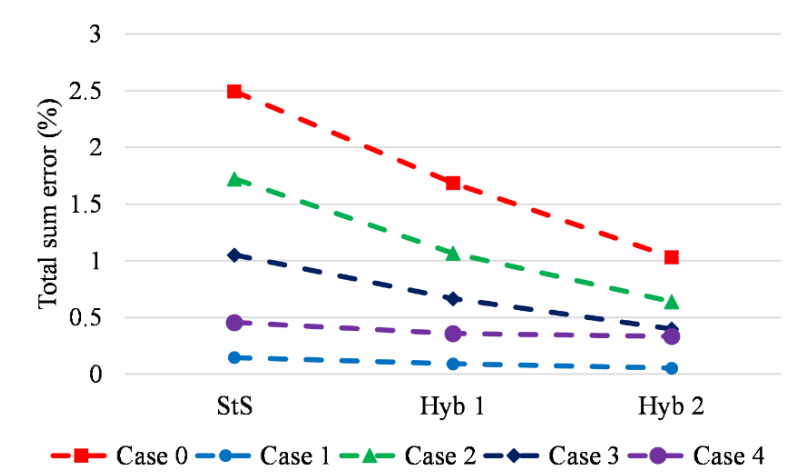

Figure 6.8: Total sum error for different observed cases

Since the PLL speed response is found to have the highest impact on the total sum error, the influence of the PLL regulator coefficients are further examined; and results are presented in Fig. 6.9. The integral gain of the PI regulator is changed proportionally with proportional gain, hence maintaining the same integrator time constant. Apart from the total sum error, Fig. 6.9 also shows the PLL eigenvalue relative error for different system models labeled with a dotted line. For the values of the PLL proportional gains between 30 and 40, a notable decline in the total sum error and PLL error can be observed. For values outside this range, changes in the total sum error and PLL error are less pronounced.

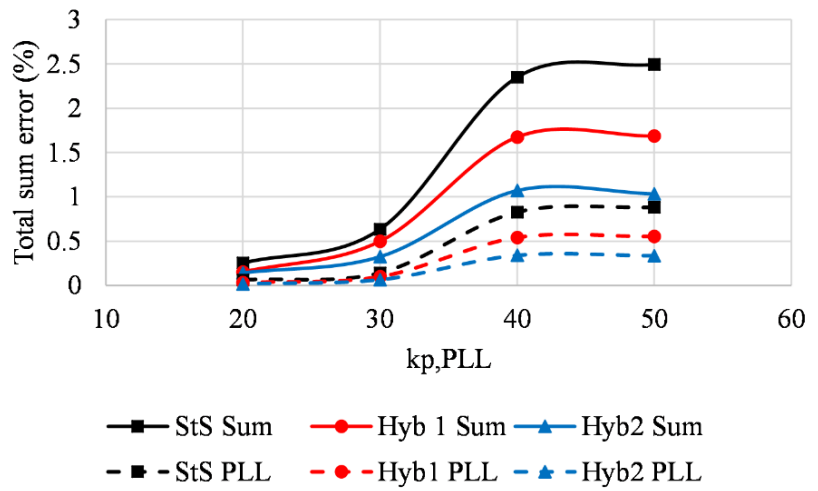

Figure 6.9: Total sum error for different PLL proportional gains

6.4.2. MI-HVDC system

Adjacent to the VSC from the previous section, another converter operating as rectifier ($P_{ac} = 250$ MW) is connected to neighboring bus 4 (Fig. 6.10). In this case, three levels of hybrid models have been assessed with the following buses and lines modeled dynamically:

- hybrid model 1: line 3-4 (designated with the red color in Fig. 6.10)
- hybrid model 2: buses 3 and 4, lines 2-3, 3-18, 4-5 and 4-14 (designated with the blue color)
- hybrid model 3: buses 2, 5, 14, 18 and 30, lines 1-2, 2-25, 2-30, 5-6, 5-8,13-14, 14-15, 17-18 and generator connected to bus 30 (designated with the green color)

The number of state variables in different system models and distributed by system elements are summarized in Table 6.5. The overall number of state variables in the dynamic model is roughly three times higher in comparison to the steady-state model and two-times higher in comparison to hybrid model 3.

Table 6.5: Number of state variables in different IEEE 39 models with embedded MI-HVDC system

Model elements	Dynamic model	Steady-state model	Hybrid model 1	Hybrid model 2	Hybrid model 3
Converters	40	40	40	40	40
AC grid	168	0	2	14	40
Generators	90	72	72	72	74
Overall	**298**	**112**	**114**	**126**	**154**

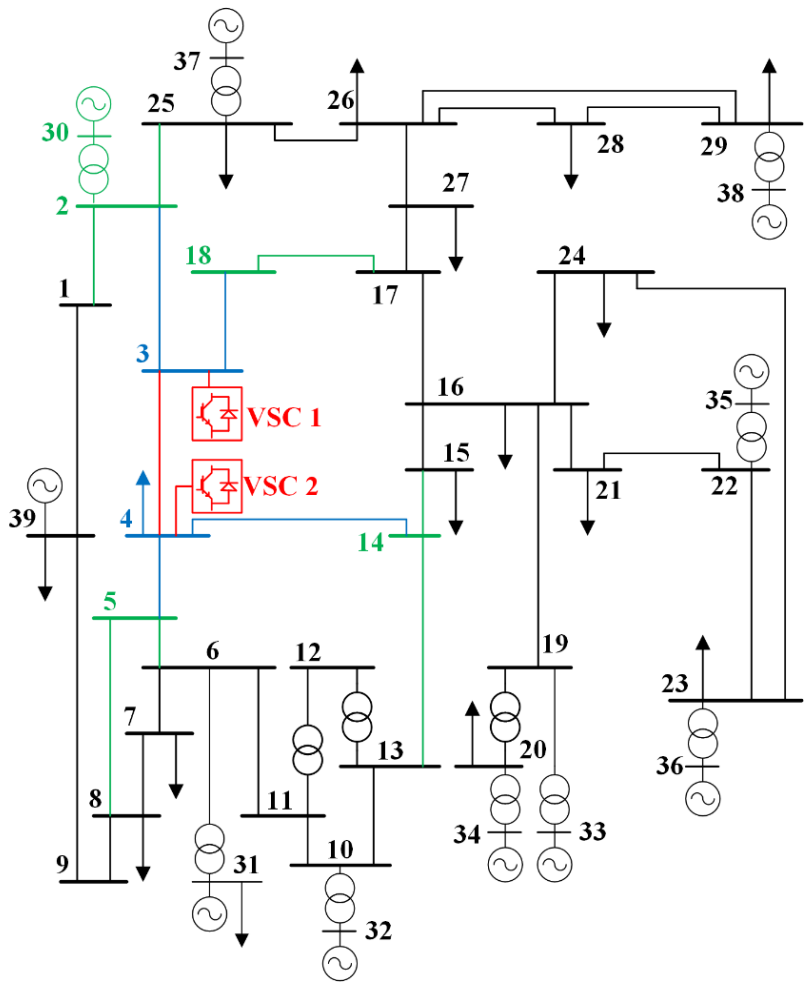

Figure 6.10: IEEE 39 bus test system with two VSC stations

In Figs. 6.11a and 6.11b total sum errors of different models are considered, with respect to the length of line 3-4 (line interconnecting two VSC stations) for fast ($k_{p,PLL} = 50$, $k_{i,PLL} = 833$, Fig. 6.11a) and slow PLL ($k_{p,PLL} = 20$, $k_{i,PLL} = 133$, Fig. 6.11b). The length of the line is increased two, three and four times. Since the lines in the IEEE 39 bus system are relatively short, dynamic modeling of the line, by using one π-section, is also sufficient for the lines that are up to four times longer. It can be observed from Fig. 6.11a that for longer interconnecting lines, the total sum error of different system models becomes more dispersed. Therefore, it can be concluded that more accurate modeling (with more dynamically modeled buses and lines) is more effective for a longer interconnecting line between converters. Total sum errors of different models for slow PLL speed response also become more dispersed with longer interconnecting lines, but to a much smaller

extent, as can be noticed in Fig. 6.11b. Hence, the effectiveness of accurate AC grid modeling with a longer interconnecting line is not as pronounced as is the case for a fast PLL speed response.

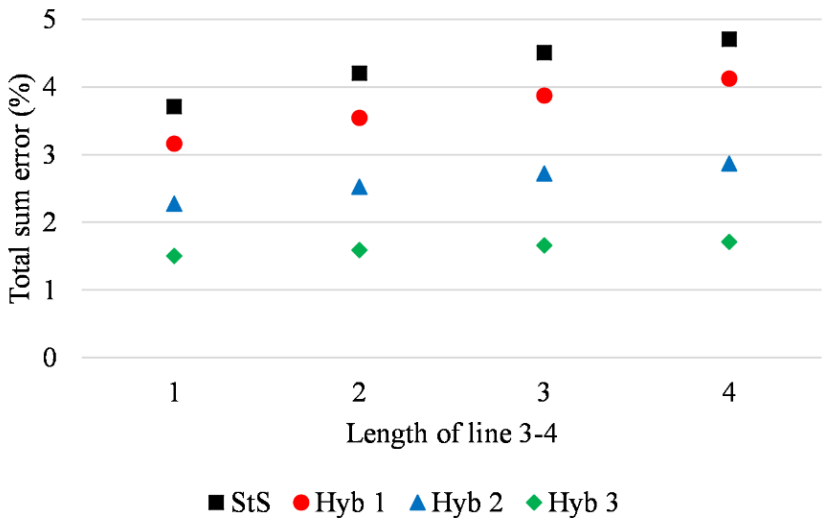

a)

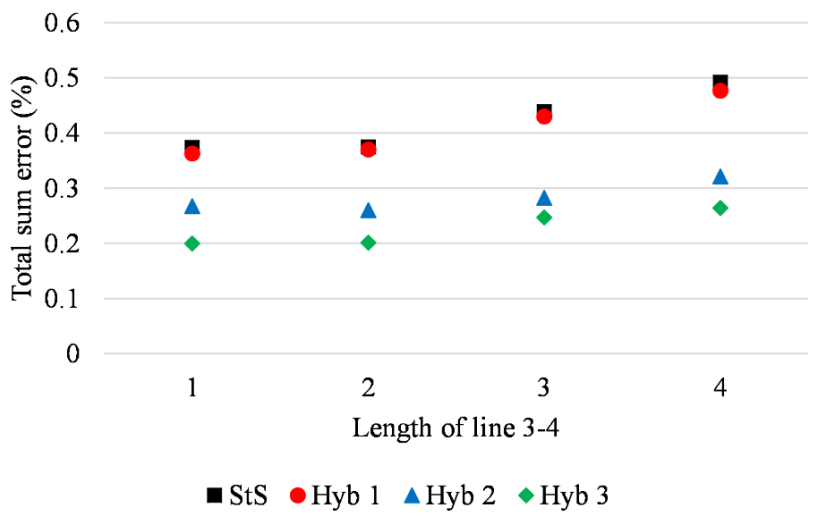

b)

Figure 6.11: Total sum error for different system models and lengths of interconnecting line 3-4: a) fast PLL; b) slow PLL

In Figs. 6.12a and 6.12b, in contrast to Figs. 6.11a and 6.11b, apart from interconnecting line 3-4, lengths of converters' neighboring lines (lines 2-3, 3-18, 4-5, 4-14) are also increased two, three and four times. This has been carried out again for fast (Fig. 6.12a) and slow PLL speed responses (Fig. 6.12b). The total sum errors of the steady-state models become significantly higher, in comparison to the previous case, when only the interconnecting line length was increased.

Hybrid 1 models, in which only the interconnecting line is modeled dynamically, reduce the error comparatively to steady-state models; but, a more significant reduction is achieved when using hybrid 2 models in which all the neighboring lines are also modeled dynamically (which corresponds to the lines whose lengths are increased in this study case). Finally, hybrid 3 models, in which additional lines are modeled dynamically, reduce the error further; but not that notably in comparison to the hybrid 2 model error reduction. A clear grouping of the steady-state and hybrid model 1 total sum errors, as well as hybrid model 2 and hybrid model 3 total sum errors can be observed. The total sum errors of hybrid models 2 and 3 even start to decrease with longer line lengths and fast PLL (Fig. 6.12a), which is not the case for a slow PLL speed response (Fig. 6.12b).

6.5. Conclusion

The importance of appropriate AC grid modeling has been demonstrated in the case of a generic MI-HVDC system with two VSCs. Instability caused by high converter's AC voltage droop coefficients remains undetected if the interconnecting AC line is not modeled dynamically.

The application of the comparison of different AC network models in the case of a larger AC system with embedded VSC HVDC stations shows that with lower SCR at the converter's PCC the accuracy of the steady-state AC network model decreases. Furthermore, it has been demonstrated that among investigated converter parameters, the PLL speed control has the most significant impact on the accuracy of the system models with embedded VSC HVDC station. Therefore, in the case of fast PLL control and/or low SCR at the PCC, a larger portion of an AC grid needs to be modeled dynamically. Lastly, lengths of the converters' interconnecting and neighboring AC lines are investigated, indicating the extent of an AC grid in the vicinity of a VSC station which needs to be modeled dynamically. The obtained results confirm that if long AC lines around a VSC station are modeled dynamically, a significant reduction in total sum error can be achieved. This is especially emphasized with faster PLL speed control.

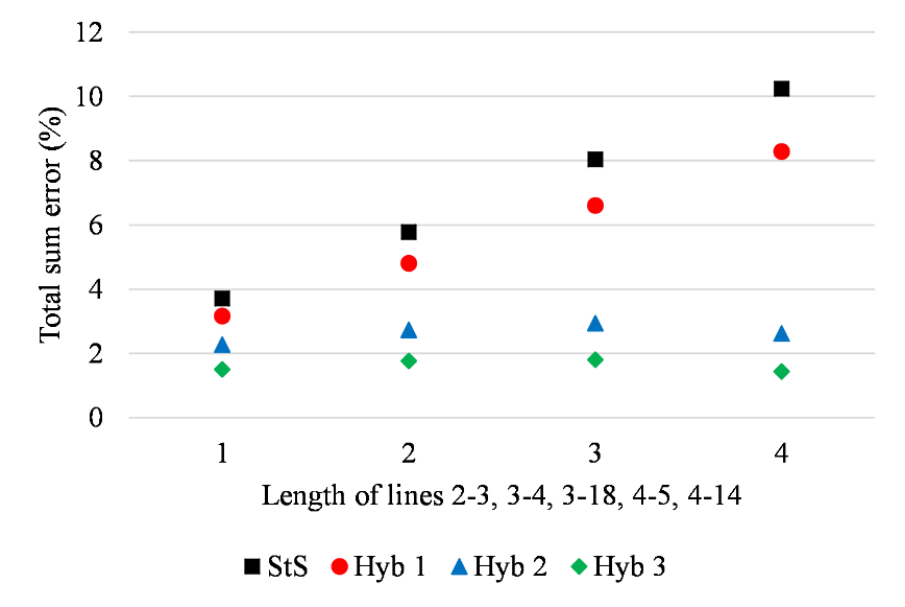

a)

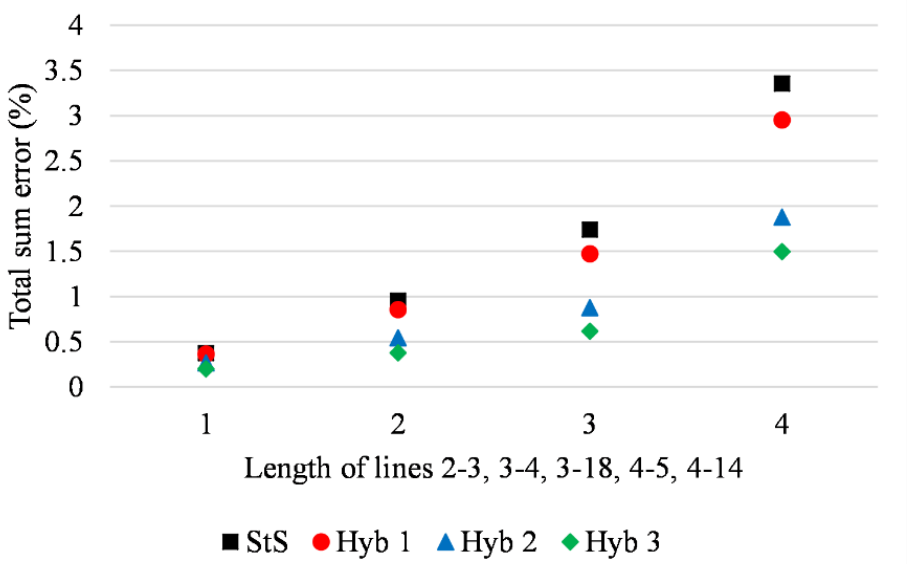

b)

Figure 6.12: Total sum error for different system models and lengths of VSC neighboring lines: a) fast PLL; b) slow PLL

7. CONCLUSIONS AND FUTURE WORK

7.1. Conclusions

VSCs are being increasingly employed in HVDC applications because of their inherent advantages compared with LCCs. One of the most important benefits of VSCs is that they have enabled the implementation of truly meshed multi-terminal DC grids. The first such grid is currently being built, and before their widespread application, a thorough investigation of different properties is required. In AC grids, more VSCs are being located mutually in electrical proximity, forming MI-HVDC systems. Many aspects regarding operation, control, and modeling requirements of both configurations have not been explored completely. This thesis focuses on the small-signal stability properties of VSC-based HVDC systems, that is, MTDC grids and MI-HVDC systems.

Chapter 4 emphasizes on the HVDC grid interaction modes—modes in which state variables from more than one subsystem participate. First, interaction modes have been investigated in a simple radial DC grid with a voltage margin control. It has been shown that the dominant interaction mode becomes more stable with increasing the active power at the voltage controlling converter, with symmetrical loading of converters and shorter electrical distances between converters. In addition, the dominant interaction mode becomes less stable with higher values of the voltages in a DC grid. The stability margin of the dominant interaction mode thus becomes notably reduced in the case of low power flow, especially in DC grids with relatively long cable connections. Second, based on the findings of these analyses, the strategy for the selection of a voltage controlling converter is derived. The converter current combined with converter power can determine the stability of the dominant interaction mode more precisely. This has been carried out for two grid configurations: for radial grids with an arbitrary number of terminals and for grids in a triangular configuration. Finally, the strategy for the selection of a voltage controlling converter is generalized to the voltage droop control, resulting in the method for tuning coefficients of proportional controllers. If the order of the droop coefficients is equal to that of the stability of the dominant interaction modes (when a certain converter is in charge of voltage control in the margin control method), the dominant interaction mode is the most stable and vice versa.

Chapter 5 focuses on identifying the small-signal stability properties of different outer control loops for reactive power and AC voltage regulation in a generic VSC-based MI-HVDC system. The studied system consists of two VSC HVDC infeeds based on MMCs interconnected with an AC line and connected to an external grid. Investigated control methods include constant reactive power, constant AC voltage, AC voltage droop control, and remote bus voltage control. The type of control employed at the converter with a lower SCR at the PCC (farther from an external grid) has more influence on the system response in comparison to the type of control employed at the converter with a higher SCR (closer to an external grid). It has been shown and discussed that the AC voltage control employed at the converter with a lower SCR aggravates the stability of the least damped mode compared to the reactive power control employed at the same converter. In AC voltage droop control, larger droop coefficients are possible when this type of control is employed at the converter with a higher SCR at the PCC. The location of AC voltage measurement in the remote bus voltage control method has been found not to have a notable influence on small-signal stability in MI-HVDC systems. The study has been expanded further by the subsystem participation analysis of selected modes and by considering the impact of the AC line length and power flow. Increasing the AC line length generally has a negative impact on system stability while low AC line power flow increases the stability of some modes and decreases the stability of others. Subsystem participation analysis has revealed that low active power flow on the transmission line and an increase in AC line length generally have a positive decoupling effect on the converters' active power and zero-energy sum control. Finally, the importance of an appropriate AC line modeling has been demonstrated by showing how the steady-state representation of an AC line overestimates the small-signal stability of the system.

The procedure for the comparison of different AC grid models based on the SSSA is introduced in Chapter 6 and applied in the case of a single and double VSC HVDC infeed in a relatively larger AC grid. The hybrid network model has been proposed in literature, where the AC grid in the vicinity of a dynamic device is modeled dynamically and the rest of the grid statically or in a steady state. However, the boundary selection between these two grid parts has not been discussed in literature so far. The conducted research has shown that the SCR at the converter's PCC significantly influences the accuracy of the steady-state AC grid model with a single VSC HVDC infeed. Furthermore, among the investigated converter parameters—the speed of the PLL control and the active power control, the active power quantity, and the type of reactive power

control method—the speed of the PLL control has been found to have the largest impact on the accuracy of steady-state and hybrid AC grid models. Therefore, in the case of fast PLL control, a larger portion of an AC grid needs to be modeled dynamically. Lastly, the influence of interconnecting and neighboring AC line lengths in the case of a double VSC HVDC infeed is considered. Significant error reduction can be achieved if long AC lines adjacent to VSC stations are modeled dynamically.

7.2. Future work

The proposal for future research regarding interaction modes in MTDC grids incorporates the investigation of interaction modes in hybrid DC grids which include LCCs and VSCs. While VSCs are the preferred technology for offshore converter stations, LCCs are still being employed because of their higher available power, lower losses, and lower price. DC grids including both types of converters have already been proposed and are expected to be built in the near future. Besides, in meshed DC grids, in which the number of cables/lines is larger than the number of converters, power flow cannot completely be controlled by converters. Thus, power flow devices will be necessary to control the power flow in each line. Therefore, another recommendation is to investigate the influence that power-controlling devices in DC grids (series current flow controllers, low stepping ratio DC/DC converters) have on the stability of interaction modes.

The research proposal regarding reactive power support in MI-HVDC systems is twofold: (i) to include and investigate the impact of capacitors (as reactive power producers) and LCCs (as reactive power consumers) on small-signal stability properties and (ii) to apply a holistic approach, that is, to extend the SSSA with load-flow and transient stability analysis. Furthermore, in transient stability analysis, the recommendation is to analyze and compare different power limitation strategies in VSCs. These include the priority of either active or reactive power or the operation at a constant power factor.

References

[1] D. Van Hertem and M. Delimar, "High Voltage Direct Current (HVDC) electric power transmission systems," in *Electricity transmission, distribution and storage systems*, Woodhead, 2013, pp. 143-173.

[2] C.-K. Kim, V. K. Sood, G.-S. Jang, S.-J. Lim and S.-J. Lee, HVDC TRANSMISSION Power Conversion Applications in Power Systems, Singapore: John Wiley & Sons, 2009.

[3] IEEE HVDC and FACTS Subcommittee, "Existing HVDC project listing," 2013. [Online]. Available: http://www.ece.uidaho.edu/hvdcfacts/. [Accessed 4 May 2019].

[4] ABB, "HVDC Classic reference list," 2017. [Online]. Available: https://new.abb.com/systems/hvdc/references. [Accessed 4 May 2019].

[5] "Multi-terminal VSC HVDC transmission project commissioned in China," SUBSEA world news, January 2014. [Online]. Available: https://subseaworldnews.com/2014/01/24/multi-terminal-vsc-hvdc-transmission-project-commissioned-in-china/. [Accessed 4 May 2019].

[6] "Zhoushan five-terminal VSC-HVDC Project," NR Electric Co., [Online]. Available: http://www.nrec.com/en/case/-449.html. [Accessed 4 May 2019].

[7] "Zhangbei The world's first DC-grid with HVDC Light," ABB, [Online]. Available: https://new.abb.com/systems/hvdc/references/zhangbei. [Accessed 4 May 2019].

[8] F. Van Hulle, J. O. Tande, K. Uhlen, L. Warland, M. Korpås, .. P. Meibom and J. Völker, "Integrating wind: Developing Europe's power market for the large-scale integration of wind power," European Wind Energy, 2009.

[9] N. Fichaux and J. Wilkes, "Oceans of Opportunity Harnessing Europe’s largest domestic energy resource," European Wind Energy Association (EWEA), 2009.

[10] "Unsolicited Right-of-Way Grant Application for the Atlantic Wind Connection Project," Ecology and Environment, inc., 2011.

[11] U.S. Energy Information Administration, "Assessing HVDC Transmission for Impacts of Non-Dispatchable Generation," U.S. Energy Information Administration, 2018.

[12] P. Kundur, Power System Stability and Control, New York: McGraw-Hill, 1993.

[13] C. Karawita and U. D. Annakkage, "A Hybrid Network Model for Small Signal Stability Analysis of Power Systems," *IEEE Transactions on Power Systems,* vol. 25, no. 1, pp. 443-451, 2010.

[14] G. Grdenić and M. Delimar, "Energetska elektronika u visokonaponskom istosmjernom prijenosu električne energije," in *14th HRO CIGRE Session*, Šibenik, 2019.

[15] ABB, "The Gotland HVDC link," [Online]. Available: https://new.abb.com/systems/hvdc/references/the-gotland-hvdc-link. [Accessed 21 October 2019].

[16] D. A. Woodford, "HVDC Transmission," March 1998. [Online]. Available: https://hvdc.ca/uploads/ck/files/BasisPrinciplesofHVDC.pdf. [Accessed 13 February 2019].

[17] D. Jovčić and K. Ahmed, High-voltage direct-current transmission: converters, systems and dc grids, Wiley, 2015.

[18] Siemens, "HVDC Classic," 2017. [Online]. Available: https://new.siemens.com/global/en/products/energy/high-voltage/high-voltage-direct-current-transmission-solutions/hvdc-classic.html. [Accessed 13 February 2019].

[19] General Electric, "HVDC Systems," [Online]. Available: https://www.gegridsolutions.com/PowerD/catalog/hvdc.htm. [Accessed 2019 February 2019].

[20] ABB, "Changji-Guquan UHVDC link," [Online]. Available: https://new.abb.com/systems/hvdc/references/changji-guquan-uhvdc-link. [Accessed 14 February 2019].

[21] ABB, "Gotland HVDC Light," [Online]. Available: https://new.abb.com/systems/hvdc/references/gotland-hvdc-light. [Accessed 14 February 2019].

[22] ABB, "HVDC Light reference list," 2018. [Online]. Available: https://new.abb.com/systems/hvdc/references. [Accessed 4 May 2019].

[23] N. Mohan, T. M. Undeland and W. P. Robbins, Power Electronics: Converters, Applications, and Design, John Wiley & Sons, 2003.

[24] ABB, "HVDC Light It's time to connect," 2013. [Online]. Available: https://new.abb.com/docs/default-source/ewea-doc/hvdc-light.pdf. [Accessed 21 October 2019].

[25] M. Barnes and A. Beddard, "Voltage Source Converter HVDC Links – The state of the Art and Issues Going Forward," *Energy Procedia,* no. 24, pp. 108-122, 2012.

[26] K. Sharifabadi, L. Harnefors, H.-P. Nee, S. Norrga and R. Teodorescu, Design, Control, and Application of Modular Multilevel Converters for HVDC Transmission Systems, Wiley - IEEE Press, 2016.

[27] Amprion, "Project description: Ultranet," [Online]. Available: https://www.amprion.net/Grid-expansion/Our-Projects/Ultranet/. [Accessed 21 October 2019].

[28] TSCNET Services, "New HVDC technology for Ultranet," [Online]. Available: https://www.tscnet.eu/new-hvdc-technology-for-ultranet/. [Accessed 21 October 2019].

[29] C. C. Davidson and D. R. Trainer, "Innovative concepts for hybrid multi-level converters for HVDC power transmission," in *9th IET International Conference on AC and DC Power Transmission (ACDC 2010)*, London, 2010.

[30] G. Buigues, V. Valverde, A. Etxegarai, P. Eguía and E. Torres, "Present and future multiterminal HVDC systems: current status and forthcoming," in *International Conference on Renewable Energies and Power Quality (ICREPQ'17)*, Malaga, 2017.

[31] D. Van Hertem, M. Ghandhari and M. Delimar, "Technical limitations towards a SuperGrid — A European prospective," in *IEEE International Energy Conference*, Manama, 2010.

[32] M. Amin and M. Molinas, "Small-Signal Stability Assessment of Power Electronics Based Power Systems: A Discussion of Impedance- and Eigenvalue-Based Methods," *IEEE Transactions on Industry Applications,* vol. 53, no. 5, pp. 5014-5030, 2017.

[33] J. Machowski, J. W. Bialek and J. R. Bumby, Power System Dynamics, Stability and Control, Wiley, 2008.

[34] J. Beerten, S. D'Arco and J. A. Suul, "Identification and Small-Signal Analysis of Interaction Modes in VSC MTDC Systems," *IEEE Transactions on Power Delivery,* vol. 31, no. 2, pp. 888-897, 2016.

[35] S. D'Arco, J. A. Suul and M. Molinas, "Implementation and Analysis of a Control Scheme for Damping of Oscillations in VSC-Based HVDC Grids," in *16th International Power Electronics and Motion Control Conference and Exposition (PEMC)*, Antalya, 2014.

[36] M. Imhof and G. Andersson, "Dynamic Modeling of a VSC HVDC Converter," in *48th International Universities' Power Engineeering Conference (UPEC)*, Dublin, 2013.

[37] G. Bergna Diaz, J. A. Suul and S. D'Arco, "Energy-Based State-Space Representation of Modulat Multilevel Converters with a Constant Equilibrium Point in Steady-State Representation," *IEEE Transactions on Power Electronics,* vol. 33, no. 6, pp. 4832-4851, 2018.

[38] G. Bergna Diaz, J. A. Suul and S. D'Arco, "Small-Signal State-Space Modeling of Modular Multilevel Converters for System Stability Analysis," in *IEEE Energy Conversion Congress and Exposition ECCE*, Montreal, 2015.

[39] G. Grdenić and M. Delimar, "Small-Signal Stability Analysis of Interaction Modes in VSC MTDC Systems with Voltage Margin Control," *Energies,* vol. 10, no. 873, 2017.

[40] C. Gavriluta, I. J. Candela, J. Rocabert, A. Luna and P. Rodriguez, "Adaptive Droop for Control of Multiterminal DC Bus Integrating Energy Storage," *IEEE Transactions on Power Delivery,* vol. 30, no. 1, pp. 16-24, 2015.

[41] M. Raza, K. Schonleber and O. Gomis-Bellmunt, "Droop Control Design of Multi-VSC Systems for Offshore Networks to Integrate Wind Energy," *Energies,* vol. 9, no. 826, 2016.

[42] X. Zhang, Z. Wu, M. Hu, X. Li and G. Lv, "Coordinated Control Strategies of VSC-HVDC-Based Wind Power Systems for Low Voltage Ride Through," *Energies,* vol. 8, pp. 7224-7242, 2015.

[43] S. Azizi, M. Sanaye-Pasand, M. Abedini and A. Hasani, "A Traveling-Wave-Based Methodology for Wide-Area Fault Location in Multiterminal DC Systems," *IEEE Transactions on Power Delivery,* vol. 29, no. 6, pp. 2552-2560, 2014.

[44] S. Xue, J. Yang, Y. Chen, C. Wang, Z. Shi, M. Cui and B. Li, "The Applicability of Traditional Protection Methods to Lines Emanating from VSC-HVDC Interconnectors and a Novel Protection Principle," *Energies,* vol. 9, no. 400, 2016.

[45] N. R. Chaudhuri, R. Majumder, B. Chaudhuri and J. Pan, "Stability Analysis of VSC MTDC Grids Connected to Multimachine AC Systems," *IEEE Transactions on Power Delivery,* vol. 26, no. 4, pp. 2774-2784, 2011.

[46] P. Rault, *Dynamic Modeling and Control of Multi-Terminal HVDC Grids,* Lille: Université Lille Nord-de-Franc, 2014.

[47] M. K. Zadeh, M. Amin, J. A. Suul, M. Molinas and O. B. Fosso, "Small-signal stability study of the CIGRE DC grid test system with analysis of participation factors and parameter sensitivity of oscillatory modes," in *Proceedings of the 18th Power Systems Computation Conference (PSCC)*, Wroclaw, 2014.

[48] G. O. Kalcon, G. P. Adam, O. Anaya-Lara, S. Lo and K. Uhlen, "Small-Signal Stability Analysis of Multi-Terminal VSC-Based DC Transmission Systems," *IEEE Transactions on Power Systems,* vol. 27, no. 4, pp. 1818-1830, 2012.

[49] J. Z. Zhou, H. Ding, S. Fan, Y. Zhang and A. M. Gole, "Impact of Short-Circuit Ratio and Phase-Locked-Loop Parameters on the Small-Signal Behavior of a VSC-HVDC Converter," *IEEE Transactions on Power Delivery,* vol. 29, no. 5, pp. 2287-2296, 2014.

[50] G. Pinares, L. Bertling Tjernberg, L. A. Tuan, C. Breitholtz and A.-A. Edris, "On the Analysis of the DC Dynamics of Multi-Terminal VSC-HVDC Systems Using Small Signal Modeling," in *Proceedings of the IEEE PowerTech*, Grenoble, 2013.

[51] B. Gustavsen and A. Semlyen, "Rational approximation of frequency domain responses by Vector Fitting," *IEEE Transactions on Power Delivary,* vol. 14, no. 3, pp. 1052-1061, 1999.

[52] B. Gustavsen, "Improving the pole relocating properties of vector fitting," *IEEE Transactions on Power Delivery,* vol. 21, no. 3, pp. 1587-1592, 2006.

[53] D. Deschrijver, M. Mrozowski, T. Dhaene and D. De Zutter, "Macromodeling of Multiport Systems Using a Fast Implementation of the Vector Fitting Method," *IEEE Microwave and Wireless Components Letters,* vol. 18, no. 6, pp. 383-385, 2008.

[54] J. Beerten, S. D'Arco and J. A. Suul, "Cable Model Order Reduction for HVDC Systems Interoperability Analysis," in *Proceedings of the 11th IET International Conference on AC and DC Power Transmission*, Birmingham, 2015.

[55] G. Grdenić, M. Delimar and J. Beerten, "Comparative Analysis on Small-Signal Stability of Multi-Infeed VSC HVDC System With Different Reactive Power Control Strategies," *IEEE Access,* vol. 7, pp. 151724-151732, 2019.

[56] L. Xu, P. Dong and M. Liu, "A comparative analysis of the interaction between different FACTS and HVDC," in *Proceedings of the 2012 IEEE Power and Energy Society General Meeting*, San Diego, 2012.

[57] L. Shen, M. Barnes and J. V. Milanović, "Interactions between STATCOM and VSC HVDC in dynamic GB system," in *Proceedings of the 7th IET International Conference on Power Electronics, Machines and Drives (PEMD 2014)*, Manchester, 2014.

[58] C. Guo, W. Liu, J. Zhao and C. Zhao, "Impact of control system on small-signal stability of hybrid multi-infeed HVDC system," *IET Generation, Transmission & Distribution,* vol. 12, no. 19, pp. 4233-4239, 2018.

[59] C. Guo, W. Liu, C. Zhao and X. Ni, "Small-signal dynamics and control parameters optimization of hybrid multi-infeed HVDC system," *International Journal of Electrical Power & Energy Systems,* vol. 98, pp. 409-418, 2018.

[60] X. Deng, K. H. Ahmed and D. Jovčić, "Power flow algorithm based on current injections for analysis of multi-infeed VSC-HVDC system," in *Proceedings of the 8th IET International Conference on Power Electronics, Machines and Drives (PEMD 2016)*, Glasgow, 2016.

[61] R. Vaid, P. Agnihotri, A. M. Gole, A. M. Kulkarni and X. Chen, "Wide-area control of multi-infeed HVDC links for targeted swing mode damping using special feedback signals," in *Proceedings of the 13th IET International Conference on AC and DC Power Transmission (ACDC 2017)*, Manchester, 2017.

[62] R. Shah, R. Preece and M. Barnes, "Role of multi-infeed VSC-HVDC on dynamic behavior of future North Scotland transmission system," in *Proceedings of the 13th IET International Conference on AC and DC Power Transmission (ACDC 2017)*, Manchester, 2017.

[63] R. Shah, R. Preece and M. Barnes, "The Impact of Voltage Regulation of Multiinfeed VSC-HVDC on Power System Stability," *IEEE Transactions on Energy Conversion,* vol. 33, no. 4, pp. 1614-1627, 2018.

[64] W. Du, Q. Fu, X. Wang and H. F. Wang, "Small-signal stability analysis of integrated VSC-based DC/AC power systems – a review," *International Journal of Electrical Power & Energy Systems,* vol. 103, pp. 545-552, 2018.

[65] A. Bayo-Salas, J. Beerten, J. Rimez and D. Van Hertem, "Analysis of control interactions in multi-infeed VSC HVDC connections," *IET Generation, Transmission & Distribution,* vol. 10, no. 6, pp. 1336-1344, 2016.

[66] H. Saad, Y. Fillion, S. Deschanvres, Y. Vernay and S. Dennetiere, "On resonances and harmonics in HVDC-MMC station connected to AC grid," *IEEE Transactions on Power Delivery,* vol. 32, no. 3, pp. 1565-1573, 2017.

[67] L. Xu and L. Fan, "Impedance-based resonance analysis in a VSC-HVDC system," *IEEE Transactions on Power Delivery,* vol. 28, no. 4, pp. 2209-2216, 2013.

[68] Y. Shao and T. Yong, "Voltage stability analysis of multi-infeed HVDC systems using small-signal stability assessment," in *IEEE PES T&D*, New Orleans, 2010.

[69] G. Stagg and A. H. El-Abiad, Computer methods in power system analysis, McGraw-Hill, Inc., 1968.

[70] H. Ali and D. Dasgupta, "Effects on time delays in the electric power grid," in *6th International Conference on Critical Infrastructure Protection (ICCIP)*, Washington, DC, 2012.

[71] C. Karawita and U. D. Annakkage, "Multi-Infeed HVDC Interaction Studies Using Small-Signal Stability Assessment," *IEEE Transactions on Power Delivery,* vol. 24, no. 2, pp. 910-918, 2009.

[72] M. Amin, J. A. Suul, S. D'Arco, E. Tedeschi and M. Molinas, "Impact of state-space modelling fidelity on the small-signal dynamics of VSC-HVDC systems," in *Proceedings of the 11th IET International Conference on AC and DC Power Transmission*, Birmingham, 2015.

[73] L. Zhang, L. Harnefors and H.-P. Nee, "Modeling and Control of VSC-HVDC Links Connected to Island Systems," *IEEE Transactions on Power Systems,* vol. 26, no. 2, pp. 783-793, 2011.

[74] G. Chunyi, L. Wei, Z. Chengyong and N. Xiaojun, "Small-signal dynamics and control parameters optimization of hybrid multiinfeed HVDC system," *International Journal of Electrical Power & Energy Systems,* vol. 98, pp. 409-418, 2018..

[75] W. Ye, Z. Chengyong and G. Chunyi, "Comparison study of small-signal stability of MMC-HVDC system in different control modes," *International Journal of Electrical Power & Energy Systems,* vol. 111, pp. 425-435, 2019..

[76] D. H. R. Suriyaarachchi, U. D. Annakkage, C. Karawita and D. A. Jacobson, "A Procedure to Study Sub-Synchronous Interactions in Wind Integrated Power Systems," *IEEE Transactions on Power Systems,* vol. 28, no. 1, pp. 377-384, 2013.

[77] D. H. R. Suriyaarachchi, U. D. Annakkage, C. Karawita, D. Kell, R. Mendis and R. Chopra, "Application of an SVC to damp sub-synchronous interaction between wind farms and series compensated transmission lines," in *Proceedings of the 2012 IEEE Power and Energy Society General Meeting*, San Diego, 2012.

[78] P. Hasanpor Divshali, S. H. Hosseinian and M. Abedi, "Enhancing Small Signal Stability and Reactive Power-sharing Accuracy in Autonomous Microgrids by a New Decentralized Reactive Power Controller," *Electric Power Components and Systems,* vol. 40, no. 16, pp. 1820-1841, 2012.

[79] Y. Saad, Numerical methods for large eigenvalue problems, Society for Industrial and Applied Mathematics, 2011.

[80] A. Bidadfar, H.-P. Nee, L. Zhang, L. Harnefors, S. Namayantavana, M. Abedi, M. Karrari and G. B. Gharehpetian, "Power System Stability Analysis Using Feedback Control System Modeling Including HVDC Transmission Links," *IEEE Transactions on Power Systems,* vol. 31, no. 1, pp. 116-124, 2016.

[81] P. W. Sauer and M. A. Pai, Power System Dynamics and Stability, Prentice Hall, 1998.

[82] IEEE, "IEEE Recommended Practice for Excitation System Models for Power System Stability Studies," 1992. [Online]. Available: https://ieeexplore.ieee.org/document/182869. [Accessed 6 May 2019].

[83] Illinois Center for a Smarter Electric Grid (ICSEG), "IEEE 39-Bus System," [Online]. Available: https://icseg.iti.illinois.edu/ieee-39-bus-system/. [Accessed 6 May 2019].

List of abbreviations

Abbreviation	Description
AC	Alternating Current
BJT	Bipolar Junction Transistor
CB	Circuit Breaker
CSC	Current Source Converter
DC	Direct Current
FACTS	Flexible AC Transmission Systems
FC	Flying Capacitor
FCS	Feedback Controlled System
GTO	Gate Turn-off Thyristor
HVDC	High-Voltage Direct-Current
ICC	Inner Current Control
IGBT	Insulated Gate Bipolar Transistor
IGCT	Integrated Gate Commutated Thyristor
LCC	Line-Commutated Converter
MCT	MOS-Controlled Thyristor
MI	Multi-Infeed
MI-HVDC	Multi-Infeed HVDC
MMC	Modular Multilevel Converter
MOSFET	Metal-Oxide-Semiconductor Field Effect Transistor
MTDC	Multi-Terminal HVDC
NPC	Neutral-Point Clamping
OPWM	Optimal Pulse Width Modulation
PCC	Point of Common Coupling
PI	Proportional-Integral
PLL	Phase-Locked Loop
PWM	Pulse Width Modulation

SC	Short-Circuit
SCC	Self-Commutated Converter
SCR	Short-Circuit Ratio
SRF	Synchronous Reference Frame
SSSA	Small-Signal Stability Analysis
VSC	Voltage Source Converter

List of symbols

Phasor or complex quantities of numerical variables are underlined. Roman type boldface denotes a matrix or a vector. RMS values of alternating quantities are written with upper case letters.

Symbol	Description
$\mathbf{A}$, $\mathbf{B}$, $\mathbf{C}$, $\mathbf{D}$	State-space representation matrices
C_{dc}	Converter DC side capacitance
C_{eq}	Equivalent per-arm capacitance of an MMC
C_f	AC side filter capacitance
C_{line}	AC line/cable capacitance
e	Converter voltage
f	Frequency
$\mathbf{f}$	Vector of the first order ordinary differential equations
$\mathbf{g}$	Vector of algebraic equations
i_A	Anode current (thyristor)
i_c	Circulating current (MMC converter)
i_C	Collector current (IGBT)
i_{cable}	Sum of DC side cable/line currents
i_{cv}	Converter AC side current
i_{dc}	Converter DC side current
i_G	Gate current (thyristor)
i_K	Cathode current (thyristor)
i_o	External grid current
$\mathbf{I}$	Identity matrix
k_{drp}	Droop coefficient

k_{ffv}	Binary feedforward constant of a PCC voltage
k_i	Integral coefficient of a PI regulator
k_p	Proportional coefficient of a PI regulator
L_a	MMC arm inductance
L_f	Converter inductance (phase reactor and transformer)
L_{line}	AC line/cable inductance
m	Number of transmission poles
p	Participation factor
p_{ac} , P_{ac}	Active power
$p_{\lim}$	Converter active power limit
q_{ac} , Q_{ac}	Reactive power
R_a	MMC arm resistance
R_f	Converter resistance (phase reactor and transformer)
R_{line}	AC line/cable resistance
$\mathbf{u}$	Input vector
v_{ac}	Converter AC side voltage (employed in outer control)
$v_{ac,rem}$	Remote bus AC voltage
v_{AK}	Voltage between the anode and the cathode (thyristor)
v_c	Circulating current driving voltage (MMC converter)
v_{CE}	Voltage between the collector and the emitter (IGBT)
v_{dc}	Converter DC side voltage
v_{GE}	Gate terminal voltage (IGBT)
v_{ICC}	Filtered PCC voltage employed in the ICC
$v_{\lim,l}$	Converter DC voltage lower limit

$v_{\lim,u}$	Converter DC voltage upper limit
V_{LL}	RMS line-to-line AC voltage
v_o	PCC AC grid voltage
v_{PLL}	Filtered PCC voltage employed in the PLL
v_R	Receiving-end voltage on a transmission line
v_S	Sending-end voltage on a transmission line
w_Σ	Aggregated zero-sequence energy sum (MMC converter)
$\mathbf{x}$	State-space vector
X	Reactance
$\mathbf{y}$	Output vector
α	Thyristor firing angle
γ	Integrator state of the ICC
δ	Phase angle between a converter and a grid voltage
$\Delta\varphi$	PLL phase tracking error
$\Delta\Theta_{PLL}$	Angle deviation estimated by the PLL
$\Delta\omega_{PLL}$	Frequency deviation estimated by the PLL
ε_{PLL}	Integrator state of the PLL
ζ	Damping ratio
ζ_z	Integrator state of the zero-sequence circulating current controller
Θ_{PLL}	Grid angle estimated by the PLL
κ_Σ	Integrator state of the aggregated zero-sequence energy sum controller
λ	Eigenvalue
ρ	Integrator state of an outer controller
σ	Real part of an eigenvalue
$\mathbf{\Phi}$	Right eigenvector

$\mathbf{\Psi}$	Left eigenvector
ω	Angular frequency
$\omega_{ac,f}$	Cut-off frequency of the AC voltage low-pass filter
ω_b	Base angular frequency
$\omega_{dc,f}$	Cut-off frequency of the DC voltage low-pass filter
ω_g	Per-unit grid angular frequency
$\omega_{ICC,f}$	Cut-off frequency of the PCC voltage low-pass filter employed in the ICC
$\omega_{p,ac}$	Cut-off frequency of the active power low-pass filter
ω_{PLL}	Per-unit grid frequency estimated by the PLL
$\omega_{PLL,f}$	Cut-off frequency of the PCC voltage low-pass filter employed in the PLL
$\omega_{q,ac}$	Cut-off frequency of the reactive power low-pass filter

Indices

a , b , c	Phase quantities
cz	Inner controller for the zero-sequence circulating current
d , q , z	d-, q- and zero-component
dyn	Dynamic network area
f	Low-pass filtered or measured values
gen	Generator
ICC	Inner controller for the converter AC currents
P	Outer controller for the active power or DC voltage
PLL	Phase locked loop
Q	Outer controller for the reactive power or AC voltage
vsc	Voltage source converter
$w\Sigma$	Outer controller for the aggregated zero-sequence energy sum

Superscripts

*	Reference value

Appendix A

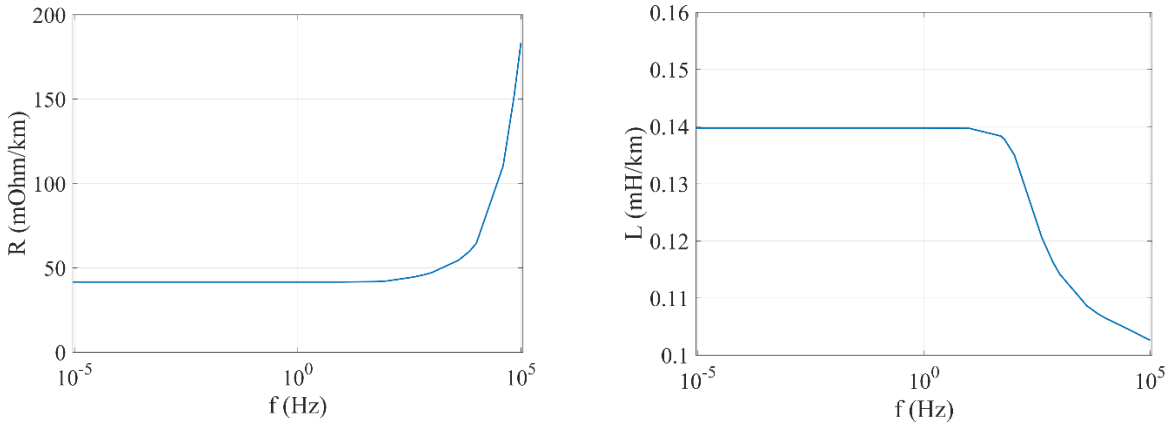

a) b)

Figure A.1: Frequency dependency: a) cable resistance; b) cable inductance

Table A.1: Electrical, control and base parameters of the test grid in Chapter 4

Parameters	Values
Phase reactor inductance	0.1656 pu
Phase reactor resistance	0.001 pu
Transfomer inductance	0.113 pu
Converter capacitance	0.004 pu
Cable resistance	$6.4938 \cdot 10^{-4}$ pu/km
Cable inductance	$2.1835 \cdot 10^{-6}$ pu/km
Cable capacitance	$9.7584 \cdot 10^{-6}$ pu/km
PLL proportional gain	10
PLL integral gain	250
Outer loop proportional gain	0
Outer loop integral gain	5
ICC proportional gain	0.371
ICC integral gain	79.8
Base power	100 MW
Base voltage	80 kV

Appendix B

Table B.1: Electrical parameters of the MI-HVDC system in Chapters 5 and 6

Parameters	Values
Nominal voltage	380 kV
Nominal power	1000 MVA
Line resistance	8.8 mΩ/km
Line inductance	0.67 mH/km
Line capacitance	17.3 nF/km
External grid resistance	0.0098 Ω
External grid inductance	0.0351 H

Table B.2: Electrical and control parameters of the MMCs in Chapters 5 and 6

Parameters	Values
Nominal voltage	313.5 kV
Nominal power	1000 MVA
Phase reactor inductance	0.0514 H
Phase reactor resistance	0.2802 Ω
Arm inductance	0.025 H
Arm resistance	0.4915 Ω
Converter capacitance	25.904 μF
DC cable capacitance	1.672 μF
AC filter capacitance	2.8721 μF
ICC proportional gain	2.6
ICC integral gain	21.4
Outer loop proportional gain	1
Outer loop integral gain	50
Circulating current prop. gain	0.1114
Circulating current int. gain	2.1875
Energy sum proportional gain	10
Energy sum integral gain	10
PLL 1 proportional gain	50
PLL 1 integral gain	833.3
PLL 2 proportional gain	10
PLL 2 integral gain	33.3

Appendix C

C.1. Synchronous generator model

$$T_{do}^{'}\frac{dE_q^{'}}{dt}=-E_q^{'}-(X_d-X_d^{'})\left[I_d-\frac{X_d^{'}-X_d^{''}}{(X_d^{'}-X_{ls})^2}(\psi_{1d}+(X_d^{'}-X_{ls})I_d-E_q^{'})\right]+E_{fd} \tag{8.1}$$

$$T_{do}^{''}\frac{d\psi_{1d}}{dt}=-\psi_{1d}+E_q^{'}-(X_d^{'}-X_{ls})I_d \tag{8.2}$$

$$T_{qo}^{'}\frac{dE_d^{'}}{dt}=-E_d^{'}-(X_q-X_q^{'})\left[I_q-\frac{X_q^{'}-X_q^{''}}{(X_q^{'}-X_{ls})^2}(\psi_{2q}+(X_q^{'}-X_{ls})I_q-E_d^{'})\right] \tag{8.3}$$

$$T_{qo}^{''}\frac{d\psi_{2q}}{dt}=-\psi_{2q}-E_d^{'}-(X_q^{'}-X_{ls})I_q \tag{8.4}$$

$$\frac{d\delta}{dt}=\omega-\omega_s \tag{8.5}$$

$$\frac{2H}{\omega_s}\frac{d\omega}{dt}=T_M-(\psi_d I_q-\psi_q I_d)-D(\omega-\omega_s) \tag{8.6}$$

$$\frac{1}{\omega_s}\frac{d\psi_d}{dt}=R_s I_d+\frac{\omega}{\omega_s}\psi_q+V_d \tag{8.7}$$

$$\frac{1}{\omega_s}\frac{d\psi_q}{dt}=R_s I_q-\frac{\omega}{\omega_s}\psi_d+V_q \tag{8.8}$$

$$\psi_d=-X_d^{''}I_d+\frac{(X_d^{''}-X_{ls})}{(X_d^{'}-X_{ls})}E_q^{'}+\frac{(X_d^{'}-X_d^{''})}{(X_d^{'}-X_{ls})}\psi_{1d} \tag{8.9}$$

$$\psi_q=-X_q^{''}I_q+\frac{(X_q^{''}-X_{ls})}{(X_q^{'}-X_{ls})}E_d^{'}+\frac{(X_q^{'}-X_q^{''})}{(X_q^{'}-X_{ls})}\psi_{2q} \tag{8.10}$$

Equations (8.7) – (8.8) represent stator winding dynamics.

Variables and parameters	Description
V_d, V_q	d- and q-axis of the generator terminal voltage
I_d, I_q	d- and q-axis of the stator current
$E_d^{'}, E_q^{'}$	d- and q-axis of the transient internal emf
E_{fd}	field voltage

ψ_{1d}, ψ_{2q}	d- and q-axis of the damper winding flux linkages
δ	rotor angle with respect to a synchronous reference frame
ω	rotor angular frequency
ψ_d, ψ_q	d- and q-axis of the stator winding flux linkages
ω_s	synchronous angular frequency
R_s, X_{ls}	stator resistance and reactance
X_d, X_q	d- and q-axis synchronous reactances
$X_d^{'}, X_q^{'}$	d- and q-axis transient reactances
$X_d^{''}, X_q^{''}$	d- and q-axis subtransient reactances
$T_{do}^{'}, T_{qo}^{'}$	d- and q-axis transient open loop time constants
$T_{do}^{''}, T_{qo}^{''}$	d- and q-axis subtransient open loop time constants
H	machine inertia constant
D	damping constant
T_M	mechanical torque

C.2. Excitation system model (type AC4A)

$$T_A \frac{dE_{fd}}{dt} = K\left(1 - \frac{T_C}{T_B}\right)x_{avr} + K\frac{T_C}{T_B}(V_{ref} - V_t) - E_{fd} \tag{8.11}$$

$$T_B \frac{dx_{avr}}{dt} = V_{ref} - V_t - x_{avr} \tag{8.12}$$

$$V_t = \sqrt{V_d^2 + V_q^2} \tag{8.13}$$

Variables and parameters	Description
x_{avr}	exciter state variable
V_{ref}, V_t	reference and generator terminal voltage
T_B, T_C	time constants of lag-lead compensator
K, T_A	voltage regulator gain and time constant

An effect of the terminal voltage transducer is neglected.

C.3. IEEE 39 bus test system

C.3.1. Line data

From bus	To bus	*R*	*X*	*B*
1	2	0.0035	0.0411	0.6987
1	39	0.0010	0.0250	0.7500
2	3	0.0013	0.0151	0.2572
2	25	0.0070	0.0086	0.1460
3	4	0.0013	0.0213	0.2214
3	18	0.0011	0.0133	0.2138
4	5	0.0008	0.0128	0.1342
4	14	0.0008	0.0129	0.1382
5	6	0.0002	0.0026	0.0434
5	8	0.0008	0.0112	0.1476
6	7	0.0006	0.0092	0.1130
6	11	0.0007	0.0082	0.1389
7	8	0.0004	0.0046	0.0780
8	9	0.0023	0.0363	0.3804
9	39	0.0010	0.0250	1.2000
10	11	0.0004	0.0043	0.0729
10	13	0.0004	0.0043	0.0729
13	14	0.0009	0.0101	0.1723
14	15	0.0018	0.0217	0.3660
15	16	0.0009	0.0094	0.1710
16	17	0.0007	0.0089	0.1342
16	19	0.0016	0.0195	0.3040
16	21	0.0008	0.0135	0.2548
16	24	0.0003	0.0059	0.0680
17	18	0.0007	0.0082	0.1319
17	27	0.0013	0.0173	0.3216
21	22	0.0008	0.0140	0.2565
22	23	0.0006	0.0096	0.1846
23	24	0.0022	0.0350	0.3610
25	26	0.0032	0.0323	0.5130
26	27	0.0014	0.0147	0.2396
26	28	0.0043	0.0474	0.7802
26	29	0.0057	0.0625	1.0290
28	29	0.0014	0.0151	0.2490

C.3.2. Transformer data

From bus	To bus	R	X	Ratio
12	11	0.0016	0.0435	1.006
12	13	0.0016	0.0435	1.006
6	31	0	0.0250	1.070
10	32	0	0.0200	1.070
19	33	0.0007	0.0142	1.070
20	34	0.0009	0.0180	1.009
22	35	0	0.0143	1.025
23	36	0.0005	0.0272	1.000
25	37	0.0006	0.0232	1.025
2	30	0	0.0181	1.025
29	38	0.0008	0.0156	1.025
19	20	0.0007	0.0138	1.060

C.3.3. Power flow – load data

Bus	$P[\text{MW}]$	$Q[\text{MVAr}]$
3	322.0	2.4
4	500.0	184.0
7	233.8	84.0
8	522.0	176.0
12	7.5	88.0
15	320.0	153.0
16	329.0	32.3
18	158.0	30.0
20	628.0	103.0
21	274.0	115.0
23	247.5	84.6
24	308.6	-92.2
25	224.0	47.2
26	139.0	17.0
27	281.0	75.5
28	206.0	27.6
29	283.5	26.9
31	9.2	4.6
39	1104.0	250.0

C.3.4. Power flow – generator data

Bus	Type	$v\,[\text{pu}]$	$P\,[\text{MW}]$
30	PV	1.0475	250.0
31	PV	0.9820	520.3
32	PV	0.9831	650.0
33	PV	0.9972	632.0
34	PV	1.0123	508.0
35	PV	1.0493	650.0
36	PV	1.0635	560.0
37	PV	1.0278	540.0
38	PV	1.0265	830.0
39	SQ	1.0300	-

C.3.5. Dynamic data – generators

Bus	R_s	X_{ls}	X_d	X_q	$X_d^{'}$	$X_q^{'}$	$X_d^{''} = X_q^{''}$	$T_{do}^{'}$	$T_{qo}^{'}$	$T_{do}^{''}$	$T_{qo}^{''}$	H	D
30	0	0.013	0.1	0.069	0.031	0.03	0.02	10.2	1.5	0.02	0.02	42	0
31	0	0.035	0.295	0.282	0.07	0.167	0.053	6.56	1.5	0.02	0.02	30.3	0
32	0	0.03	0.25	0.237	0.053	0.088	0.04	5.7	1.5	0.02	0.02	35.8	0
33	0	0.03	0.262	0.258	0.08	0.143	0.06	5.69	1.5	0.02	0.02	28.6	0
34	0	0.054	0.67	0.62	0.132	0.166	0.099	5.4	0.44	0.02	0.02	26	0
35	0	0.022	0.254	0.241	0.05	0.081	0.038	7.3	0.4	0.02	0.02	34.8	0
36	0	0.032	0.295	0.292	0.09	0.167	0.068	5.66	1.5	0.02	0.02	26.4	0
37	0	0.028	0.29	0.28	0.057	0.091	0.043	6.7	0.41	0.02	0.02	24.3	0
38	0	0.03	0.211	0.205	0.057	0.07	0.043	4.79	1.96	0.02	0.02	34.5	0

C.3.6. Dynamic data – exciters

Bus	K	T_A	T_B	T_C
30	6.2	0.05	10	1
31	5	0.06	10	1
32	5	0.06	10	1
33	40	0.02	10	1
34	5	0.02	10	1
35	40	0.02	10	1
36	5	0.02	10	1
37	40	0.02	10	1
38	5	0.02	10	1

Biography

Goran Grdenić was born in 1990 in Zagreb. He received his B. Sc. and M. Sc. degrees in electrical engineering and information technology at the University of Zagreb, Faculty of Electrical Engineering and Computing (FER) in 2012, and 2014, respectively. He defended his doctoral dissertation in 2019 at the same faculty. From 2015 he has been working as a teaching and research assistant with the Department of Energy and Power Systems at FER. In the academic year 2017/2018, he spent four months as a visiting researcher at the KU Leuven, Belgium. In 2014 he received the award “Hrvoje Požar” for the best students in energy-related studies.

List of publications

Journals

1. G. Grdenić, M. Delimar and J. Beerten, "Comparative Analysis on Small-Signal Stability of Multi-Infeed VSC HVDC System with Different Reactive Power Control Strategies," *IEEE Access*, vol. 7, pp. 151724-151732, 2019.

2. G. Grdenić and M. Delimar, "Small-Signal Stability Analysis of Interaction Modes in VSC MTDC Systems with Voltage Margin Control," *Energies*, vol. 10, no. 873, 2017.

3. M. Pikutić, G. Grdenić and M. Delimar, "Comparison of results and calculation speeds of various power system power flow methods," *Journal of Energy*, vol. 66, pp. 117-127, 2017.

4. G. Grdenić and Ž. Tomšić, "Renewable energy sources and other energy technologies as a measure for mitigating the impact of urban heat islands," *Journal of Energy*, vol. 66, pp. 184-194, 2017.

Conferences

1. G. Grdenić and M. Delimar, "Energetska elektronika u visokonaponskom istosmjernom prijenosu električne energije," in *The 14th HRO CIGRÉ Session*, Šibenik, 2019.

2. G. Grdenić, M. Delimar and J. Beerten, "Small-Signal Stability Analysis of Multi-Infeed VSC HVDC System Under Different Reactive Power Control Strategies," in *The 11th Mediterranean Conference on Power Generation, Transmission, Distribution and Energy Conversion*, Cavtat, 2018.

3. G. Grdenić and Ž. Tomšić, "Obnovljivi izvori energije i ostale energetske tehnologije kao mjera za smanjivanje utjecaja gradskih toplinskih otoka," in *The 12th HRO CIGRÉ Session*, Šibenik, 2015.

Životopis

Goran Grdenić rođen je 1990. u Zagrebu. Preddiplomski i diplomski studij elektrotehnike i informacijske tehnologije završio je 2012., odnosno 2014. godine na Fakultetu elektrotehnike i računarstva (FER) Sveučilišta u Zagrebu. Doktorski rad obranio je 2019. godine na istome fakultetu. Od 2015. godine radi na Zavodu za visoki napon i energetiku FER-a kao asistent. Akademske godine 2017./2018. proveo je četiri mjeseca na znanstvenom i stručnom usavršavanju na Katoličkom sveučilištu u Leuvenu, Belgija. Nagrađen je nagradom „Hrvoje Požar“ 2014. godine za najbolje studente u području energetike.